# In-Situ Monitoring of Groundwater Radionuclides with Emphasis on Tritium Detection

Tilly Lucy Alton, MSci Physics


Submitted for the degree of Doctor of Philosophy at Lancaster University.

January 2019

# Abstract

This thesis is concerned with the detection of low energy beta emitting radioisotopes from a source of groundwater, with particular emphasis on tritium ($^3$H). This is investigated firstly through an understanding of the challenges of detecting tritiated water, which involves the use of Monte Carlo simulations, numerical analysis and the development of simple scintillator-based detector system. Secondly, by a novel exploration of heterogeneous scintillators, utilising scintillator fabrication, Geant4 simulations and a refined detector prototype. And finally, by the design and testing of a flow cell detector based on the novel heterogeneous scintillator, including the detection of transient tritium concentration levels. The results have demonstrated that the beta particle in the tritiated water undergoes attenuation which causes a shift in the detected energy spectrum, which is particularly relevant for single crystal scintillator detectors used to discriminate radioisotopes by comparing beta spectra. The heterogeneous scintillator used was fabricated through a granulation method, before being used to validate simulations resulting in a novel heterogeneous scintillator configuration. The results of the flow cell and associated detection showed tentative validation of the theory, showing how a short detection time would impact on detector performance.

# Acknowledgements

I would like to acknowledge and thank my two supervisors Dr David Cheneler and Dr Stephen Monk for their help and guidance over the last few years, without it this would likely have not been possible. For providing the flow cell in Chapter 7 and scintillators in Appendix A.6, thank you Neil Maddison, and thank you to Dr Cheneler for providing the work in the Appendix A.3 & A.7. I also need to thank my family for all their support and kindness, over these last few interesting years. For helping me in many many ways during my time at Lancaster I would like to thank Dr. Ioannis Tsitsimpelis, Dr. Ioannis Tzagkaroulakis, Dimitrios Afouxenidis, Man-Li Huang, Mauro Licata, Miriam Ferrer Huerta, Dr. Sam O'Sullivan, Dr. Jackie Pates, Andy Verden, Dr. James Dickinson & Avril Collett. And a big thank you to Yue Tan for her overwhelming support, especially when it was so crucially needed.

I would also like to acknowledge and thank the Lancaster University Engineering Department for funding this research.

# Declaration

I declare that the work in this thesis has been done by myself and has not been submitted elsewhere for the award of any other degree.

Tilly Lucy Alton

# Contents

# List of Figures

# List of Tables

# Chapter 1

# Introduction

The focus of this thesis is the design and testing of a detection system for low-energy beta particle emitting radionuclides with particular emphasis on waterborne tritium. Tritium, a radioactive isotope of hydrogen, is produced naturally by the interaction of cosmic rays with upper atmospheric nitrogen; more importantly, it is also produced through atomic weapons testing, and industrial processes [1, 2]. Tritium enters the environment through a number of pathways, such as the atmospheric circulation of naturally produced tritium, weapons testing, industrial processes or accidents. Once in the environment it behaves in a similar way as the more common hydrogen isotope, i.e. protium. Although tritium has a relatively short half-life of 12.3 years and emits a beta particle with a low energy ($<$18.6 keV), it can lead to localised damage to the body's cells. Currently it is deemed to have a low biological effectiveness, but there have been recommendations to increase its biological effectiveness value [3]. At present, the most accurate methods of detecting waterborne tritium are laboratory-based liquid scintillation [4, 5]. This makes in-situ and near real-time detection diffi-

cult. A near real-time, in the field detection system that detects waterborne tritium in-situ will allow easier detection in a range of environmental applications and as a direct consequence will allow for quicker and easier monitoring reducing any related biological risk.

The motivation behind this research is to firstly gain a better understanding of the challenge of waterborne tritium detection, and secondly to design and test an experimental detector demonstrating performance improvements. The overall aim of this thesis is the development of a prototype of a heterogeneous scintillator for waterborne tritium detection.

## 1.1 Research Objectives & Aims

- An initial aim of the work is to investigate and understand through simulations the inherent difficulties of waterborne tritium detection with a scintillator.
- Design and fabrication of the data collection and processing system for the radiation detection sensor.
- Development of a heterogeneous scintillator using simulated and experimental data. This heterogeneous scintillator has to demonstrate improved performance in a continous flow-cell scenario when comparing with pre-existing detectors.
- Proof of concept for the use of a heterogeneous flow-cell for detecting tritium in solution. This includes a source with differing flow rates and concentrations

that are both constant and transient.

## 1.2 Publications

1. T. Alton, S. Monk, D. Cheneler. Beta Particle Energy Spectra Shift due to Self-attenuating Effects in Environmental Sources, Nuclear Engineering and Technology, vol 49, issue 7, pp. 1483-1488, 2017. (See Chapter 4).

2. T. Alton, S. Monk, D. Cheneler. Corrigendum to "Beta particle energy spectra shift due to self-attenuation effects in environmental sources", Nuclear Engineering and Technology, vol 50, issue 6, pp. 996, 2018.

3. S.D Monk, B.A. Shippen, B.R Colling, D. Cheneler, H. Al Hamrashdi, T. Alton. A comparison of MCNP6-1.0 and GEANT 4-10.1 when evaluating the neutron output of a complex real world nuclear environment: the thermal neutron facility at the Tri Universities Meson facility, Nuclear Instruments and Methods Research Section B, vol 399, pp. 48-61, 2017. This article assisted with learning the Geant4 code which forms a vital part of the thesis.

4. T. Alton, S. Monk, D. Cheneler. Heterogeneous Scintillator Geometries for Waterborne Beta Particle Detection, Radiation Measurements, 111, 6-12, 2018. (See Chapters 5 & 6).

## 1.3 Conference Presentations

- In Situ Monitoring of Radionuclides in Water, With Emphasis on Tritium Detection, Universities Nuclear Technology Forum (UNTF), Open University, 2015.
- In Situ Groundwater Radionuclide Detector with Geant4 Simulation Data, Lancaster University Engineering Postgraduate Review Conference, Lancaster University, 2015.
- In Situ Monitoring of Radionuclides in Water, With Emphasis on Tritium Detection, Universities Nuclear Technology Forum (UNTF), Sheffield University, 2016.
- In Situ Monitoring of Radionuclides in Water, With Emphasis on Tritium Detection, Lancaster University Engineering Postgraduate Review Conference, Lancaster University, 2016.
- In Situ Monitoring of Radionuclides in Water, With Emphasis on Tritium Detection, Lancaster University Engineering Postgraduate Review Conference, Lancaster University, 2017.

## 1.4 Thesis Organisation

The thesis is organised into eight chapters and an appendix.

This first Chapter is an introduction detailing the organisation of the thesis, the second chapter is a comprehensive view of the literature of the subjects of this thesis,

solid scintillators, heterogeneous scintillators and flow-cell detectors. A short description of radiation transport detailing the passage of beta particles in matter, comprises Chapter 3, which also includes a short investigation of the range of tritium beta particles. The fourth chapter describes the single crystal detector and design, including the modelling, electronics used, results, discussion and conclusion. Chapter 5 covers the process of producing the particulate scintillators, covering both chemical and mechanical approaches. Chapters 6 and 7 cover the heterogeneous scintillator and the flow cell heterogeneous scintillator respectively, detailing both simulation and experimental setup, the results, discussion and conclusion. Chapter 8 comprises of the conclusions to this thesis. The Appendix contains supplimentary information.

# Chapter 2

# Tritium Behaviour & Detection

This chapter covers the current literature and understanding of detecting beta particles and particularly tritium (T). Whilst the research area has been broken down into various sections there is particular emphasis on scintillation crystals and flow cell detection as these are key areas.

## 2.1 Tritium

Hydrogen has three common isotopes [6, 7], Protium ($^{1}_{1}$H), Deuterium ($^{2}_{1}$H) and Tritium ($^{3}_{1}$H), with the respective natural abundances being 99.9885%, 0.0115% & $1 \times 10^{-9}$% [8, 9]. The structure of these isoptopes is such that all three have a proton in the nucleus and an orbiting electron. The difference between the isotopes is the addition of neutrons, one for deuterium and two for tritium. Whilst tritium was initially discovered in 1934 [10], it wasn't until 1939 that it was isolated and identified

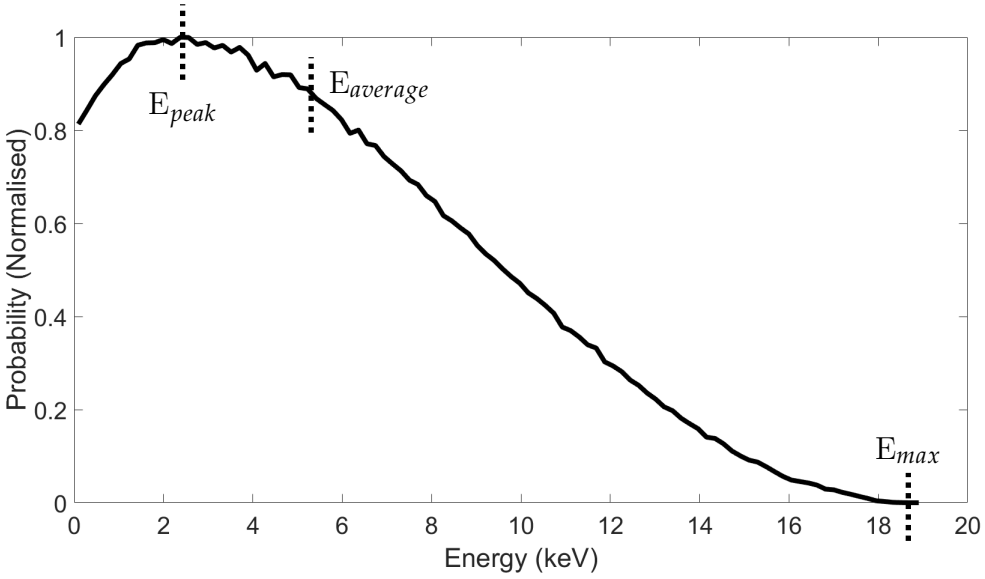


Figure 2.1.1: Tritium beta particle energy spectrum [17].

as radioactive [11, 12, 13, 14]. Aside from the different atomic masses they all behave the same chemically. Tritium is unstable and decays with a Super Allowed [15] decay and with a half-life of 12.3 years. One of the neutrons in the tritium nucleus decays and releases both a beta particle (an electron) and an electron anti-neutrino [16], producing a daughter helium atom, ${}^{3}_{2}\mathrm{He}$, see Eq. (2.1.1). This results in a beta particle being emitted with a spectrum of possible kinetic energies, the maximum of which is 18.6 keV with an average of 5.7 keV [15], see Fig. 2.1.1.

$$ {}^{3}_{1}H \rightarrow {}^{3}_{2}He + e^{-} + \bar{\nu}_{e} \tag{2.1.1} $$

Natural tritium production in the upper atmosphere is mainly by neutron capture of $^{14}\mathrm{N}$, followed by decay into $^{12}\mathrm{C}$ & $^{3}\mathrm{H}$, $^{14}\mathrm{N}(\mathrm{n},{}^{3}_{1}\mathrm{H})^{12}\mathrm{C}$ [18, 19]. More importantly, tritium is introduced into the environment by the nuclear industry with, routine dis-

charges, such as from CANDU reactors [20], atmospheric discharges [21] and pipeline discharges [2]. Tritium is also produced by nuclear fuel reprocessing sites, for example, in a pressure water reactor the boron in boric acid will undergo neutron absorption. The subsequent decay will create a tritium atom, which will be separated when the fuel is reprocessed [22, 23]. Tritium is also released during atomic weapons testing [1] and accidents, such as Fukushima [24] and Chernobyl [25, 26]. As tritium's chemical behaviour is identical to that of hydrogen, it may be found in many hydrogen containing compounds. The majority of tritium produced in the atmosphere oxidises to tritiated water (HTO) [4], or to tritiated hydrogen (HT) [4]. Other physiochemical atmospheric forms do exist, such as tritiated methane ($CH_3T$) and tritiated ethanol ($C_2H_5T$) [27]. Tritium is also found in the bioshphere with organically bound tritium (OBT). Within the hydrosphere, the majority is in the form of HTO [28].

### 2.1.1 Environmental Concentrations

In designing a detector for in-situ use, it is necessary to benchmark against real world concentrations and legal limits. There are various legal limits in place for environmental tritium levels and a selection is shown in Table 2.1.1.

Table 2.1.1: Tritium limits for drinking water for a number of countries, the World Health Organisation and the European Union [29].

| Country/Organisation | Tritium limit ($\mathrm{Bq\,mL^{-1}}$) |
|---|---|
| Australia | 76.103 |
| Finland | 30 |
| WHO | 10 |
| Switzerland | 10 |
| Russia | 7.7 |
| Canada (Ontario) | 7 |
| United States | 0.74 |
| European Union | 0.1 |

It should be noted that the European Union, Australian and Canadian limits are a guideline. However some states such as France and Germany apply the European Limit as a legal limit, some provinces in Canada apply their recommended limit ($7\,\mathrm{Bq\,mL^{-1}}$) as a legal standard [29], such as Ontario.

Tritium levels in the Irish Sea have been examined [30] and the conclusion was that the normalised activity concentration had a mean of $6.9 \pm 0.4\,\mathrm{Bq\,mL^{-1}}$. Using the published discharge data from 2013 [31] the total discharges from pipeline and sewer were 1400 TBq and 6.6 GBq respectively. Using the stated mean above the concentrations from the pipeline and sewer are then $9.66\,\mathrm{mBq\,mL^{-1}}$ and $41\,\mathrm{nBq\,mL^{-1}}$. The

waters around various French nuclear sites [32] were found to have minimum and maximum concentrations of 5 and 70 $\mathrm{mBq\,mL^{-1}}$ respectively. The Western Shore of the Black Sea was sampled [33] and the collected data found a minimum and maximum of 0.03 and 0.4 $\mathrm{mBq\,mL^{-1}}$. The Gulf of Finland [34] had several locations analysed with the results showing a minimum and maximum concentration of 0.6 $\mathrm{mBq\,mL^{-1}}$ and 5.76 $\mathrm{mBq\,mL^{-1}}$.

The above information, particularly the WHO and EU drinking water limits, can be utilised to provide benchmarks for the performance of a developed detector.

### 2.1.2 Health Effects of Tritium

Once tritium has entered the environment there are a number of pathways into the body such as tritiated water and organically bound tritium (OBT). The main pathway into the body is through ingestion of tritiated water (HTO) [28], however this has a short biological half-life of 10 days [35]. OBT has a much longer biological half-life ($\sim$100 days) [35] and accounts for the majority of the tritium content in tissue for animals and humans [36, 37]. The different physiochemical forms of tritium also extends to the dose coefficients for adults, namely $4 \times 10^{-11}\,\mathrm{Sv\,Bq^{-1}}$ and $9 \times 10^{-11}\,\mathrm{Sv\,Bq^{-1}}$ for HTO & OBT respectively [38]. The Relative Biological Effectiveness (RBE) is a weighting factor given to ionising radiation to highlight the different effects it has on the body at the same energy. Tritium's penetration length in water is comparable to the average size of a cell in the body, i.e. 10-20 µm, this along with its behaviour in the body leads to localised doses, such as the breast and colon [39]. The International

Commission on Radiological Protection (ICRP) considers a weighting factor of 1 for beta particles relative to gamma rays, however the UK Health Protection Agency [3] and the US Oak Ridge National Laboratory [40] recommend and conclude stating that for tritium the value should be 2. This increase is due to the behavior of the tritium beta particles and the associated biological effectiveness. Once in the body the effects of tritium are consistent with other ionising radiations [41, 42] in being able to induce stochastic (probability is a function of dose [43]) and deterministic (severity is a function of dose [43]) effects, although the data that currently exists is for lab animals (mice & rats), no epidemiological data shows stochastic effects on humans [41].

## 2.2 Tritium Detection

There are a number of detection systems that have been used for detecting tritiated water. The most common method is a Liquid Scintillation Counter (LSC) employing a liquid scintillator. Here the radioisotope is typically placed into a glass vial (approximately 20 mL) with a scintillation cocktail, this cocktail contains a solvent, scintillator and surfactant [44]. Inside the vial the energy from the decaying radioisotope is transferred to the scintillator through the solvent [44], the generated scintillation photons are then counted within the LSC using a technology such as a PhotoMultiplier Tube (PMT). There are two drawbacks applicable here, firstly that it is challenging to implement in-situ and secondly, is that the waste material is often

harmful to the environment [45]. This method is widely adopted as it has a high counting efficiency for tritium, for example Ultima Gold has 56% counting efficiency for tritium [44].

Direct detection using a mercuric iodide ($HgI_2$) semiconductor has been demonstrated [46]. This device was custom fabricated using a wafer of $HgI_2$, electrodes of an acrylic graphite composition and palladium wires, see Fig. 2.2.1. The results showed a promising 25% efficiency however the surface is hygroscopic, meaning water absorbing [47], which leads to material degradation. A deadlayer of 0.2 µm thick on the surface was concluded by the authors [46], with this the predicted life expectancy of the device is poor (50% for one month). Adding an additional layer to protect the $HgI_2$ from the water would increase the predicted life expectancy (75% for two years) but would cause further attenuation, which is already significant (0.5 keV losses).

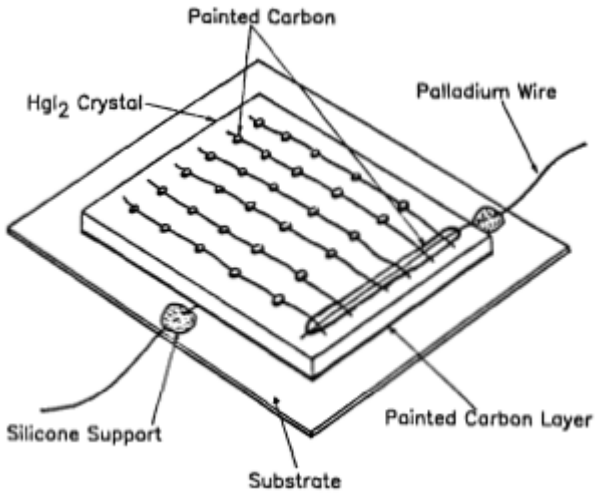


Figure 2.2.1: A diagram of the $HgI_2$ semiconductor used for direct detection of tritium [46].

Organic scintillators have been employed for tritium detection, two examples given here are BC-408 & BC-400 (BC referes to Bicron Corporation [48, 49]). The BC-408 detector [50, 51] was constructed as a flat disc of 29 mm diameter and 0.5 mm thick, with one surface in contact with the tritiated water. The container of tritium was lined with a reflective aluminium cup. The volume was $\sim$3 mL with concentration $\sim$3 GBq $L^{-1}$ and repeatedly counted for 10 min. The results showed a sensitivity of $1.39 \times 10^{-8}$ CPS/(Bq/L·$cm^2$), which is too low for the concentrations desired in this thesis, which are towards 10 Bq $mL^{-1}$ (Table 2.1.1). The scintillators BC-400 and europium doped calcium fluoride ($CaF_2$:Eu or $CaF_2$(Eu)) have been used to develop flow cell radiation detectors for waterborne tritium. One of the BC-400 designs [52] utilised a porous block made by dissolving the BC-400 in a mixture of ethyl-acetate and amyl-acetate, then stretching thin films of the solution.

They [52] determined a detection limit of 39 Bq $mL^{-1}$ with low count times of $<$5 min and a flow rate of 1 mL $min^{-1}$. A second design [53] used a channel in acrylic with a sheet of BC-400 above. The detection limit was found at a concentration of 346 Bq $mL^{-1}$ giving $\sim$0.6 CPS. However, it should be noted that both research groups [52, 53] experienced a contamination effect with BC-400. To counteract this the flow cell can be flushed with pure water to clean. Falter [52] determined that 30 min of flushing with distilled water was optimal, Uda [53] followed a similar principal in flushing with pure water.

It has been demonstrated that nanoporous palladium absorbs hydrogen, and therefore tritium [54, 55, 56]. This has formed the basis of a radiation detector where Pd

is adjacent to a scintillator, any tritium absorbed will then have a reduced possible path length to the scintillator. This design demonstrates a higher efficiency. However one major drawback is that the absorption will stop when the structure is full, when this happens it will need replacing, which is more of a difficulty in an in-situ situation.

$CaF_2$:Eu has been used for transuranics [57], high energy beta particles [58] and flow cells [59, 60, 61, 62], but also specifically for tritiated water detection [63, 64, 65, 66]. This tritium-specific design focused on a tube packed with purchased small particles of $CaF_2$:Eu, experimental results exploring how particle size affects the detected count rate can be seen in Fig. 2.2.2. The results show that the 50 µm particles achieve the highest count rate. Further experiments in shielding, using 900 kg of lead did not have a significant impact on the background count rate. The three articles demonstrated that concentrations of $10\,\mathrm{Bq\,mL^{-1}}$ can be detected with these purchased scintillator particles with a counting time of 600 s, albeit with a low flow rate ($1\,\mathrm{mL\,min^{-1}}$). The results into particle size did not reveal convergence, therefore further reduction could be beneficial. Further, the low flow rates are not suitable for in-situ detection of real-time sources, e.g. a transient concentration.

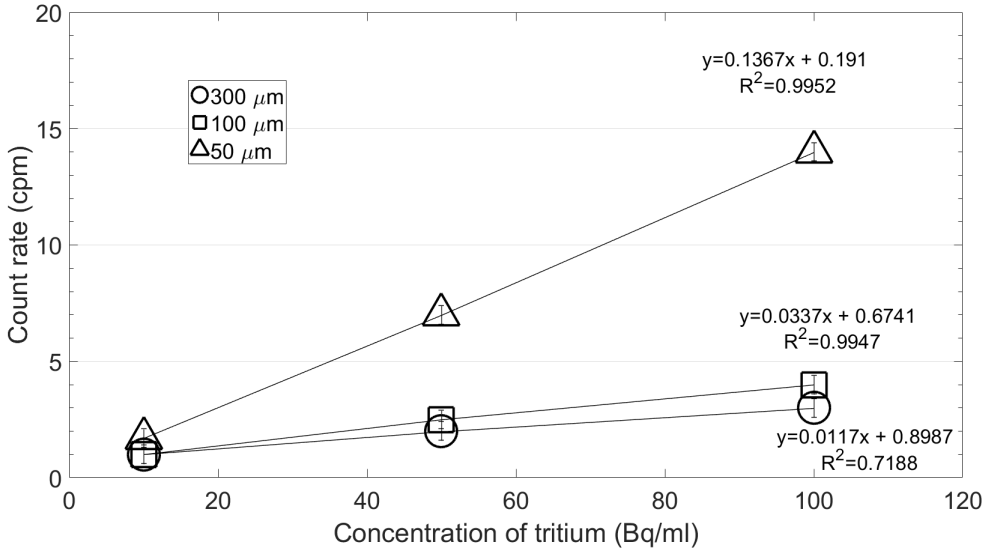


Figure 2.2.2: Graph of data investigating the impact of scintillator particle diameter on the count rate of waterborne tritium with a single flow cell, adapted from [64].

## 2.3 Scintillators

Scintillators have been used for detecting radiation for more than a century [67]. They can also be catagorised into organic, inorganic, and also hygroscopic & non-hygroscopic. Hygroscopic scintillators [68] are not suitable for exposure to water, and whilst it is possible to seal the material this would add an attenuating layer. Non-hygroscopic scintillators offer an alternative as they do not degrade with exposure to water, nor need a protective layer. The section on tritium (Chapter 2.1) highlighted the challenges of detection such as a low kinetic energy leading to a small penetration length ($<4\,\mu$m). Any additional layer in between the radioisotope and the scintillator will impact the device performance. As the radioisotope source will be in solution, tritiated water, then the ideal scintillator would be non-hygroscopic, and hygroscopic

ones can be ignored.

The previous section (Chapter 2.2) listed a number of scintillators, BC-400, BC-408 & $CaF_2$:Eu. However other non-hygroscopic scintillators do exist, which have been omitted for reasons such as low photon yield. This section covers the ideal scintillator choice, specifically the needs of such a scintillator are:

- Essential:
    1. Maximise scintillation photons created per unit energy of the incident beta particles.
    2. Non-hygroscopic, so detector performance is not compromised with prolonged exposure to the source.
- Desirable:
    1. Peak emission matching a photon detectors peak sensitivity to increase the detection efficiency of scintillation photons.
    2. Refractive index matching with photon detector will ensure ideal optical coupling and minimal photon losses.
    3. Linear light output with incident energy for ease of calibrating with incident energy.
    4. Minimal temperature dependency for better consistency across different operating environments.

Table 2.3.1 lists a selection of viable non-hygroscopic scintillators and their properties. The scintillators and accompanying references are, YSO:Ce [69], YAG:Ce [70],

YAP:Ce [71], CsI:Tl [72, 73], BC-400 [74] (also referred to as EJ-212 & NE102A [75]), BGO [76], $BaF_2$ [77], $CeF_3$ [78], $PbWO_4$ [79] and $CaF_2$:Eu [80, 81, 82, 83, 84].

The yttrium based scintillators listed are not suitable for this application because of their properties, such as low light yield and short decay time. There appears to be uncertainty in the literature about the hygroscopic nature of CsI:Tl, it is sometimes listed as non-hygroscopic and other times as partially hygroscopic [85, 72, 86]. Its high density and inconsistency in hygroscopic property make this scintillator not ideal.

The materials BGO, $BaF_2$, $CeF_3$ & $PbWO_4$ all have properties that are not optimal, such as too high refractive index or too low light yield. As was shown earlier, BC-400 has contamination issues, it has been shown to have little temperature dependency [87], and along with its properties stated in Table 2.3.1 make it ideal. $CaF_2$:Eu displays little temperature dependancy for its light yield [88] and high transmittance for optical photons [89] minimising absorption. It has a single emission peak for the scintillation photons [80].

Both BC-400 and $CaF_2$:Eu are amongst the better scintillators. BC-400 does however have a lower light yield than $CaF_2$:Eu ($10\,\text{photons}\,\text{keV}^{-1}$ compared with $\sim 30\,\text{photons}\,\text{keV}^{-1}$) and the noted contamination issue. The advantages of $CaF_2$:Eu are, non-hygroscopic, low density, emission peak at 425 nm (closely matches common photon detectors), refractive index of 1.44 (closely matching water and common photon detectors), reasonable brightness and minimal temperature dependency. $CaF_2$:Eu is the ideal scintillator for this tritium flow cell, with the only viable alternative BC-400.

Table 2.3.1: A review of the physical properties of a number of scintillators, YSO:Ce, YAG:Ce, YAP:Ce, CsI:Tl, BC-400, BGO, $BaF_2$, $CeF_3$, $PbWO_4$ and $CaF_2$:Eu. Scintillators with two decay times will be labelled as slow/fast.

| Properties of Inorganic Scintillators | | | | | | | | | | |
|---|---|---|---|---|---|---|---|---|---|---|
| | YSO:Ce | YAG:Ce | YAP:Ce | CsI:Tl | BC-400 | BGO | $BaF_2$ | $CeF_3$ | $PbWO_4$ | $CaF_2$:Eu |
| Wavelength of max emission (nm) | 420 | 370 | 370 | 550 | 423 | 480 | 310/220 | 340/300 | 440/530 | 435 |
| Index of refraction at max emission | 1.8 | 1.95 | 1.95 | 1.8 | 1.58 | 2.15 | 1.52 | 1.62 | 2.16 | 1.44 |
| Decay constant | 70 ns | 30 ns | 30 ns | 1 µs | 2.4 ns | 300 ns | 630/0.7 ns | 300/30 ns | 30/6 ns | 0.9 µs |
| Total light yield (Photons/keV) | 10 | 15 | 15 | 54 | 10 | 8-10 | 10-1.8 | 4.4 | 0.2 | 24-30 |
| Density ($g\,cm^{-3}$) | 4.5 | 5.3 | 5.3 | 4.51 | 1.023 | 7.13 | 4.88 | 6.16 | 8.28 | 3.179 |
| Hygroscopic | No | No | No | ? | No | No | No | No | No | No |
| Hardness (Mohs) | 5.6 | 8.5 | 8.5 | 2 | | 5 | 3 | ? | ? | 4 |
| Birks constant $g\,MeV^{-1}\,cm^{-2}$ | | | | | | | | | | $5.3x10^{-3}$ |

### 2.3.1 $CaF_2$:Eu Scintillation Process

$CaF_2$:Eu is a scintillating material and this section details its scintillation process when exposed to ionising radiation [90, 91, 92, 93]. When the ionising radiation enters the scintillator it will interact through a number of processes with the atomic nuclei, although it is more likely to be with the orbiting electrons. The result of this is the transfer of energy from the incident ionising radiation to the orbiting electrons, which creates electron-hole pairs in the scintillator (Fig 2.3.1). These electron-hole pairs migrate through the crystal to a location where they can recombine. There are a number of locations where the recombination occurs, such as a defect or doped element. Between the Valence Band & Conduction Band is a forbidden region, the europium is then used to add energy levels in the forbidden region. Recombinations at the europium dopant are radiative, meaning, the creation of visible photons.

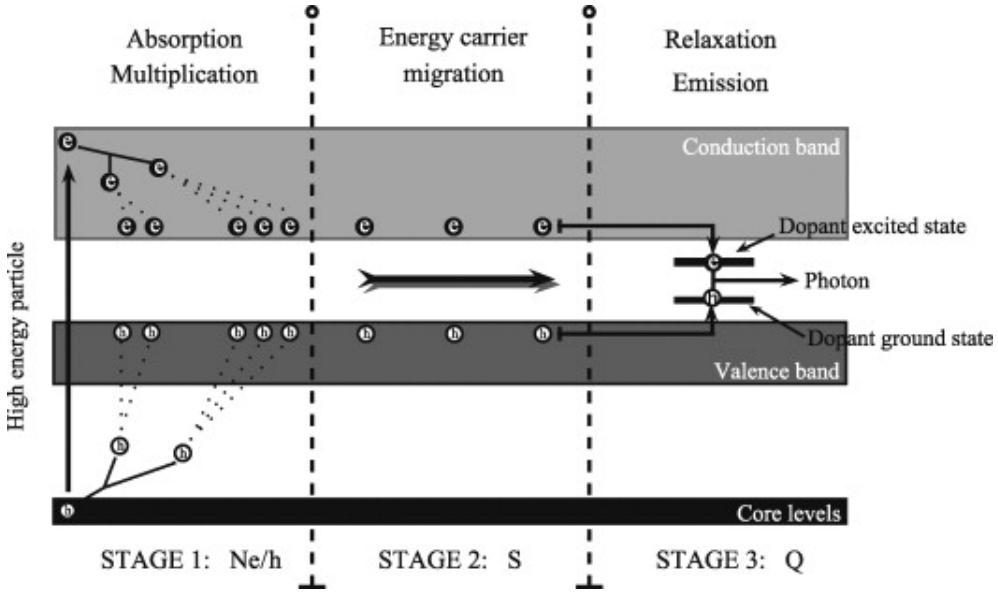


Figure 2.3.1: Diagram of the process of scintillation in $CaF_2$:Eu through the creation and recombination of electron-hole pairs [94].

### 2.3.2 Heterogeneous & Nanoparticle Scintillators

Unfortunately the nomenclature surrounding heterogeneous scintillators is a little unclear. There appears to be three terms in use to describe very similar and often overlapping structures of scintillators: heterogeneous [66], granulated [86, 95] & particulate [96, 97, 98, 99]. A fourth term, distributed [100], does exist but appears to have gained little traction. For the purpose of the rest of this thesis the term heterogeneous will be preferred as it is the most applicable as it usually refers to flow cell detectors.

A heterogeneous scintillator is a scintillator which is often made of a porous or dispersed structure [101], these are often in the form of tightly packed particles. The theory behind the effect of nanometer sized particle scintillators has been explored [102, 103] and demonstrates a number of advantages when compared with a single crystal of the same material; the luminescence of the nanoparticle scintillator increases as its radius decreases with some scintillators.

There is a reduction in the number of defects and therefore less non-radiative recombinations.

The reduction in size creates changes in the crystal structure such as, a broadening of the absorption & emission lines, an increase in the forbidden band and a change in the luminescence lifetime.

Many of the recombination centres are located on the surface, so application of a

coating can further increases the luminescence.

The radiative lifetime can be decreased by coating with a high refractive index material. Two practicalities have been noted, nanoparticle layers thicker than 0.5 mm become opaque and the size reduction leads to an increase in radiation hardness [103]. Experimental data validating validating various parts of the theory have been presented [102, 104], for example the prediction of an increase to luminescence and emission peak wavelength can be observed in Fig. 2.3.2. The data shows that the luminescence does increase, other predictions from the theory such as a shift in the peak emission wavelength are validated too.

A development of the nanoparticle and heterogeneous scintillator has been to apply a coating to the particles. This approach has a theoretical basis [102], with the explanation that recombinations on the surface are more likely to be non-radiative, therefore a surface coating will reduce the non-radiative recombinations. Experimental data for validation of this [105, 106] can be seen in Fig. 2.3.3. The results have demonstrated that for a few scintillators, including $CaF_2$:Eu it is possible to utilise a coating and core/shell structure for the particles to increase the luminescence.

The data has shown that the ideal scintillator would be $CaF_2$:Eu as its properties most meet the requirements, the alternative would be BC-400. The data and theory on heterogeneous & nanoparticle scintillators shows that it is an area that could provide a route for possible optimisation for tritium detection by increasing luminescence.

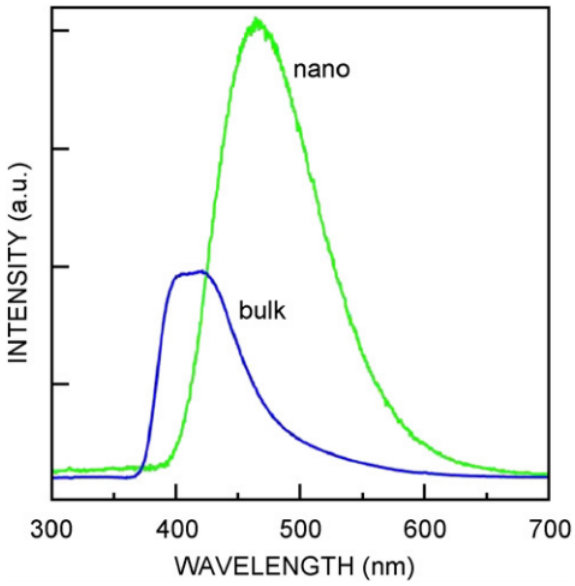


Figure 2.3.2: Experimental radioluminescence data using the scintillator YSO:Ce of both single crystal (Bulk) and nanoparticle setups. The light output is normalised by sample mass [104].

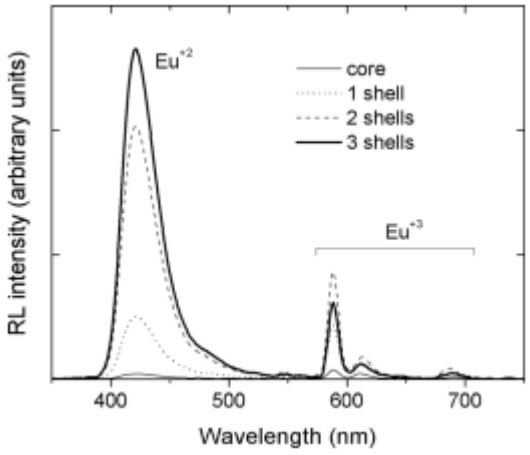


Figure 2.3.3: Radioluminescence data demonstrating the effect of coating small particles of $CaF_2$:Eu with $CaF_2$ [105].

## 2.4 Beta Particle Simulations

Heterogeneous scintillators have been modelled before for pixelated X-ray detection [107, 108] and pixelated alpha detection [109]. The results from those show that the spacial resolution comparable to direct semiconductor detection can be maintained, with increased detector efficiency. An example of the geometry of one of these detectors can be seen in Fig. 2.4.1, here the substrate is polycarbonate with ZnO nanowires and either matched with a PMT or CCD. Simulations were utilised [109, 107] to optimise the scintillator diameter, separation and detector thickness to guide the design process.

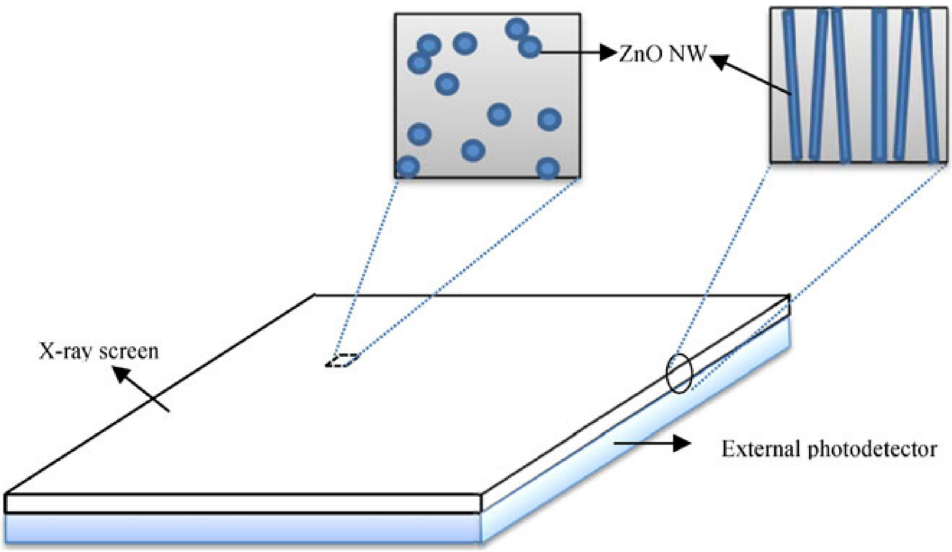


Figure 2.4.1: Diagram of the ZnO nanowire structure used for X-ray detection [109].

Simulations covering a heterogeneous geometry with alpha particles have been written [110] and the associated code can be viewed in the document [110]. The geometry was defined to be an Face Centred Cubic (FCC) unit cell with spheres, the initial positions of the alpha particles were described by either in the void between spheres,

or on the surface of the spheres. The results highlighted that for the alpha particles that occupy the void between spheres the small radius produced an increase in the deposited energy. Monte-Carlo code simulating both alpha and beta particles for a heterogeneous scintillator of fabricated scintillating fluors [111, 112] has been written and run previously. In these, two geometries were examined: Hexagonal Close Pack and Cubic Close Pack, this was to calculate the energy deposited into the scintillators. The results highlighted that reducing the scintillaing particle radius increased the energy deposited. Both of these codes however are quite limited, partly due to the restricive definitions of geometry.

Simulations involving the Monte-Carlo transport code PENELOPE2000 has been carried out for heterogeneous scintillators [113], in this case to specifically to model a flow cell detector. The geometry here focused around a 3D packing arrangement using Square Packing (SP), Body Centred Cubic (BCC), Cubic Close Packing (CCP) & Hexagonal Close Packing (HCP). These structures were made with 1000 spheres of a scintillating material, see Fig. 2.4.2. Several radionuclides were modelled using monoenergetic beta particles, those being tritium (18.6 keV), carbon 14 (160 keV), nickel 63 (67 keV), strontium 90 (550 keV), yttrium 90 (2200 keV), technetium 99 (292 keV) and promethium 147 (224 keV). A number of variables were investigated with the aim of maximising the energy deposition into the scintillator:

- Porosity
- Radius
- Packing arrangement

- Density
- Energy

The radii examined were 0.5 µm to 800 µm with the scintillating materials being CsI:Tl, $CaF_2$ and polystyrene. The conclusions for low energy beta particles, defined here as <180 keV, were that the variables sphere radius, packing arrangement, density and particle energy all had an impact on the energy deposition. The results showed that in order to maximise the energy deposition from a low energy beta particle various factors can be optimised. These optimisations are a small radius, cubic close packing and a low density scintillator (to reduce backscatter) [113].

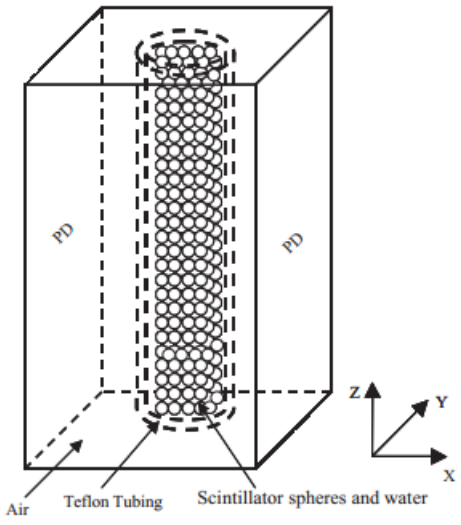


Figure 2.4.2: Modelling geometry of the flow cell detector, PD indicates a photodetector [113].

# Chapter 3

# Radiation Transport

This chapter gives an overview of the transport behaviour of beta particles including a brief description of the physics.

The radiation transport simulations used in this thesis were written and ran using Geant4 which is a Monte Carlo transport code distributed for free by CERN [114]. Geant4 is capable of simulating a range of particles such as neutrons [115], muons [116] and beta particles. When it comes to simulating the beta particle from a tritium decay, Geant4 is an ideal transport code compared to other codes such as Penelope or MCNP. Geant4 has numerous advantages for this thesis. Examples are that Geant4 can generate and track scintillation optical photons, handle complex geometries, e.g. importing from CAD, Constructive Solid Geometry & Boundary Representative Solids. Geant4 also has an advantage in that the user can choose and design which physics processes are used and their associated accuracies, as part of this, Geant4 includes multiple electron electromagnetic physics models. A few of these are

valid to low energies: Livermore; Penelope; G4DNA; Option 4 & Low Energy. Livermore specifically has two models for electrons, G4LivermoreIonisationModel and G4LivermoreBremsstrahlungModel, both of which are applicable down to $\sim$10 eV [117, 118, 119, 120, 121, 122, 123, 124]. The model itself is built from evaluated data libraries [125]. Geant4 has two classes to handle the generation of particles, namely, G4GeneralParticleSource and G4ParticleGun. Due to the greater flexibility in handling particle generation, G4GeneralParticleSource has been used throughout. The simulations in this chapter were completed using Geant4 version 10.3 on the CentOS 7 VM [114].

## 3.1 Physical Processes

This section aims to provide a basic explanation of the behaviour of beta particles/electrons in matter, i.e. scattering by the atomic nucleus. It will be assumed during this chapter that the electrons will be low energy, akin to those from a tritium decay which has a kinetic energy up to 18.6 keV.

### Elastic Scattering

Elastic scattering is the scattering by either the nucleus or an orbiting electron where the incident particle does not lose any energy. As electrons primarily interact with the electromagnetic force [126] it is the electrostatic force [127, 128, 129] between it and the nucleus or orbiting electron responsible for elastic scattering. When scattering

from the nucleus, the closer the incident particle gets, the larger the scattering angle. This gives rise to Back Scattered Electrons where the scattering angle is close to the incident path [130]. A diagram of this type of scattering is shown in Fig. 3.1.1a.

### Inelastic Scattering

Inelastic scattering is the scattering by either the nucleus or an orbiting electron where the incident particle transfers some of its energy to the other particle/s. The inelastic scattering can occur between either an orbiting electron or the atomic nucleus and is due to electrostatic forces. The inelastic scattering could occur with an orbiting electron, leading to excitiation, ionisation & Auger electrons [131, 132], if ionisation, the resulting free electron leads to further ionisation events it is a Delta Ray [133]. These interactions are collectively called Collisional Stopping Power. Radiative Stopping Power is another component of inelastic scattering, here the incident particle undergoes an acceleration due to change in direction where the energy loss is in the form of a photon [134]. This interaction is called Bremsstrahlung and whilst it can occur with either the nucleus or an orbiting electron, it is more likely with the atomic nucleus [135]. A diagram of this can be seen in Figs. 3.1.1b and 3.1.1c.

Of the possible interactions described above the most likely for a low energy electron is ionisation [136].

When the electron moves through matter, the various interactions lead to scattering. When compared with other particles from radioactive decays, such as alpha, neutron and gamma particles, the electrons scattering angles are greater. These increased scattering angles lead to a greater discrepency between the total distance the particle

travels and its assumed straight line distance [137, 138, 129, 139], see Fig. 3.1.2.

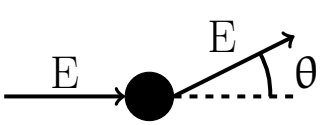


(a) A diagram of elastic scattering of an electron.

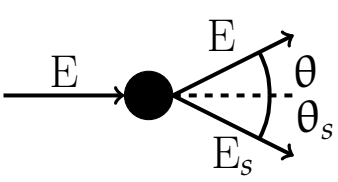


(b) A diagram of inelastic scattering with an atomic orbiting electron.

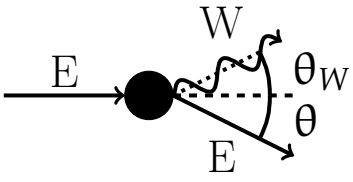


(c) A diagram of inelastic scattering creating a bremsstrahlung photon.

Figure 3.1.1: Diagram of (a) electron processes elastic scattering, (b) inelastic scattering and (c) inelastic scattering creating a Bremsstrahlung photon. Here the incident electron is labelled $E$ with scattering angle $\theta$, the scattered orbiting electron $E_S$ and associated angle $\theta_S$, the Bremsstrahlung photon $W$ with angle $\theta_W$. Adapted from [140].

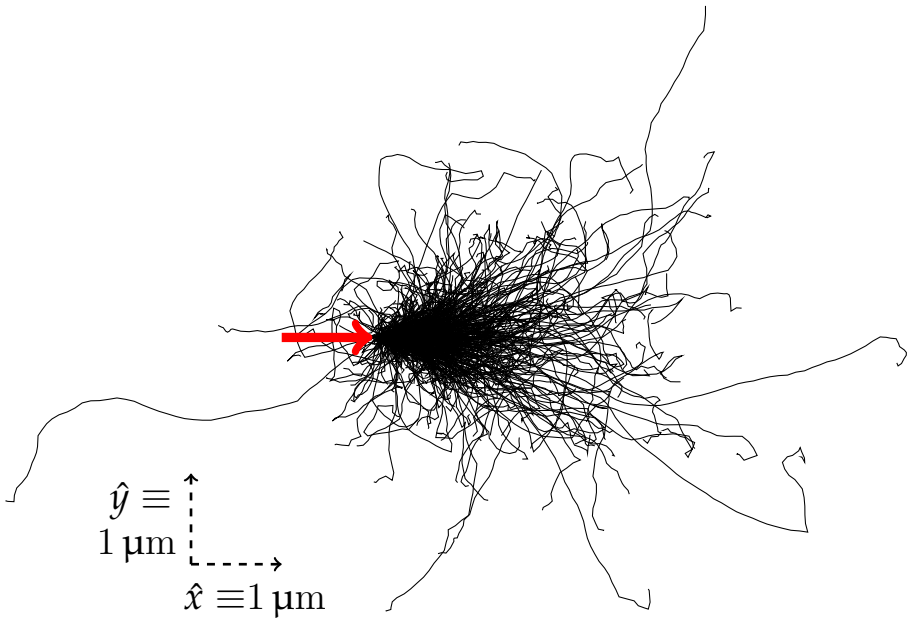


Figure 3.1.2: A diagram of the tracks of 1,000 $^3$H beta particles/electrons through water using Geant4, the $\hat{z}$ axis has been simulated but not plotted. Employing the same physics options as in Chapter 3.2, and also the same definition of water. There is an upper limit placed for each step to 100 nm, the red arrow indicates the direction of the beam.

## 3.2 Range

As mentioned in the previous section, there is a discrepency between the total path travelled and the total straight line distance due to scattering effects. This scattering effect is pronounced in tritium decay due to the low kinetic energy of the emitted particles, resulting in a short effective penetration or straight line distance. The true total path length (including scattering effects) the particle travels will be referred too as the track length and the total straight line distance as the geometric track length.

As the tritium to be detected is contained in water, the emitted beta particle will interact with the water, resulting in attenuation. This attenuation is a result of the energy loss to the particle, meaning that the track length between emission and detection ought to be minimised in order to maximise detection efficiency. To investigate the track length and geometric track length a Geant4 simulation has been written. Here a beam of electrons was fired through a cubic block of water. The energy spectrum of the beta particles was described using a 1000 bin histogram extrapolated from reference data of the tritium beta particles [17] (see Fig. 2.1.1). The water was defined as $^{1}H_{2}{}^{16}O$ with a density of $1\,\mathrm{g\,cm^{-3}}$, and a total of 1x$10^{6}$ particles examined. For increased accuracy in the simulation, the physics models used were eIonisation and eBremsstrahlung from the Livermore package and the default eMultipleScattering model. The results were analysed using a histogram and are located in Fig. 3.2.1, where the plotted errors are calculated as $\sqrt{N}$ where N is the number of particles in each bin. The data reveals that the maximum path lengths are $3\,\mu\mathrm{m}$ and $7\,\mu\mathrm{m}$

for geometric track length and track length respectively. In the previous chapter, Chapter 2.2, it was shown that a non-hygroscopic scintillator is ideal for detection of the beta particle. Whilst it is possible to protect a hygroscopic scintillator with an additional layer, this would increase attenuation, reducing the energy upon entering the scintillator. Therefore the scintillator $CaF_2$:Eu, is a good scintillating material candidate, the same simulation was then repeated with identical geometry where the medium was changed to $CaF_2$:Eu (Fig. 3.2.1). The properties for it used $Ca_1F_2$ and Eu from the Geant4 NIST definition [141], with the Eu doped to 2% (2% mass). The results show maximum track lengths and geometric track lengths of 2 µm and 1 µm. The track lengths for air have also been examined, air being 70% $_7$N (14.01 g mol$^{-1}$ molar mass) and 30% $_8$O (16.00 g mol$^{-1}$ molar mass). The results, Fig. 3.2.2, show maximum lengths of 10 mm and 5 mm for track length and geometric track length. As can be seen for the data presented, all the track lengths are very short, which is due to the low energy of emission and the attenuation from the medium. The short range makes detection inherently very difficult as beyond ∼1 µm from the surface the detector is effectively 'blind'. Any dead layers or protective layers will attenuate the particles reducing the energy, before the particle has reached the scintillator.

The maximum ranges were stated above, however the probable upper range is <0.3 µm for both water and $CaF_2$:Eu, and <400 µm for air. The above maximum track length values can be seen in Table 6.6.1 in Chapter 6. Later chapters utilise other radionuclides, $^{36}$Cl, $^{14}$C & $^{210}$Pb and the track length data for these is included in the Appendix A.1.

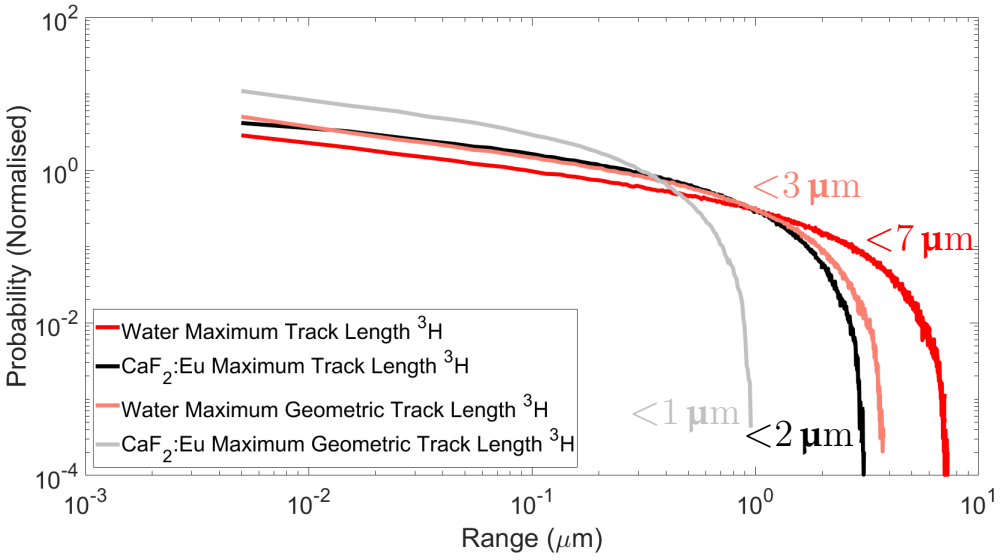


Figure 3.2.1: Data showing the range of tritium ($^3$H) beta particles in both water and $CaF_2$:Eu. Error bars are plotted but are of small magnitude and the colour of the maximum values is associated with the curve it relates to.

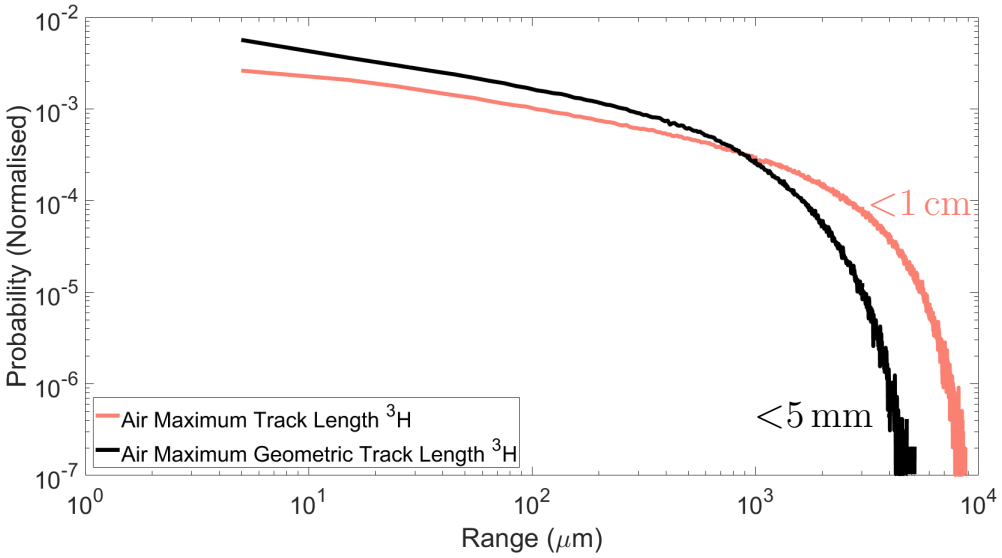


Figure 3.2.2: Data showing the range of tritium ($^3$H) beta particles in air. Error bars are plotted but are of small magnitude and the colour of the maximum values is associated with the curve it relates to.

## 3.3 Conclusions

Both sections of this chapter have shown how the electron/beta particle interactions and their scattering leads to the particles range. This, combined with the low energy from the tritium decay leads to a very short range. This short range means that any attenuation must be minimised in order to maximise detection efficiency. Therefore the inorganic non-hygroscopic scintillator $CaF_2$:Eu is still a suitable candidate for the scintillating material as it does not require an additional coating to stop it dissolving. The maximum straight line distance the particle will travel in water is $<0.3\,\mu m$ ($\sim$99% of the electrons) which is an inherent difficulty in waterborne tritium detection as any beta particle emitted further than this away from a scintillator will not be detected.

# Chapter 4

# Single Crystal Scintillation Detector

## 4.1 Introduction

In Chapter 2.3, $CaF_2$:Eu was determined to be the ideal scintillator for detecting waterborne tritium. This chapter then investigates the efficiency and limitations of using a homogeneous, single crystal inorganic non-hygroscopic scintillator, specifically $CaF_2$:Eu. This particular chapter covers experimental data, simulations results and numerical analysis, which culminates in the comparison of experimental data with a model of the detector setup. The conclusions were used to inform the design of the heterogeneous scintillator in later chapters.

## 4.2 Experimental Detector

For the reasons given in Chapter 2.3 the scintillator $CaF_2$:Eu has been selected as the best scintillating material for detecting the beta particles from a tritium decay. Once the beta particle enters the scintillator the process of scintillation will produce optical photons. There are a number of photon detection technologies, PhotoMultiplier Tubes [142], Silicon PhotoMultiplier (SiPM) [143], Avalanche Photo Diode (APD) [144], CMOS/CCD [145, 146] etc. The SiPM was selected [147] as it has a lower operating voltage (29.7 V) when compared with a PMT (1-2 kV) and compact size. The model selected was a Sensl C-Series 60035 [148]. As the overall motivation of the thesis is an in-situ detector, the SiPM appears to be the ideal.

A preliminary experiment was conducted to examine the shape of the pulse from the SiPM. For this experiment a Cobalt 60 source was chosen [149, 150]. This particular $^{60}$Co source was sealed, with an activity of ∼38.11 kBq, diameter of ∼3 cm and decays with both $\beta$ (317.32 keV) & $\gamma$ (1332.508 kBq) [150]. The only circuitry employed was a power supply to bias the SiPM, see Fig. A.2.1 in the Appendix A.2. Thirty pulses were captured using an oscilloscope, averaged (Fig. 4.2.1), then curve fitted. Circuit analysis [151] suggested that the output pulse should take a particular exponential form, as shown in Eq. 4.2.1. After fitting to the values, $a$ & $b$ were found to be $2.381\times10^{-7} \pm 1.085\text{x}10^{-9}$ s and $7.443\times10^{-7} \pm 2.283\text{x}10^{-9}$ s respectively [151]. The values $a$ and $b$ above are constant and not dependent on the energy of the radiation, the equation (Eq. 4.2.1) is used in the model further into this chapter to predict the

output current given a known pulse amplitude.

$$i(t) = c(exp(-t/a) + exp(-t/b)) \tag{4.2.1}$$

For the experiments into waterborne tritium detection the scintillator $CaF_2$:Eu was

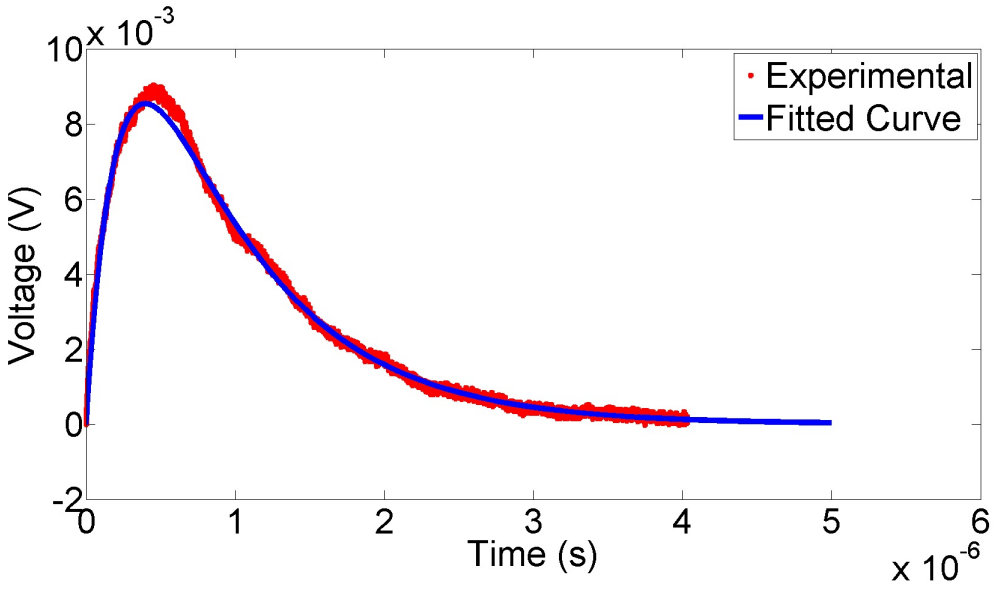


Figure 4.2.1: Data showing a comparison a peak due to the $^{60}$Co source from the SiPM with the equation Eq. (4.2.1).

brought from Hellma [83] and measured 28.6 mm in diameter with thickness of 1 mm. During the experiments the scintillator was in contact with the tritiated water with a cylindrical volume of 20 mL, concentration 1500 Bq mL$^{-1}$, resulting in an activity of 30 000 Bq. The cylinder itself had a radius of 2.5 cm and height of 2.5 cm. This volume of tritiated water was compared in a subsequent experiment with a background of de-ionised water, itself having a volume of 20 mL. Another radioisotope, a sealed source of Chlorine 36 ($^{36}$Cl), was picked to compare with tritium. $^{36}$Cl only decays with a beta emission, albeit at a higher energy than tritium (708.6 keV [152, 153])

making it useful to compare and calibrate with. Throughout the following experiment, the scintillator itself was optically coupled to the SiPM using optical gel, when the tritium source was in use it was in contact with the scintillator, i.e. no air gap (see Fig. 4.2.2). The $^{36}$Cl sealed source was placed with a $\sim$1 mm air gap between itself and the scintillator surface. Each of the sources was sampled for 30 min.

The bias voltage for the SiPM was supplied from a voltage regulator, seen in Fig. 4.2.3. The output from the SiPM went through a pre-amplifier (Fig. 4.2.4) for conditioning before sampling, for this a Charge Sensitive Pre-Amplifier was used (CSP, also named a Transimpedance Amplifier, TIA). The feedback resistor and capacitor values give it a time constant of 82 ns, along with a gain of 29 for a 70 mV 1 µs pulse, and 74 for a 70 mV 10 µs. The output from the CSP was sampled with a 400 kS s$^{-1}$ 16 bit ADC, National Instruments USB-6212 and part number 780107-01 [154].

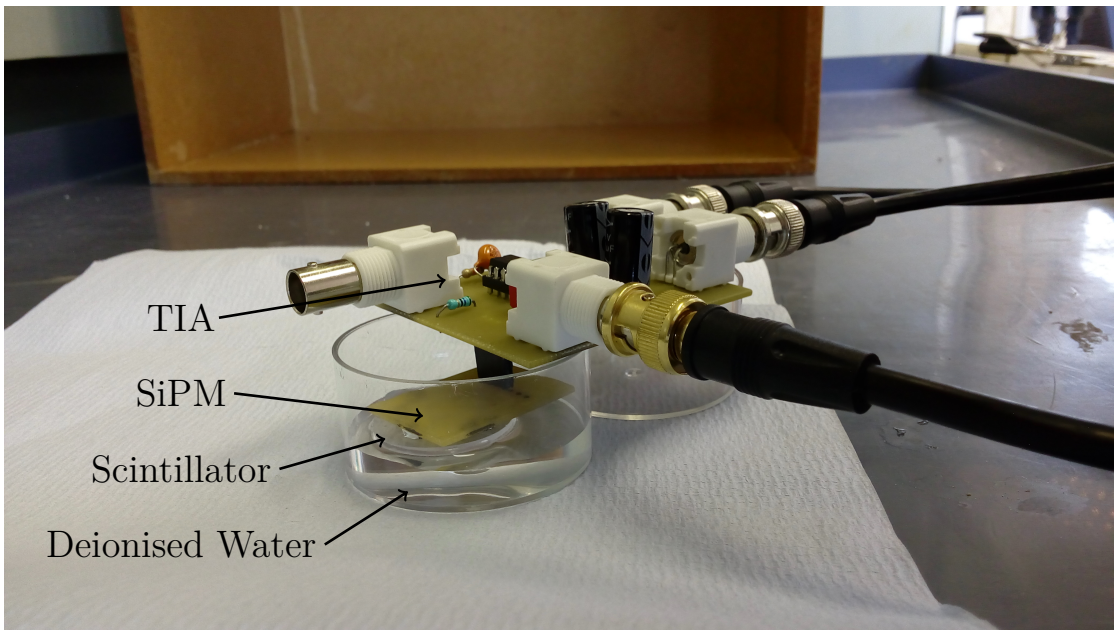


Figure 4.2.2: Photograph of the SiPM, $CaF_2$:Eu scintillator and preamplifier (TIA) used in this chapter.

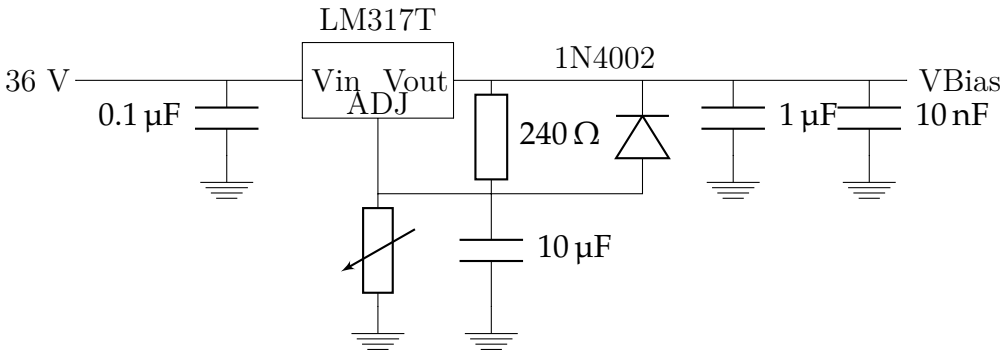


Figure 4.2.3: Circuit diagram showing the SiPM bias voltage circuit, employing the LM317T voltage regulator [155, 156]. The output *VBias* is adjusted using the variable resistor and the 10 nF capacitor is located adjacent to the SiPM Cathode pin and is present also in the SiPM Bias Figure A.2.1.

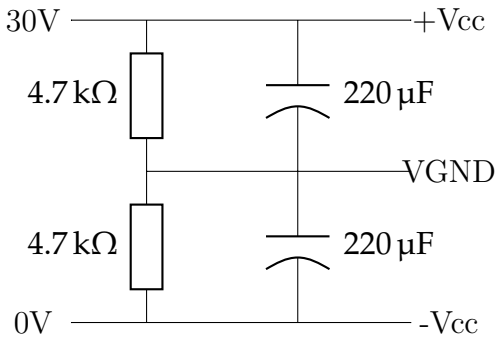


(a) Circuit diagram showing the rail splitter for powering the OP27E in Fig. 4.2.4b.

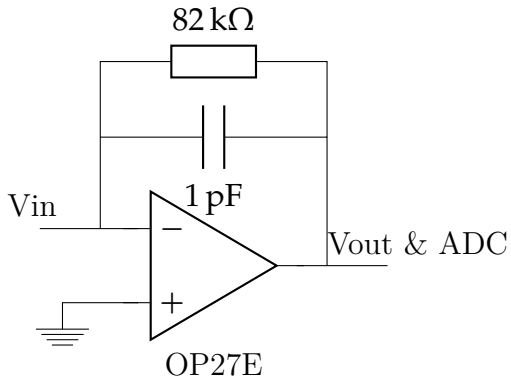


(b) Circuit diagram of a Charge Sensitive Preamplifier/Transimpedance Amplifier [157].

Figure 4.2.4: Circuit diagrams of the rail splitting and charge sensitive preamplifier circuits.

## 4.3 Simulation Model Definition

The results from the experimental detector described above were validated with a Monte Carlo simulation. This simulation was made of two parts, the first used Geant4 to model the electron transport to the scintillator and photons created to the SiPM, then a second used Matlab [158] to model the electronics. This information, coupled with circuit analysis of the SiPM [151] & preamplifier, along with fitting of one parameter allows the prediction of the detector behaviour given the exposure received.

### 4.3.1 Geant4 Simulation

The Geant4 simulations for both tritium and $^{36}$Cl were completed using two virtual machines, Geant4 version 10.1 was employed for the validation of the detector model ( Figs. 4.4.5 and 4.4.6) and Geant4 version 10.3 was used for the other data and figures. The simulation code was the same for both versions.

#### Geant4 Physics

Geant4 simulations require the user to select the physics models or libraries it will use. These models and libraries represent the physical processes that a particle can undergo, and therefore should be chosen carefully for an accurate simulation. The physics models for this Geant4 simulation for electron/beta particles were,
G4eMultipleScattering, G4eIonisation and G4eBremsstrahlung from the default elec-

tromagnetic physics. The code used was as follows:

```
pmanager->AddProcess(new G4eMultipleScattering(),-1,1,1);
pmanager->AddProcess(new G4eIonisation(),-1,2,2);
pmanager->AddProcess(new G4eBremsstrahlung(),-1,3,3);
```

The three numbers in each line above are options, with the numbers indicating how the specified process is applied. The numbers represent *AtRest*, *AlongTheStep* & *PostStep* and positive numbers indicate it is active, negative number inactive [159]. The optical photons creation and transportation model were, G4OpAbsorption, G4OpRayleigh, G4OpMieHG, G4OpBoundaryProcess, G4Scintillation and G4Cherenkov.

Geant4 Geometry

Geant4 allows the user to define the geometry according to the application, here the single crystal scintillator was a cylinder with a thickness of 2 mm and radius 14.3 mm for both radioisotopes. The water volume used for the tritium was defined as a cylinder 15 mm in radius & 1 mm thick, with one surface in contact with the scintillator. For the $^{36}$Cl source, the water was removed. The remainder of the simulation was declared as air. Diagrams of these are shown in 4.3.1.

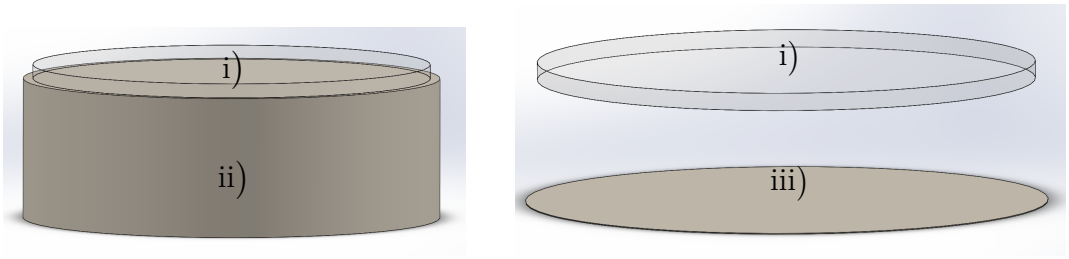


(a) Diagram of the Tritium ($^{3}$H) single crystal detector model in Geant4, not to scale.

(b) Diagram of the Chlorine 36 ($^{36}$Cl) single crystal detector model in Geant4, not to scale.

Figure 4.3.1: Diagram of the two setups used to model the single crystal detector. The scintillator is labelled as i), radius 14.3 mm and thickness 2 mm. The cylindrical water volume, ii), radius 15 mm and thickness 10 mm and, the disc iii), with radius 15 mm with an 1 mm gap from the scintillator.

Geant4 Beta Source

As mentioned above, there are two sources, tritiated water and $^{36}$Cl. The tritiated water is modelled as an isotropic volume source described as a cylinder, this is placed inside of the water volume stated in the geometry section and with one surface in contact with the scintillator. The radius of this cylinder is 15 mm with the height being varied, see Fig. 4.3.1a. The $^{36}$Cl is a disc source of 15 mm radius and placed 1 mm from the scintillator, a diagram is located in Fig. 4.3.1b. The energy spectrum for both sources was extracted from the Radiological Toolbox [17] then extrapolated to 1000 bins. The energy spectrums for tritium and chlorine are shown in Figs. 4.3.2 and 4.3.3 respectively.

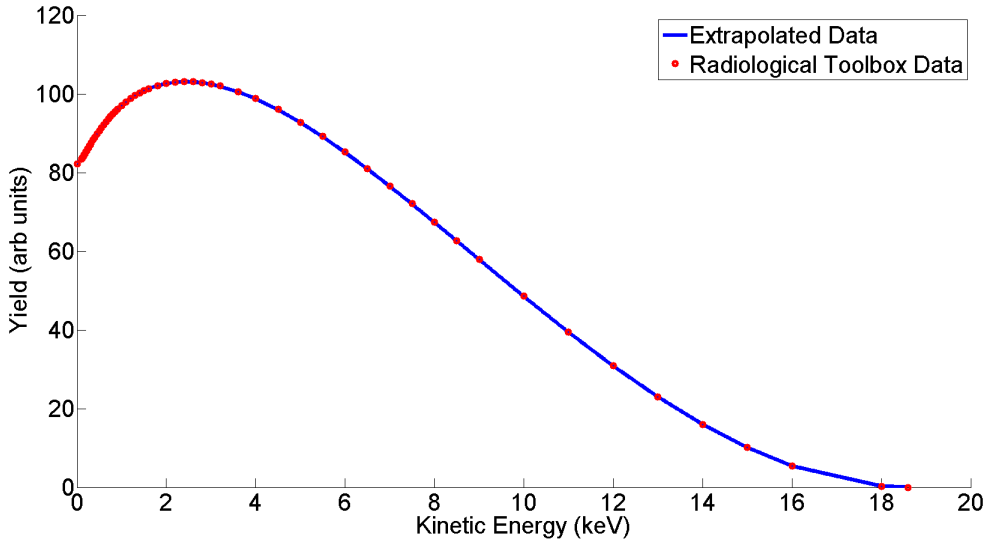


Figure 4.3.2: Energy spectrum data for $^{3}$H from the Radiological Toolbox [17], plotted with the extrapolated spectrum.

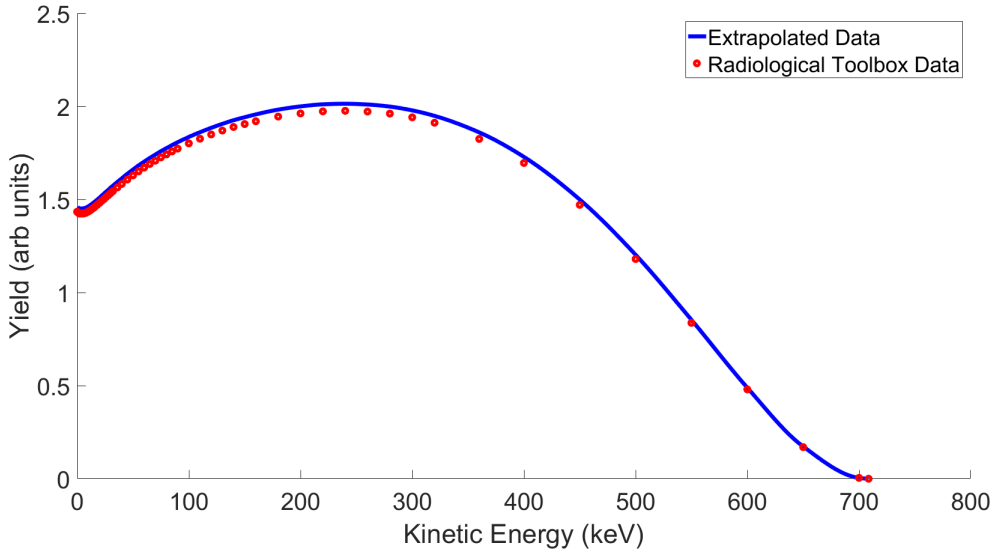


Figure 4.3.3: Energy spectrum data for $^{36}$Cl from the Radiological Toolbox [17], plotted with the extrapolated spectrum.

Geant4 Materials

Geant4 requires the user to define the material properties for all the materials in the simulation, this definition also includes other properties such as scintillation and visible photon interactions. Four materials were used in these simulations, air, water, $CaF_2$:Eu and glass.

Air was defined as 70% nitrogen and 30% oxygen, with nitrogen having an atomic number of 7 and molar mass of $14.01\,\mathrm{g\,mol^{-1}}$ and oxygen having an atomic number of 8 and molar mass of $16.00\,\mathrm{g\,mol^{-1}}$. Water was defined as two parts hydrogen and one part oxygen, with hydrogen having an atomic number of 1 and molar mass $1.00\,\mathrm{g\,mol^{-1}}$, and oxygen as stated above. $CaF_2$:Eu was defined using the NIST database for $CaF_2$ (G4_CALCIUM_FLUORIDE) and Eu (G4_Eu) with a density of $3.179\,\mathrm{g\,mol^{-1}}$ and 0.2% doping. Glass was defined using the G4_Pyrex_Glass from the NIST database.

The scintillation properties of $CaF_2$:Eu were defined using the information in Chapter 2 and Table 2.3.1 and the emission curve made of 59 points. Data showing the original data from Saint Gobain [160], the interpolated 59 point data and the scintillation emission curve from Geant4 is shown in Fig. 4.3.4.

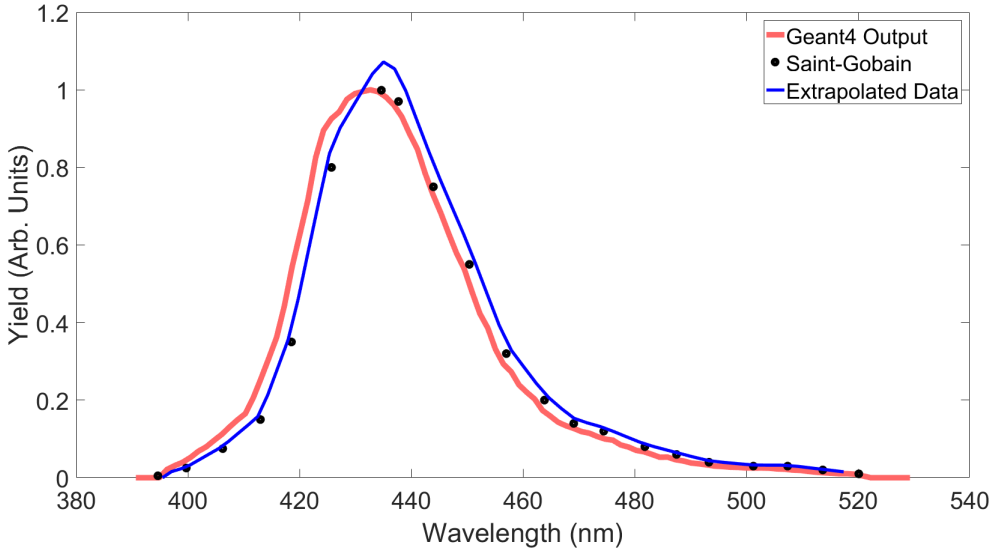


Figure 4.3.4: Showing the original data [160], extrapolated data and the resulting emission curve of $CaF_2$:Eu produced by Geant4.

### 4.3.2 Electronics Simulation

This is the second part of the simulation, the code that models the output voltage given an input of number of photons per event that arrive at the SiPM. This was written in Matlab, using circuit analysis of the SiPM and CSP [161, 162, 151] with the output pulses simplified to be only the peak amplitude. The model is shown in Eq. 4.3.1 with the terms shown in Eq. (4.3.2), (4.3.3) & (4.3.4). $G$ is the SiPM gain, $RQ$ quench resistance, $CQ$ quench capacitance and $CD$ is a capacitance value. $RS$ is the shunt resistance, $e$ electron charge ($1.602 \times 10^{-19}$ C), time $t$, $r_s$=1 k$\Omega$, $r_q$=200 k$\Omega$ and $c_q$=0.5 pF. Values $a$ & $b$ are the constants given earlier in Chapter 4.2, $N_{fired}$ is the number of SiPM microcells fired by incident photons and $F$ is the parameter to deduce from fitting. The parameter $F$ was found to be $1.8{\times}10^{19}$ through fitting the

data, giving the final equation Eq. 4.3.5 [151].

$$V(t) = F \cdot G \cdot \frac{RQ \cdot CQ \cdot CD \cdot RS}{b-a} \cdot e \cdot (exp(-t/a) - exp(-t/b)) \tag{4.3.1}$$

$$RQ = \frac{r_q}{N_{fired}} \tag{4.3.2}$$

$$CQ = c_q \cdot N_{fired} \tag{4.3.3}$$

$$CD = c_d \cdot N_{fired} \tag{4.3.4}$$

$$V(t) = 1.8 \times 10^{19} \cdot G \cdot \frac{RQ \cdot CQ \cdot CD \cdot RS}{b-a} \cdot e \cdot (exp(-t/a) - exp(-t/b)) \tag{4.3.5}$$

## 4.4 Results & Discussion

The Geant4 model described above is for the single crystal $CaF_2$:Eu scintillator to detect tritiated water. As the medium of the source of radiation is self-attenuating, the shape of the energy spectrum of the beta particles arriving at the surface of the scintillator can be distorted from the initial energy spectrum (Fig. 4.4.1). Additionally, as the beta particle source self-attenuates there will be a thickness that is representative of an infinite volume for an isotropic source beyond which emitted beta particles will never reach the detector and effectively do not exist. That is, increasing the thickness further does not impact on the energy spectrum at the single crystal scintillator surface. The optimal thickness for this is 5 µm, as the simulation data (Fig. 4.4.1) demonstrates that increasing it further does not change the curve shape. Then in any future simulations of tritiated water with an adjacent material, the optimisation is that the tritiated water need not be thicker than 5 µm.

The attenuation of the tritium beta spectrum due to the self-attenuating medium has

been predicted numerically, Appendix A.3 [151]. This numerical prediction has been validated using the same Geant4 simulation, likewise with a 5 µm thick tritiated water volume. The results are shown in Fig. 4.4.2. The data reveals that the simulation validates the theory for predicting the attenuation of the self-attenuating source of a beta radioisotope. Both Figs. 4.4.1 and 4.4.2 show that there is a shift in the average energy, note that the $\hat{y}$ axes (Probability & Yield) have been normalised. The simulation was also verified by prediction of the mass attenuation of water, Fig. 4.4.2, the details for this are located in the Appendix A.3 and Eq. A.3.5.

The attenuation of the beta particle energy spectrum also impacts the number of scintillation photons arriving at an adjacent SiPM. Figure 4.4.3 highlights how this attenuation shifts the photon distribution. Similar simulations have been used to calculate the mass attenuation of water, using the method in the Appendix A.3. The results are shown in Fig. 4.4.4.

Using the Geant4 model of the single crystal detector and both tritium & $^{36}$Cl radioisotopes, along with the model of the detector electronics a model of the entire detector can be made. Figs. 4.4.5 and 4.4.6 shows that with the parameter fitted the model is able to replicate the output from the preamplifier. For this data the error is expressed as $1/\sqrt{N}$, where N is the number of particles in each histogram bin. Both figures show a peak at the low voltage, which can be explained as noise. The data analysis method used for both figures also employed a threshold, which was set to -0.265 V during the calibration. From the tritium data in Fig. 4.4.5 there is a data point at approximately $-0.27$ V (labelled with a *), this is an erroneous peak. The

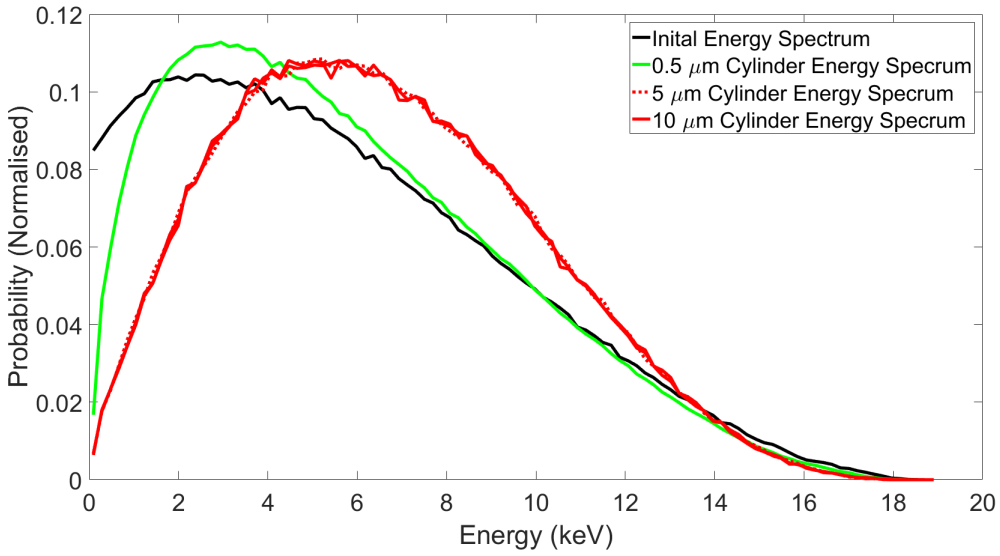


Figure 4.4.1: Data showing the energy spectrums of cylinders of tritiated water of various thicknesses incident on a single crystal scintillator.

$^{36}$Cl results ( Fig. 4.4.6) displays a peak at approximately $-0.4\,\mathrm{V}$, this is due to noise in the detector setup.

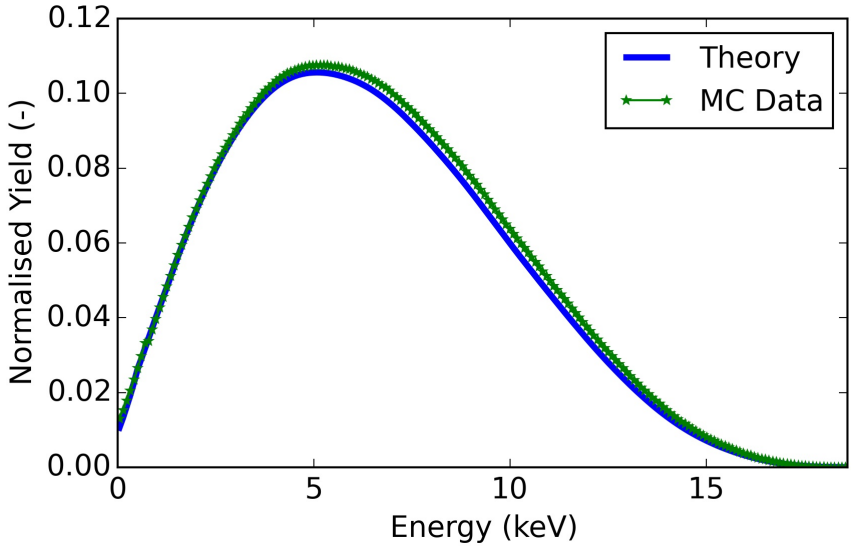


Figure 4.4.2: Data showing that the Geant4 data validates the numerical prediction of the attenuation of the tritium ($^3$H) energy spectrum [151].

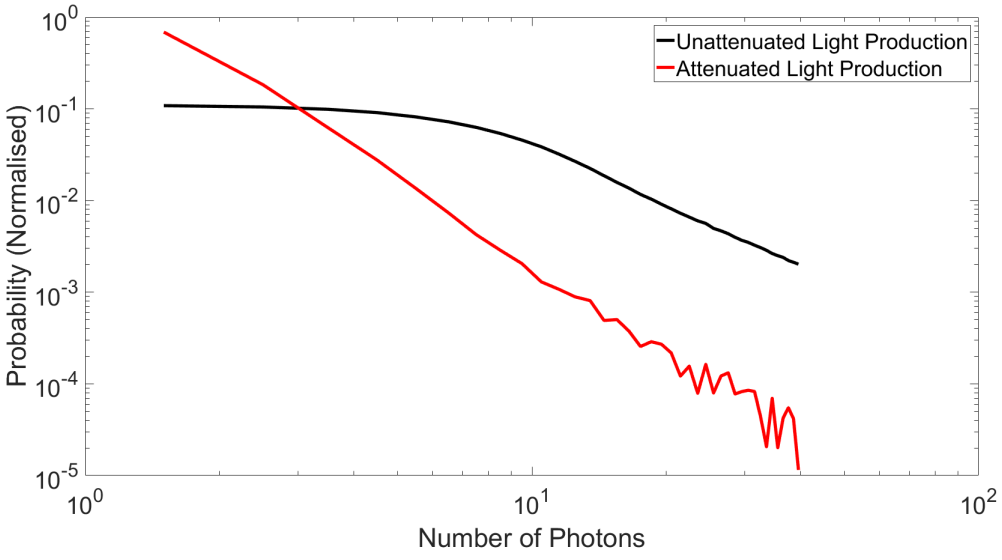


Figure 4.4.3: Data showing the histogram of photon production of both the unattenuated and attenuated (5 µm) energy spectrums for the tritium source.

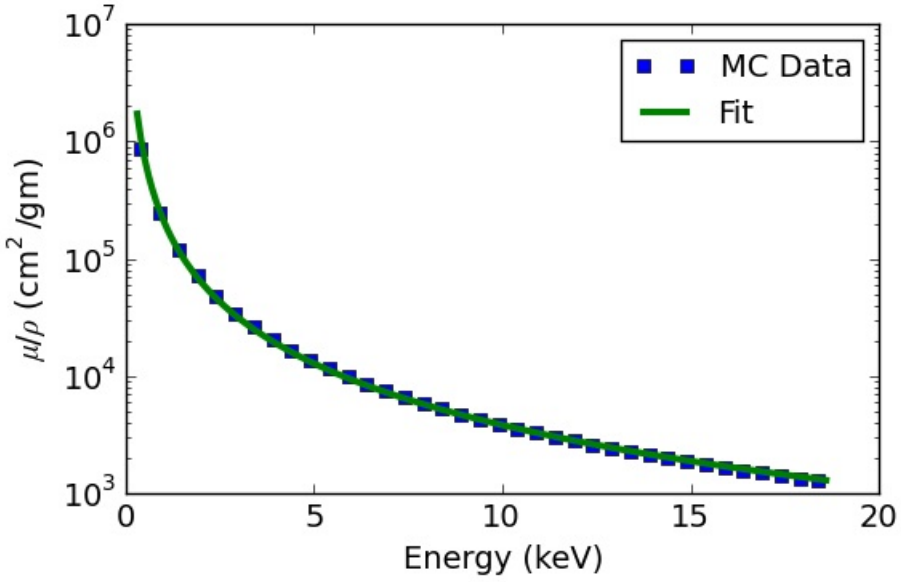


Figure 4.4.4: Data showing the mass attenuation of water as calculated using Geant4 [151].

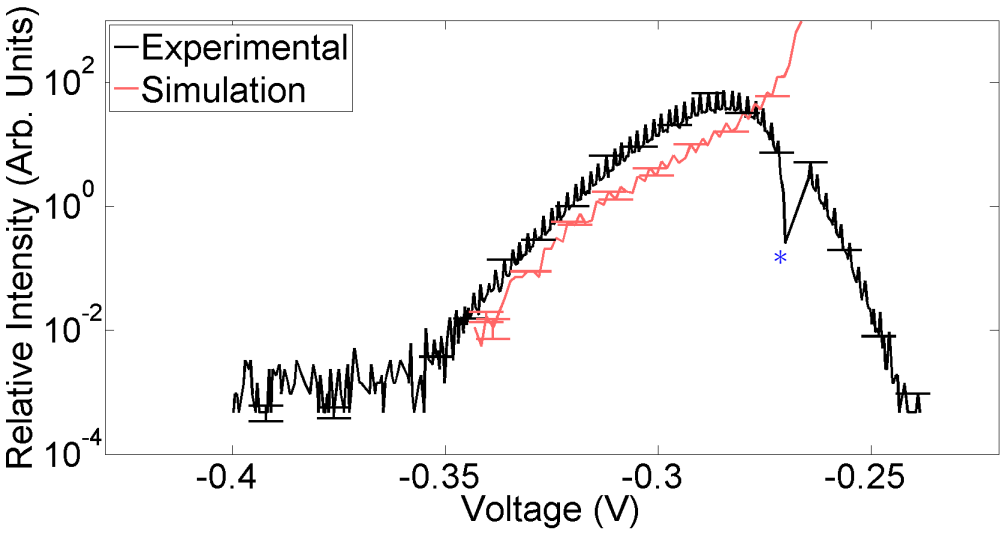


Figure 4.4.5: Data showing the experimental data and prediction using both Geant4 and circuit analysis for tritium.

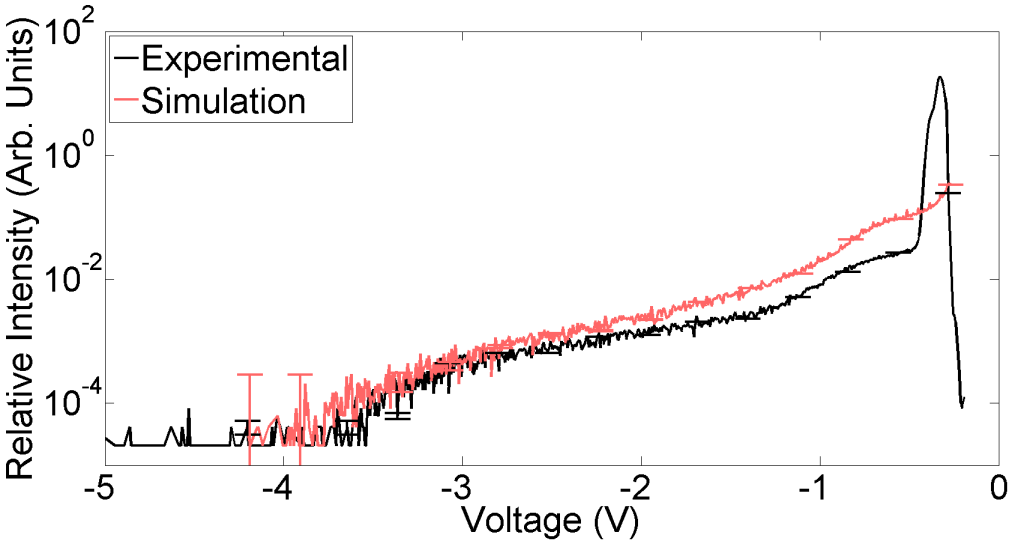


Figure 4.4.6: Data showing the experimental data and prediction using both Geant4 and circuit analysis for $^{36}$Cl.

## 4.5 Conclusions

This chapter has provided a number of useful results. First that the output pulse from an SiPM takes a particular form, with the time constants shown to be independent of the kinetic energy. For simulating a volume of source tritium with a single crystal scintillator, the results showed that a volume 5 µm thick can be assumed to be effectively 'infinite'. Therefore for any future simulations the distance from the surface of the scintillator for an isotropic self-attenuating volume of tritium is 5 µm. The attenuation data, both Geant4 simulation and numerical analysis, show that the energy spectrum of the beta particles arriving at the scintillator has changed. This matters as the expected energy spectrum for a detector has to account for the self-attenuating source itself. This shift in the energy spectrum is accompanied with a change in the distribution of the photons arriving at an adjacent SiPM. By employing

a combination of both the Geant4 simulations, a model of the detector & preamplifier and an additional radioisotope ($^{36}$Cl), a model of the entire detector has been made. This model had a single parameter fitted using both radioisotopes where the data was a histogram of pulse heights.

# Chapter 5

# Heterogeneous Scintillator Fabrication

## 5.1 Introduction

The previous chapters have highlighted the difficulty in detecting waterborne tritium, such as the low range of the beta particle in water. A novel approach to improve the detection efficiency of waterborne tritium will be covered in the next chapter through a development of a new heterogeneous scintillator. However the explanation of this novel approach relies on a separate body of work, which will be the content of this chapter. This chapter covers the fabrication of the heterogeneous scintillator material. Two methods were attempted, the *Chemical* and *Granulation*, only the Granulation method yielded successful results.

## 5.2 Preexisiting Fabrication Methods

### 5.2.1 Chemical

There are many available methods for fabricating nanometer & micrometre sized particulate $CaF_2$:Eu in the literature. The predominant method is utilising a chemical approach, these methods will be reviewed in this section.

The Reverse Micelle Method [163] has been used to produce both undoped $CaF_2$ and doped $CaF_2$:Eu. The process involved a number of solutions to form the end product, starting from a Ca solution. This was mixed with an Igepal-520 & cyclohexane solution, rare earth dopant added and EtOH (co-surfacant). The final step was the addition of a HF, cyclohexane and Igepal-520. After being left for two hours the result was centrifuged, washed and dried before characterisation. The XRD and TEM analysis [163] demonstrated the presence of $CaF_2$ with dopant, average particle diameter 20 nm and homogeneous chemical composition. Once the particles were annealed that analysis revealed a reduction in surface contamination, e.g water.

The process of Electrodeposition [164] has been investigated for producing undoped $CaF_2$ particles and those doped with Eu & Tb. An initial solution of $CaCl_2$, EDTA & Sodium Ascorbate was used, to this $NH_4F$ was added, as well as NaOH to control the pH. The electrodeposition used a three electrode cell controlled by a potentiostat to complete the procedure. Analysis of the resulting material showed small particles with diameters of $\sim$500 nm. The dopants were distributed over the material and dis-

played the expected single emission peak.

$CaF_2$:Eu can also be made in nanometer sized particles using a process of Precipitation [165, 166]. This begins with two solutions, the first is $NH_4F$ and a ligand, ammonium di-*n*-octadecyldithiophosphate (ADDP), which is in 1:1 mixture of ethanol and water. The second solution contained ($Ca(NO_3)_2{\cdot}4H_2O$ & $Eu(NO_3)_3{\cdot}6H_2O$ which are sources of Ca and the Eu doping in water. The first solution was added drop-wise into the second, and after stirring the precipitates were washed in ethanol and water. XRD characterisation revealed that $CaF_2$:Eu was produced [165, 166], TEM analysis identified that the particles size average diameter of $10 \pm 2$ nm. The radioluminescence results demonstrated three peaks, one at 420 nm for $Eu^{2+}$ and the others at 590 nm and 620 nm for $Eu^{3+}$. $CaF_2$ & $CaF_2$:$Eu^{3+}$ nanometre sized nanocrystals have been fabricated through the Hydrothermal method [167, 168]. This starts with $CaCl_2$ in de-ionised water, with the addition of $NH_4F$ and stirring. This was placed in an autoclave for 24 h at a temperature of 160 °C, then centrifuged and washed. XRD results confirmed the production of $CaF_2$, however luminescence measurements highlighted the presence of defects. During this method it was noted that the pH affected the particle size and size distribution.

Chemical co-precipitation as a technique to create nanometre sized particles of $CaF_2$ & $CaF_2$:$Eu^{3+}$ has led to successful results [169, 168]. This method involves $CaCl_2$ & $EuCl_3$ in ethanol and $NH_4F$ being added, then left to stir. Completing this in ethanol is advantageous when compared to water as $NH_4F$ is less soluble, which makes con-

trolling the $CaF_2$ easier [169]. XRD results demonstrated the formation of $CaF_2$:Eu, and TEM results showed that using water the particle diameters were ∼30 nm to 35 nm and ∼15 nm to 20 nm when using ethanol.

Vacuum deposition is a technique for producing a sheet of $CaF_2$:Eu [170]. The powders $CaF_2$ and $EuF_3$ were mixed under nitrogen, charged into a graphite crucible. This was heated to 500 °C, then melt flowed under argon gas. Held for 4 hours, cooled back to room temperature and finally under a vacuum ($3 \times 10^{-4}$ Pa) deposited onto fused silica glass. Using XRD the layer was confirmed to be $CaF_2$:Eu.

The Sol-Gel method has been used to produce $CaF_2$:Eu nanometre particles [171, 170, 172, 173], Figs. 5.2.1 and 5.2.2. This starts with the Ca precursor $Ca(OLac)_2 \cdot 0.2H_2O$ and the europium precursor $Eu(CH_3COO)_3$ being dissolved in methanol. To this, HF was added to provide the fluorine, after mixing trifluoroacetic acid (TFA) & tetramethyl orthosolicate (TMOS) was added to stablise the solution. Alternatively $Ca(OH)_2$ & $Eu(CH_3COO)_3 4H_2O$ in a solution of ethanol, water and TFA. The characterisation of the methanol based method yielded particles of $CaF_2$:Eu as confirmed by XRD and size analysis concluded with ∼10 nm. The method using ethanol and water found that after sintering at 300 °C to 700 °C the particles were $CaF_2$:Eu with sizes ∼100 nm.

The sintering/annealing has been utilised as a successful method of reducing $Eu^{3+}$ to $Eu^{2+}$ [172, 174], including in an air environment [175]. The impact of surface roughness on a Bismuth Germanate scintillator and its performance has been investigated

[176] and the result showed that the difference between a polished and rough surface was minimal. Therefore, the surface finish of any produced scintillator should have only a minimal impact on its performance.

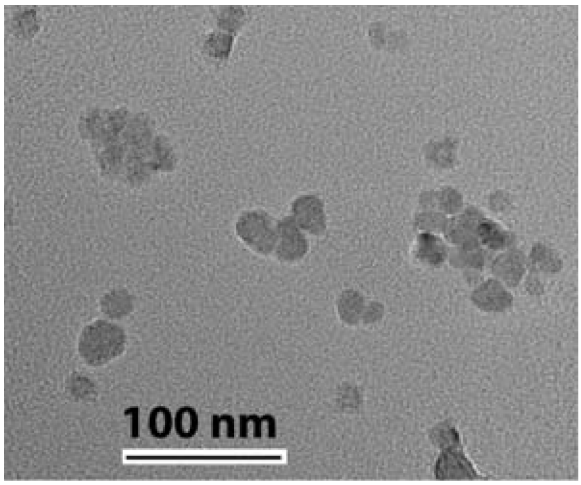


Figure 5.2.1: TEM image of $CaF_2$:Eu particles coated in $CaF_2$, fabricated using the sol-gel method [165].

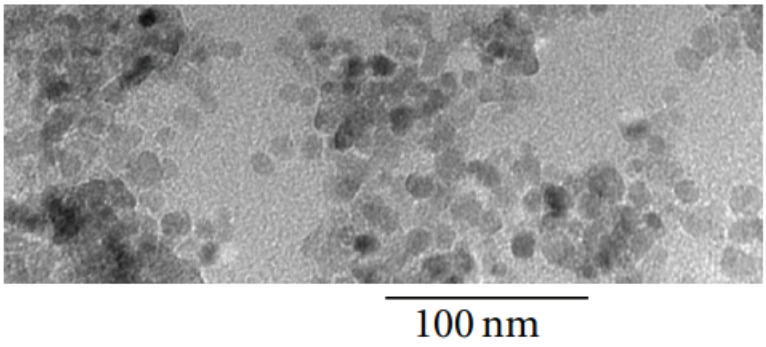


Figure 5.2.2: TEM image of $CaF_2$:Eu particle fabricated using the sol-gel method [166].

### 5.2.2 Granulation

As stated in Chapter 2.3.2 the nomenclature for the use of particles of a scintillator material is unclear. Here the term Granulation is used to refer to a purely mechanical method of producing the particles, as opposed to the chemical approach. This is consistent with literature where a granulated scintillator is often referred to as one that has been made into a powder. The method preferred is the ball milling machine [177, 178], however the mortar & pestle has been explored too [179, 180]. Unfortunately little information is available in regards to the production of a heterogeneous scintillator using a mechanical method. There is information on the ball milling of $CaF_2$ and how the nanocrystalline structure compares with the chemical approach [181, 182]. Specifically the ball milling of $CaF_2$ powder was compared with small crystals grown from $CaCO_3$ & $NH_4F$. The resulting materials were characterised through XRD, NMR,TEM and SEM, with the conclusion that the nanocrystalline structures were nearly identical. Examples of granulated scintillators produced by ball milling are shown in Figs. 5.2.3 and 5.2.4. Whilst little data exists for the accurate process of granulating a scintillator, this is likely due to the positive correlation relationship between milling time and average crystallite size [177].

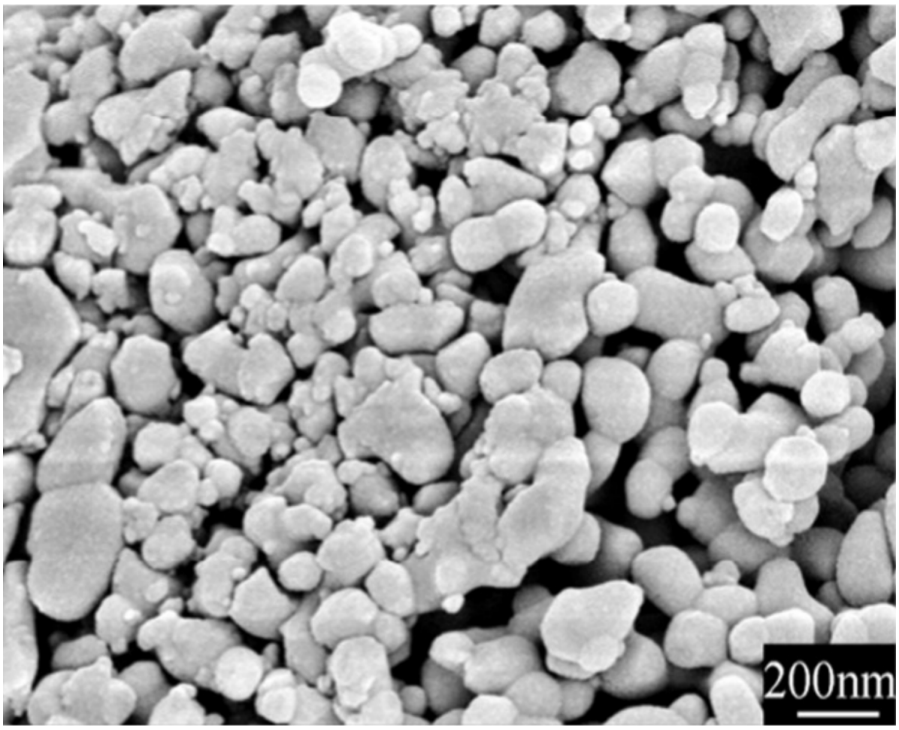


Figure 5.2.3: SEM image of ball milled Yb:YAG [177].

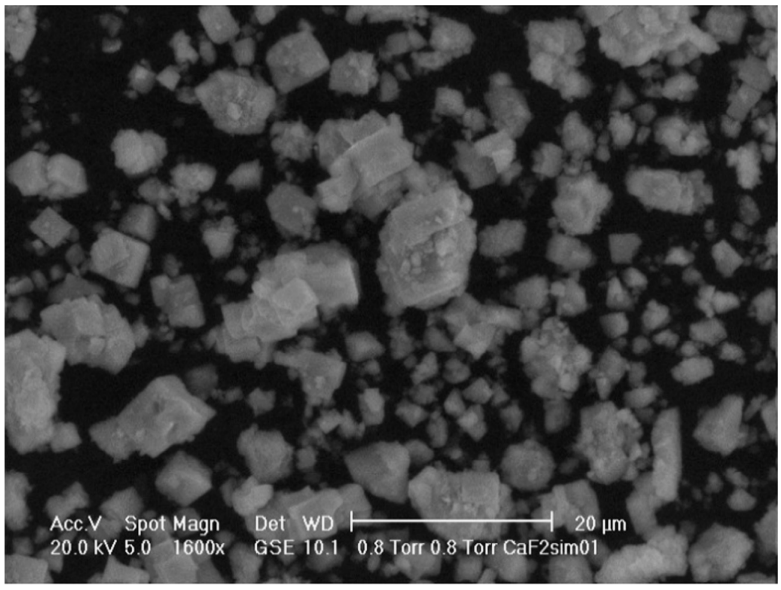


Figure 5.2.4: SEM image of spherical ball milled $CaF_2$ [182].

### Summary

Whilst there are many methods of fabricating $CaF_2$:Eu into small particles through the chemical approaches, some are not suitable due to the method, such an example is vacuum deposition [170], or the use of hazardous chemicals like HF. There are a number of methods that have a similar approach, hydrothermal, chemical co-precipitation & sol-gel appear to lead to the best results Figs. 5.2.1 and 5.2.2. All the current methods target small particles, $\sim$10 µm to 100 µm. However this is a limited range and if an ideal particle size exists, it could lie outside of that particular range. The granulation method will create particles of the correct chemical composition, however the size distribution of mortar & pestle crushed $CaF_2$:Eu is unknown. Both methods shall be attempted to find the ideal for this specific application.

## 5.3 Particle Fabrication Method: Chemical

This section details the chemical approach used in the endevour to fabricate small particles of $CaF_2$:Eu.

### 5.3.1 Method

The method of using reagents to produce the $CaF_2$:Eu particles used the reagents listed in Table 5.3.1. Throughout the various experimental series the solvents utilised were de-ionised water, ethanol, methanol and acetylacetone.

Table 5.3.1: The list of the reagents used as the precursors to produce $CaF_2$:Eu [183, 184, 185, 186].

| Precursor | Element | Formulae | Molecular Weight ($g\,mol^{-1}$) |
|---|---|---|---|
| Calcium L-lactate Pentahydrate (Unknown Purity) | Calcium | $[CH_3CH(OH)COO]_2Ca \cdot 5H_2O$ | 308.29 |
| Ammonium Fluoride ($\geq$99.99%) | Fluoride | $NH_4F$ | 37.04 |
| Europium Acetate Hydrate (99.9%) | Europium(III) | $Eu(CH_3CO_2)_3 \cdot xH_2O$ | 329.10 (anhydrous) |
| Chemical | | | |
| Tri-Sodium Citrate (99%) | | $Na_3C_6H_5O_7 \cdot H_2O$ | 294.10 (258.07 anhydrous) |

An experiment into the impact of annealing was conducted using $CaF_2$:Eu. The results to this are shown in Figs. 5.3.4, 5.3.5 and A.4.1 to A.4.3. A total of 1 g of $CaF_2$:Eu of stoichiometric amounts was produced with the europium doping at 1%. 1 g $NH_4F$, 4 g calcium L-lactate & 400 mg europium acetate was employed along with the solvents 80 mL methanol and 10 mL acetylacetone. Stirring was completed at ambient temperature and the mixture was deposited onto the substrate using a spray-gun

and hot plate, which itself was maintained at 200 °C. After spray deposition the substrates were left to cool before being placed in a furnace to anneal for 2 h at either 600 °C or 700 °C.

An experimental series involving a fixed concentration of $CaF_2$ and a fixed annealing temperature to find both the ideal annealing time and spray deposition hot plate temperature was completed. The concentration was 0.1 M (0.1 mol dm$^{-3}$) with an annealing temperature of 700 °C, the annealing time then varied through 0 min, 30 min, 60 min, 90 min, 120 min and 150 min and the hot plate temperature varied through 150 °C, 200 °C, 250 °C, 300 °C, 350 °C and 400 °C. Here the precursors included $NH_4F$, Ca-Lactate and the solvent Deionised Water (DI). The glass substrates used underwent a cleaning process:

1. 5 min sonication in DI and decon 90 ("an emulsion of anionic and non-ionic surface active agents, stabilising agents, non-phosphate detergent builders, alkalis and sequestering agents, in an aqueous base"[187]).
2. Wash with DI.
3. 5 min sonication in acetone.
4. Wash with DI.
5. 5 min sonication with Isopropyl Alcohol (IPA).
6. Dry with a nitrogen airgun.

The product from this experimental series was analysed using Raman spectroscopy, the results can be seen in Figures 5.3.6 to 5.3.8.

Further investigation into the pH comparing the Ca & F precursors in a DI solution with dropwise addition of the $NH_4F$ solution into the Ca solution was undertaken. A $0.1\,\mathrm{mol\,dm^{-3}}$ solution of Ca-lacate and $NH_4F$ in DI stirred for many hours had a pH of 6.0. However with the $NH_4F$ being added dropwise and left stirring yielded a pH of 5.6. As the ideal pH for $CaF_2$ production is between 5 & 6 [188], then dropwise addition of the F solution is the optimal method.

An experimental series involved fixed concentrations of $CaF_2$, varying concentrations of citrate with a delay before the addition of the citrate. The concentrations of citrate were 0.01, 0.1, 0.5, 1 & 5 %mol, the time delays chosen were, 0, 1, 2, & 3 h. The concentration of $CaF_2$ was $0.1\,\mathrm{mol\,dm^{-3}}$. As a development from the previous experiment, the $NH_4F$ solution was added dropwise into the Ca lactate solution whilst being stirred. The citrate solution was also added dropwise whilst being stirred, then left to stir for 2 hours before characterisation. After characterisation the samples were annealed at 600 °C for 90 min. The results from this particular series can be seen in Figures 5.3.11 to 5.3.14.

## Raman Characterisation

Raman is a technique used to characterise a sample by illuminating it with monochromatic optical light [189, 190]. The majority of the interactions will be elastic, i.e. no

energy loss, therefore the wavelength is constant. However some of those interactions are inelastic, there is an energy change and therefore a shift in the wavenumber. By investigating a sample through this technqiue many features about a material can be probed. One of the features is the presence of elements, but the bonds between them can also be understood. Figures Figs. 5.3.1 and 5.3.2 show the Raman spectra for $CaF_2$ and $CaF_2$:Eu respectively. The data reveals that pure $CaF_2$ has a single peak at $321\,cm^{-1}$, the presence of impurities adds peaks at $\sim 500\,cm^{-1}$ and $2000\,cm^{-1}$ to $2200\,cm^{-1}$. When the $CaF_2$ is doped with europium there remains a single peak, however it does shift down to a lower Raman Shift values, $\sim 318\,cm^{-1}$ (Fig. 5.3.2). One further effect of the europium doping is the broadening of the $\sim 318\,cm^{-1}$ peak. The data in Fig. 5.3.1 shows at peak a $\sim 470\,cm^{-1}$, this is quite likely due to small amounts of impurities [191, 192]. The peaks that are present at $\sim 2050\,cm^{-1}$ are not as readily identifiable as other data sets do not extend this far [193, 194].

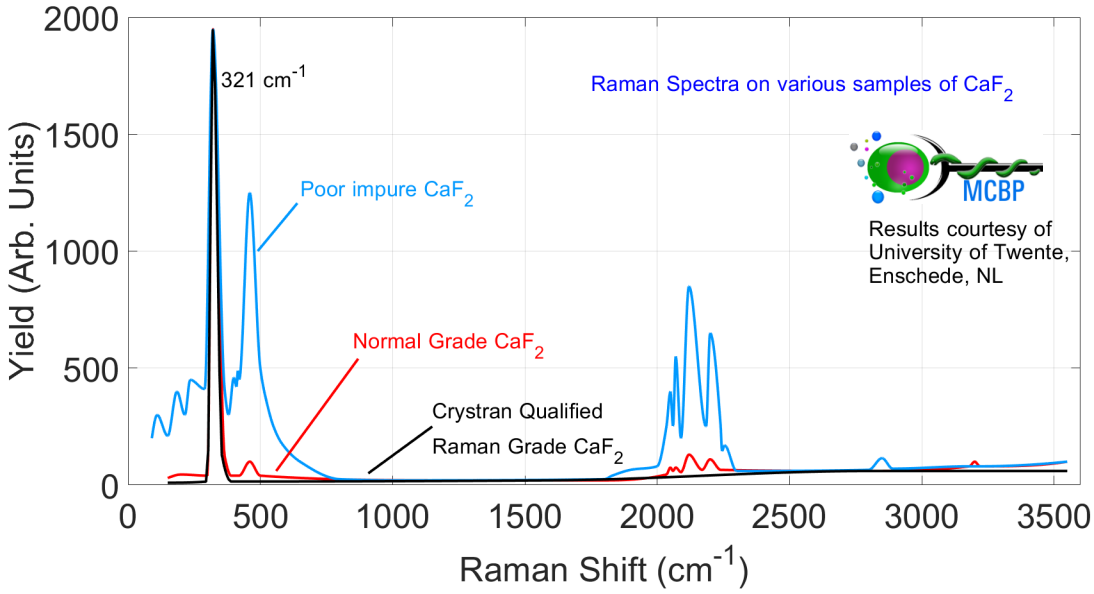


Figure 5.3.1: Raman spectra of pure and impure $CaF_2$, adapted from [195].

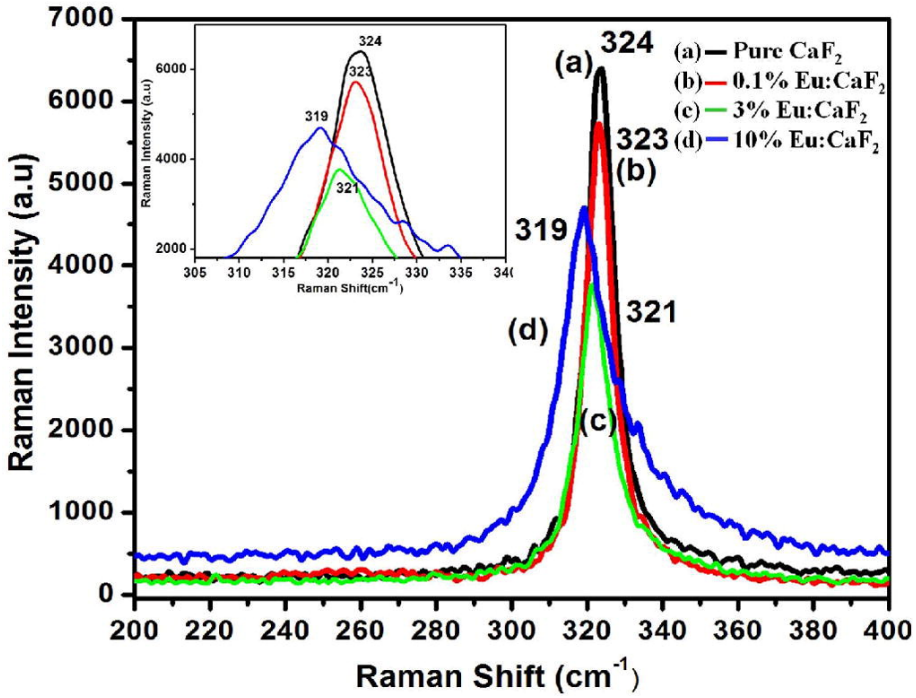


Figure 5.3.2: Raman spectra of pure $CaF_2$ and $CaF_2$:Eu at various doping concentrations [196, 197].

### 5.3.2 Results & Discussion

The data shown in Fig. 5.3.3 shows the Raman spectra from a single crystal of $CaF_2$:Eu purchased from Hellma. This acted as a reference for the Raman results, note that the characteristic $321\,cm^{-1}$ peak of $CaF_2$ has a low relative intensity and the numerous additional peaks. The two figures shown earlier showed that for $CaF_2$ & $CaF_2$:Eu there should only be the $321\,cm^{-1}$ peak. These additional peaks could be from surface contamination.

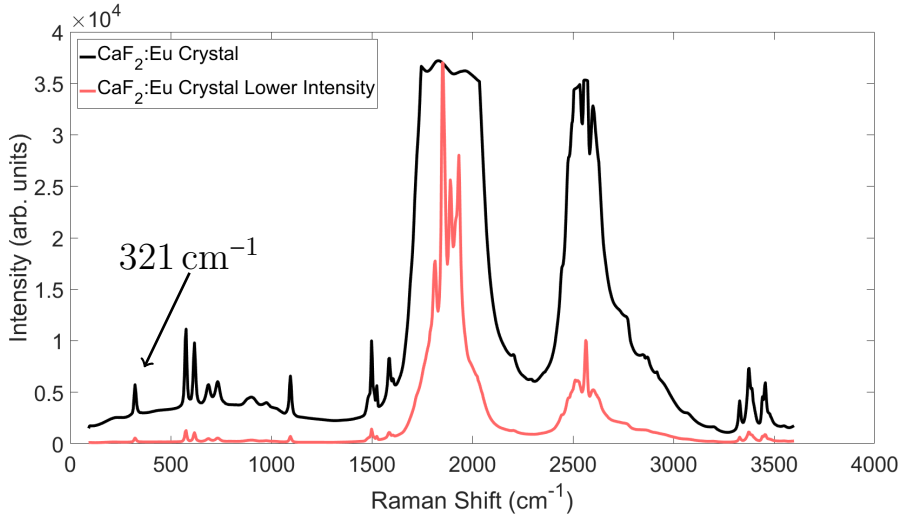


Figure 5.3.3: Measured raman spectra of a purchased [83] single crystal of $CaF_2$:Eu.

The experiment investigating the spray depositing of $CaF_2$:Eu onto a hotplate, with the resulting samples being annealed at 600 °C and 700 °C are shown in Figs. 5.3.4 and 5.3.5. The remainder of the figures are located in the Appendix, Figures A.4.1 to A.4.3. The expected $321\,cm^{-1}$ peak is present in some of the data. There are a number of other peaks in the data, particularly at $\sim 1900\,cm^{-1}$ and $\sim 2500\,cm^{-1}$, which are also of a much larger amplitude. It seems that $CaF_2$ has likely been formed,

but in small quantities and with significant impurities in the product. The Raman spectra of $CaF_2$:Eu [194] shows an additional peak at $\sim$1050 $cm^{-1}$, this is also in the presented data at 1095 $cm^{-1}$. This peaks has a low amplitude, like the $CaF_2$ peak, indictating that $CaF_2$:Eu has likely been produced but in small quantities.

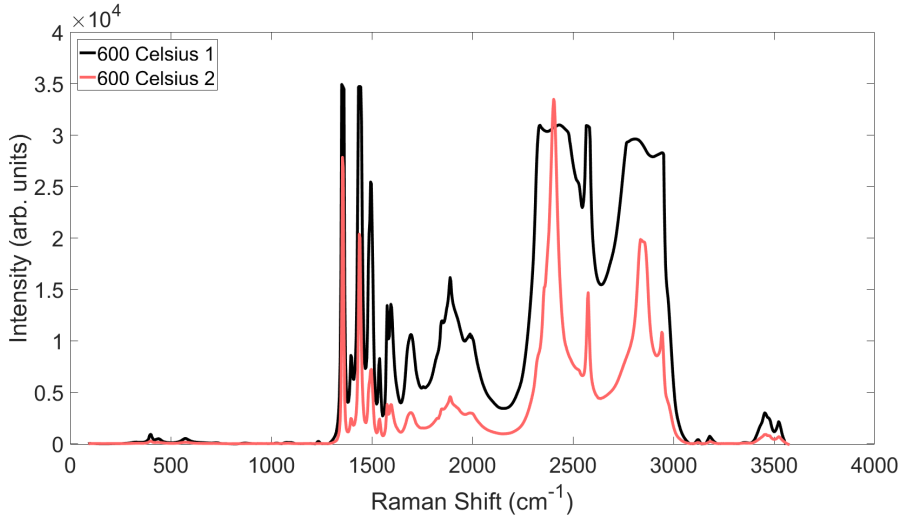


Figure 5.3.4: Raman results of the spray deposited $CaF_2$:Eu onto a 200 °C hot plate, which were annealed at 600 °C.

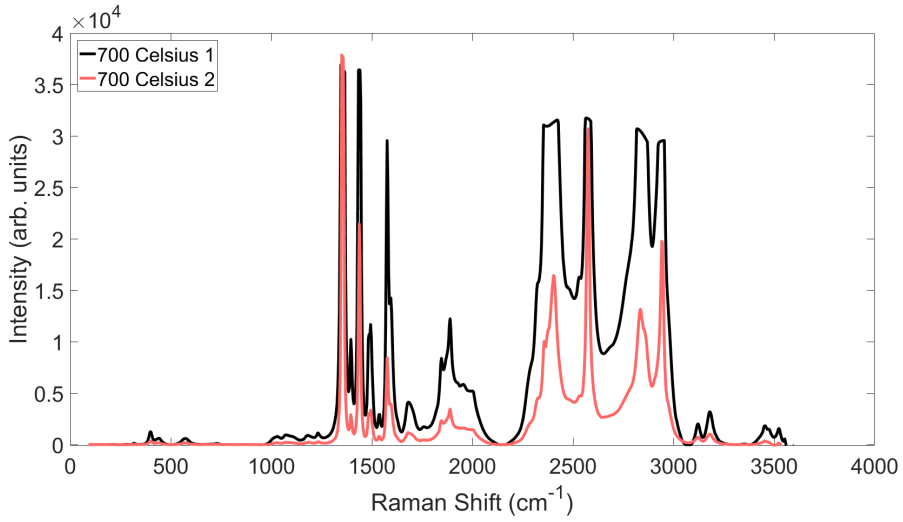


Figure 5.3.5: Raman results of the spray deposited $CaF_2$:Eu onto a 200 °C hot plate, which were annealed at 700 °C.

Shown in Fig. 5.3.6 is the resulting Raman for a hot plate temperature of 150 °C, the remainder of the data can be seen in Appendix A.4. The data across all of the deposition temperatures provides evidence that annealing is important. As can be observed the 321 $cm^{-1}$ peak has increased amplitude with many of the other peaks decreasing in amplitude. Figures 5.3.6 to 5.3.8 show the effects of temperature and anneal time and Figs. 5.3.9 and 5.3.10 shows the effect of annealing time. Fig. 5.3.6 shows all the Raman spectra for the 150 °C hot plate temperature, the spectra for the other temperatures are located in Appendix A.4. In the presented data (Fig. 5.3.6 and Appendix A.4) every curve shows the characteristic $CaF_2$ peak. When the data from Figures 5.3.7 to 5.3.10 is analyses it reveals that in order to maximise the 321 $cm^{-1}$ peak the hot plate temperature should be 400 °C and the sample should be annealed for 120 min. This suggests that these parameters are close to optimal for producing

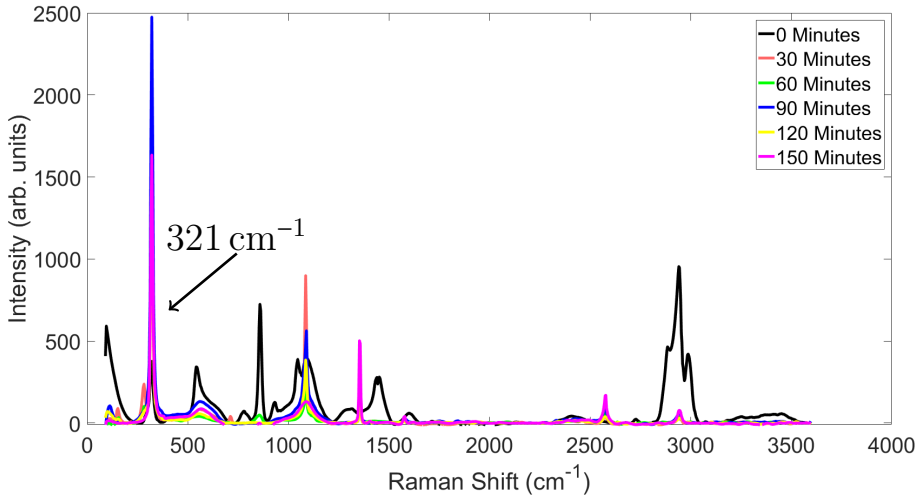


Figure 5.3.6: Raman spectra of the $CaF_2$ samples spray desposited at 150 °C and annealed at 700 °C with annealing times shown. The solution composition was $NH_4F$ and Calcium L-lactate pentahydrate with deionised water.

$CaF_2$ using these chemicals and hot plate deposition. A further observation can be made from the data, the annealing process decreased the amplitude on many of the other peaks. This suggests that the annealing process affected the structure of the material. It was noted that in Chapter 5.2.1 it is possible to reduce $Eu^{3+}$ to $Eu^{2+}$ through annealing, this reduction was not examined.

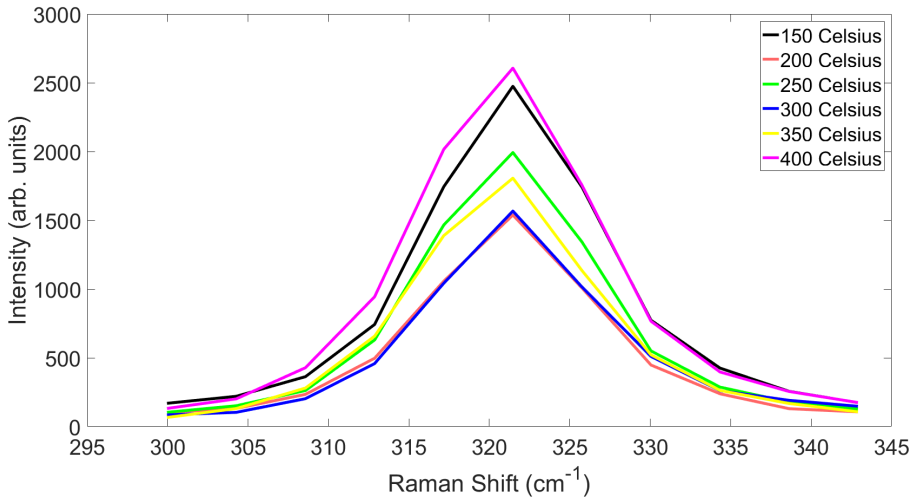


Figure 5.3.7: Amplitude of the 321 $cm^{-1}$ peak vs. hot plate temperature for the fabricated $CaF_2$. The data has been reduced to plot only the maximum peak amplitude for each hot plate temperature.

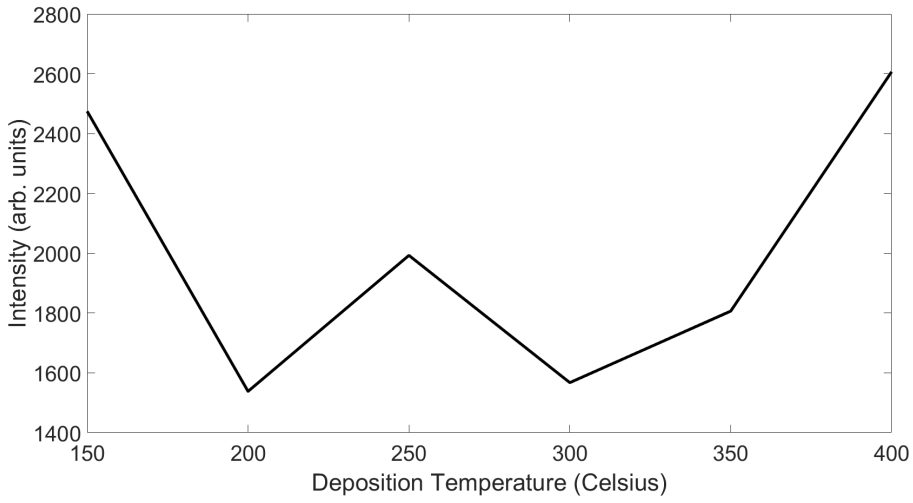


Figure 5.3.8: Data showing the maximum 321 $cm^{-1}$ peak for each spraying hot plate temperature for the $CaF_2$ Raman results.

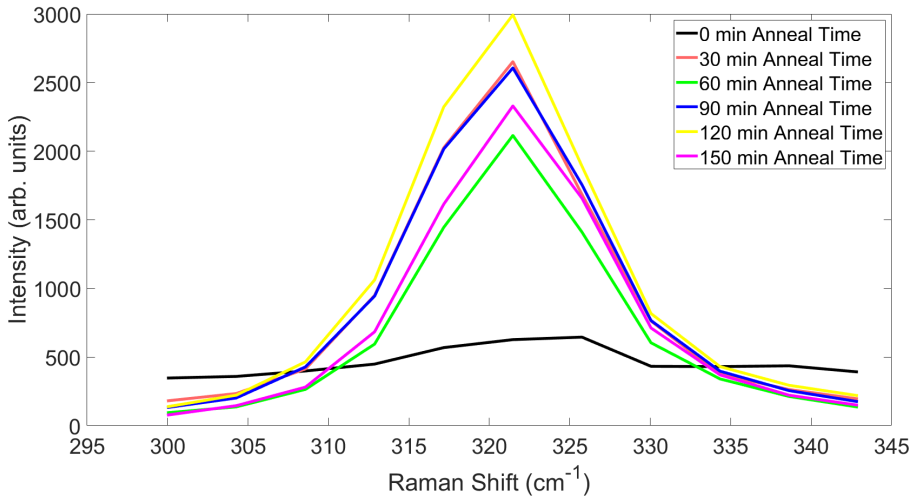


Figure 5.3.9: Amplitude of the 321 $cm^{-1}$ peak vs. anneal time for the fabricated $CaF_2$. The data has been reduced to plot only the maximum peak amplitude for each anneal time.

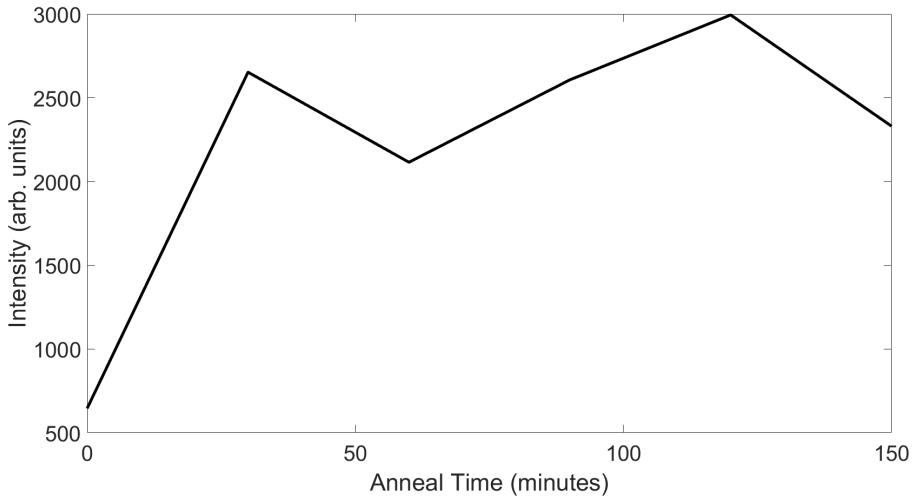


Figure 5.3.10: Data showing the maximum 321 $cm^{-1}$ peak for each total anneal time for the $CaF_2$ Raman results.

The results from the experimental series with the citrate did not produce any conclusive results. All the samples were analysed only using the optical microscope, a small selection of these images are included in Figures 5.3.11 to 5.3.14. Whilst there are some differences between the images, analysis of the size of the features did not determine a correlation between feature size and citrate concentration. As there was no noticeable correlation further analysis, i.e. the Raman spectra, was not measured.

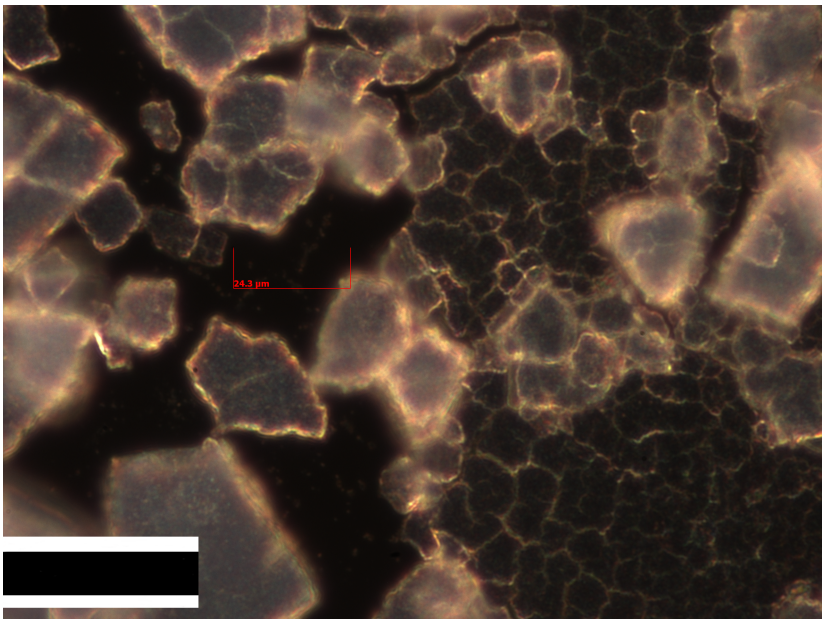


Figure 5.3.11: Optical micropscope image of 1 %mol citrate with no delay before its addition, the scale bar represents 50 µm.

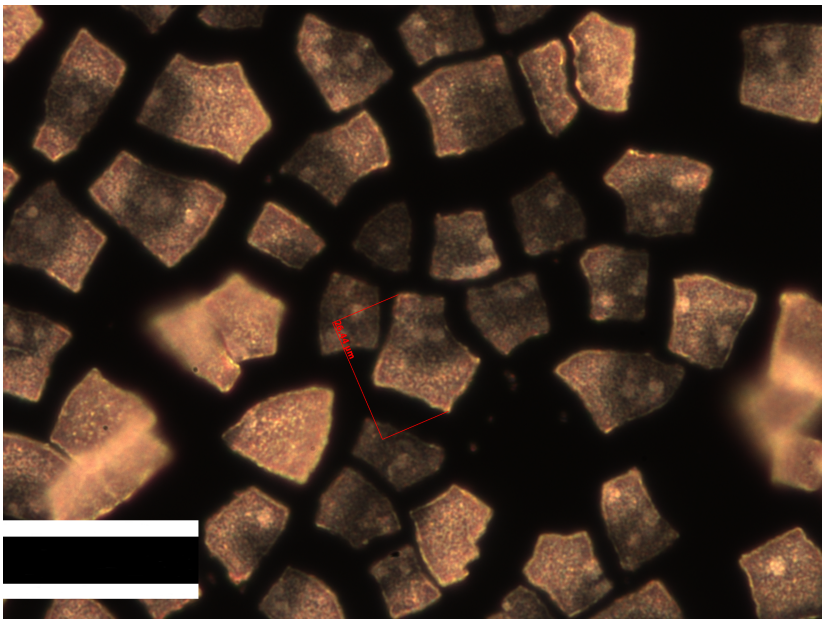

Figure 5.3.12: Optical microscope image of 1 %mol citrate with no delay before its addition. Then annealed at 600 °C for 90 min. The scale bar represents 50 µm.

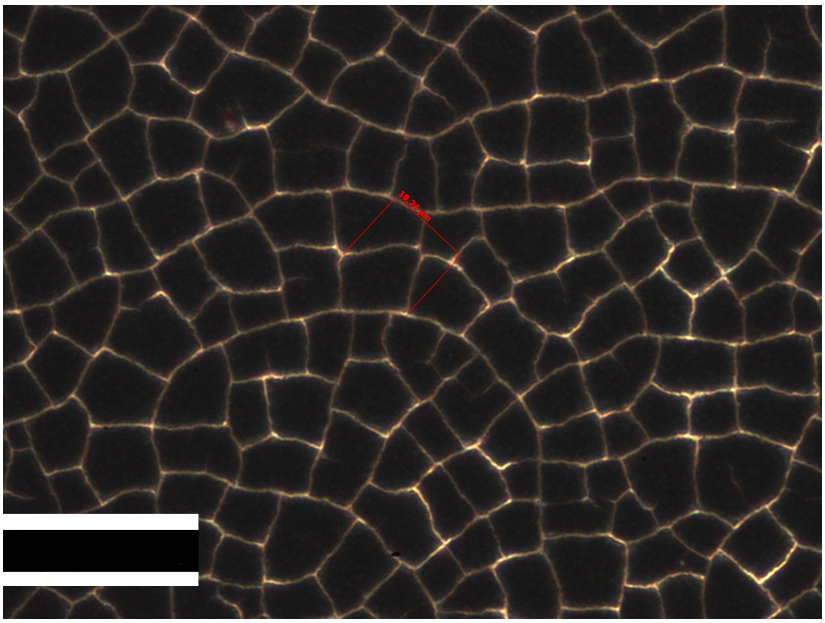

Figure 5.3.13: Optical micropscope image of 0.1 %mol citrate with a 1 h delay before its addition, the scale bar represents 50 µm.

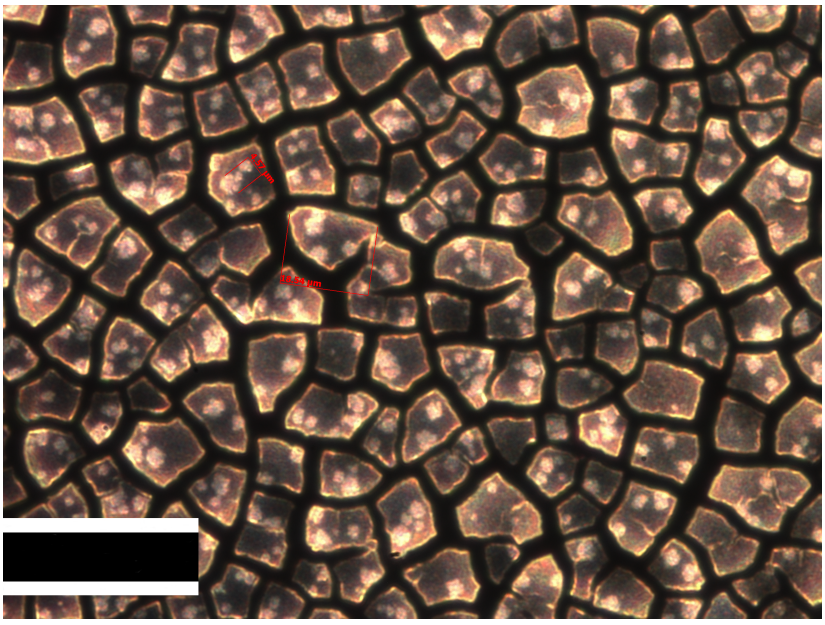

Figure 5.3.14: Optical micropscope image of 0.1 %mol citrate with a 1 h delay before its addition. Then annealed at 600 °C for 90 min. The scale bar represents 50 µm.

### 5.3.3 Conclusion

This section has demonstrated the likely formation of $CaF_2$ in Fig. 5.3.6, as the $321\,cm^{-1}$ peak is characteristic of $CaF_2$. However the results do not conclusively show the formation of $CaF_2$ particles.

## 5.4 Particle Fabrication Method: Granulation using Mortar & Pestle

This section covers the alternate method of granulation, focusing on the use of a mortar and pestle.

### 5.4.1 Method

This method involved crushing up a single crystal scintillator to produce the desired particles. The single crystals were purchased from Hellma [83] as a small disc (1.5 cm radius & ∼1.5 mm thickness), and with either a ground or polished surface finish. After crushing, the particle size distribution was determined using water dispersion and optical light, the particular instrument being a MasterSizer 3000 [198].

### 5.4.2 Results & Discussion

The results of the granulation process using a mortar & pestle are shown in Figs. 5.4.1 and 5.4.2. The results demonstrate that crushing down a single crystal with a mortar & pestle can produce small particles of $CaF_2$:Eu. The two figures represent the

particle size distribution from the crushing of two different (no known difference in composition) single crystals. The centre of the distribution in Fig. 5.4.1 is ∼7 µm with the particles sizes between ∼2 µm to 11 µm, and Fig. 5.4.2 has its centre at ∼10 µm and the diameters range between ∼2 µm to 50 µm. An optical microscope image of the crushed $CaF_2$:Eu is shown in Fig. 5.4.3, no shape analysis of the image has been undertaken, however it can be seen visually that the particles do not have a sphericity close to 1.

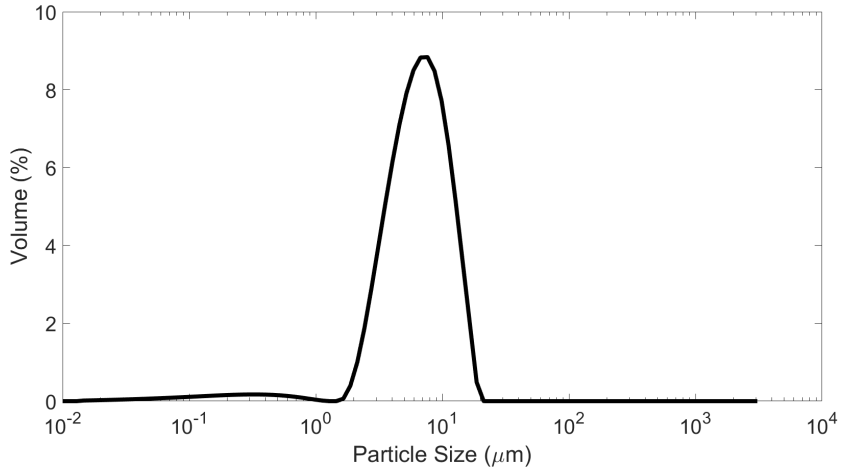


Figure 5.4.1: Results of the particle size distribution of the produced heterogeneous scintillator using a MasterSizer.

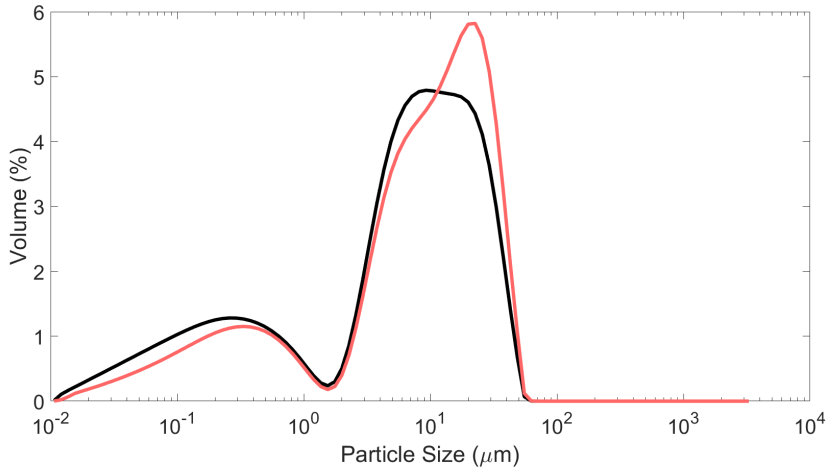


Figure 5.4.2: Results of the particle size distribution of the produced heterogeneous scintillator using a MasterSizer [198].

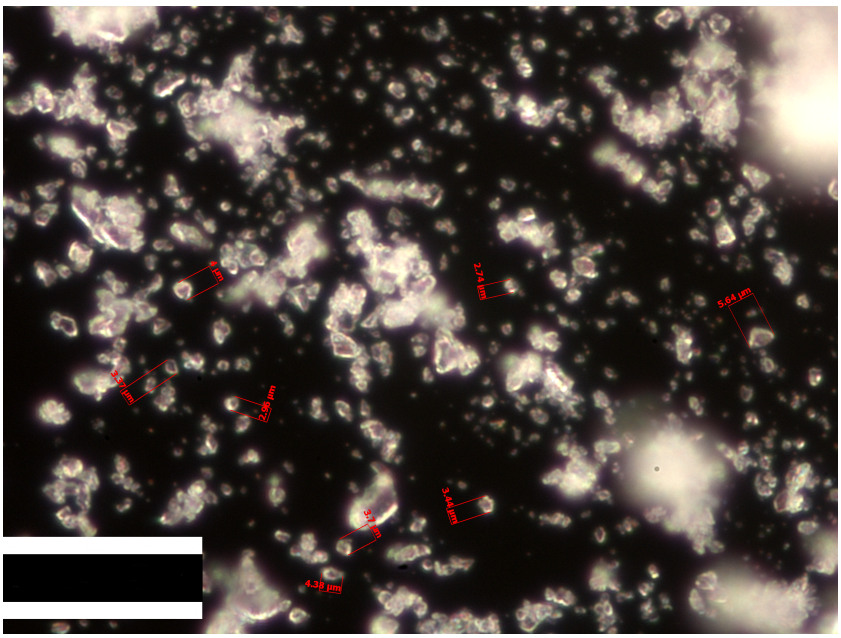

Figure 5.4.3: Optical brightfield microscope image of the $CaF_2$:Eu particle crushed using a mortar & pestle. The scale bar equates to 50 µm and the image was taken at 50x magnification.

## 5.5 Conclusion

The data from the chemical section does show the fabrication of $CaF_2$, in the hot plate experimental series. However the experiments with the citrate and with the europium did not show the successful formation of $CaF_2$:Eu particles. The mortar & pestle method did demonstrate the production of micrometre sized particles of $CaF_2$:Eu. Given the simplicity of this method and the positive results it is the chosen method for the required application.

# Chapter 6

# Heterogeneous Scintillator Detector

## 6.1 Introduction

Chapters 2 and 4 demonstrated that $CaF_2$:Eu can detect the beta particles from a tritium decay. Chapter 3 highlighted some of the inherent difficulties, such as the short range of the beta particle. It was further noted in Chapter 2 that heterogeneous scintillators offer important advantages. This chapter extends this work by presenting a novel approach, the scintillator for this was produced using the method in Chapter 5.4, the mortar & pestle.

This chapter details the design of a particular arrangement of heterogeneous scintillator through both simulations and experiments to show its benefits when compared with a single crystal. This arrangement is referred to as a planar $2D$ structure. Latter parts of this chapter will examine alternate configurations, namely multiple layers of $2D$ unit cells, $3D$ structures of unit cells and a flow-cell.

## 6.2 Definition of 2D Configuration in Geant4

Chapter 4.3 utilised the Monte Carlo simulation software Geant4 to model the beta particles, as will this chapter. Whilst it was previously used to better understand the inefficiencies in waterborne tritium detection, in this chapter it will be used to simulate the efficiency of the heterogeneous scintillator configuration. This model will be employed to guide the design of a flow-cell by optimising the particles arrangement and size. The modelling for the heterogeneous scintillator was completed using Geant4 versions 10.3 using the CentOS 7 VM [114] and a Ubuntu 16.04 LTS machine.

### 6.2.1 Beta Source

Three beta emitting radionuclides were used to create the heterogeneous scintillator model, namely $^{3}$H (<18.6 keV [15]), $^{14}$C (<156.476 keV [199]) and $^{210}$Pb (<63.5 keV [200]). $^{14}$C and $^{210}$Pb were chosen because they are both beta emitters, with a different energy spectrum and they are commonly used as tracers in the environmental sciences [201, 202, 203, 204, 205]. The energy spectrum data for each was extracted and extrapolated from the Radiological Toolbox [17], using the same method as discussed in Chapter 4. The energy spectra for the radionuclides are shown in Figs. 4.3.2, 6.2.1 & 6.2.2, the original data from the Radiological Toolbox is also plotted.

For the reasons stated in Chapter 4 G4GeneralParticleSource has been employed again. The source was defined as a cubic volume and isotropic. The dimensions were set using the sum of the individial water volumes, e.g. 1000 unit cells in a square

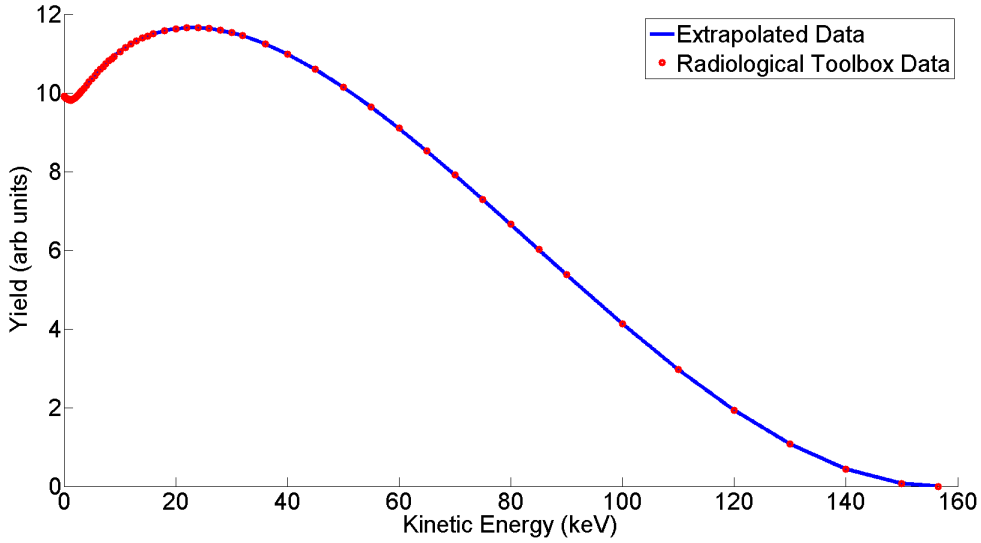


Figure 6.2.1: Energy spectrum data for $^{14}$C from the Radiological Toolbox [17], plotted with the extrapolated spectrum.

pack which equates to 2000R, the length of the source volume in the $\hat{x}$ & $\hat{y}$ axes. One cubic volume is then used to cover all the present unit cells, for this example it would be 2000R$\hat{x}$ & 2000R$\hat{y}$. This definition of the source will generate the beta particles at any location inside its volume, therefore when placed over the unit cells, the beta particles could be created inside one of the scintillator volumes. This is not representative of an experimental setup, so to avoid this, if a beta particle is created in one of the scintillator volumes it is immediately killed, along with any secondaries so that it effectively was never generated.

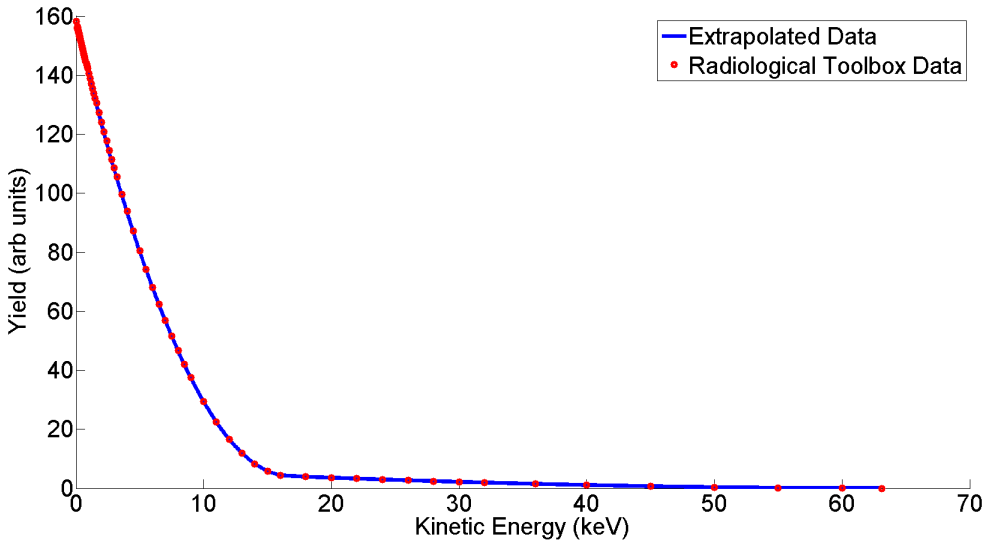


Figure 6.2.2: Energy spectrum data for $^{210}$Pb from the Radiological Toolbox [17], plotted with the extrapolated spectrum.

### 6.2.2 Geometry

As stated in the introduction to this chapter, there is a focus on a planar arrangement of scintillator particles, called here $2D$. The current detectors (Chapter 2) have either used a single crystal scintillator or a heterogeneous scintillator for this application. The choice of heterogeneous scintillators used in the literature so far offers an increase in the energy detection efficiency over equivalent single crystal configurations, but only at flow rates unsuitable for detecting rapid changes in transient tritium concentration levels. The novel method presented here using a single layer (2D) of scintillator particles provides a small increase in the deposited energy compared to single crystal configurations without a significant impact on the flow rate. The geometry used in this simulation was built up from unit cells, similar to those from crystallography. The unit cells chosen for use with the 2D arrangements here were Square Pack (SP) and Face

Centred Cubic (FCC), these were tiled together to form a large array of unit cells. The tiling of the unit cells was checked using the inbuilt visualisation code of Geant4. Close packed unit cells were selected as these arrangements would give the best possible results and be the most representative of an experimental heterogeneous scintillator produced using the techniques described in the previous chapter, given random arrays are very difficult to simulate. The sphericity of the $CaF_2$:Eu particles are not known so the model will assume perfect sphericity, this has been used previously [113, 110]. This assumption does lead to a limitation of these simulations as a sphericity of $<1$ has not been examined.

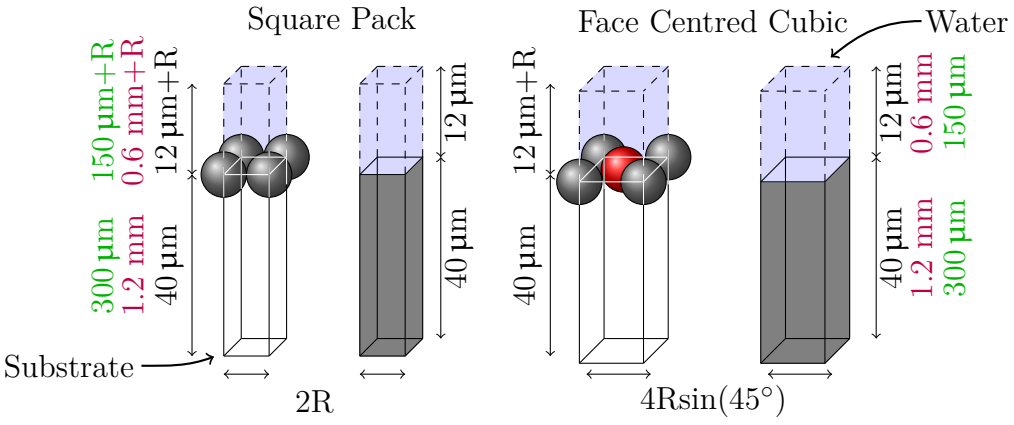


Figure 6.2.3: A diagram of the 2D geometries used in the heterogeneous Geant4 simulation, showing both Square Packed and Face Centred Cubic unit cells. Shown are both the single crystal and heterogeneous scintillator represented by both red and grey colours. Dimensions shown are for tritium (black text), Carbon 14 (purple text) and Lead 210 (green text). The inclusion of the additional radioisotopes Carbon 14 and Lead 210 is covered in Chapter 6.2.1.

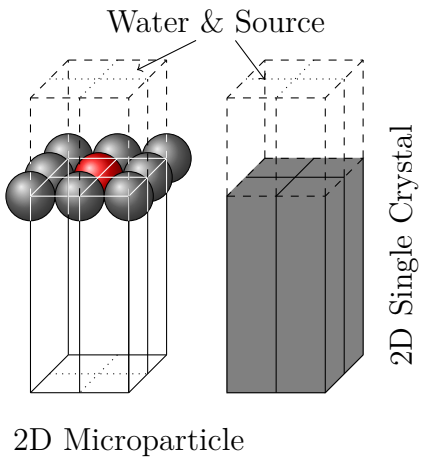


Figure 6.2.4: A diagram showing the tiling of the 2D Square Packed unit cells, red and grey colours denote scintillating material. For the 2D geometries the water & source as labelled and represented as the dashed volumes.

These 2D structures in the simulation were designed to represent a layer of scintillator particles on a substrate, a diagram of this can be seen in Fig. 6.2.3. The unit cells were defined using the following in the $\hat{x}$ & $\hat{y}$ axes:

- Square pack $\pm 2R$
- Face centred cubic $\pm 4Rsin(45deg)$

The height ($\hat{z}$) of the unit cells were set to be larger than the range of the particles and is given in the diagram. For comparison a single crystal of equivalent size was also modelled using the same method, this is also shown in Fig. 6.2.3. The figure contains diagramatic representations of the 2D square packed unit cells and single crystal unit cells employed along with the dimensions for each radioisotope. Red & grey is the scintillator material, white the substrate and blue the waterborne radioisotope. A diagram of these large tiled arrays can be seen in Fig. 6.2.4. An evolution of the 2D

idea involved a second inverted layer of particles and substrate. This would then represent a narrow planar channel lined with a layer of scintillator particles. A diagram given in Fig. 6.2.5 reveals the layout, the centre blue part is the source. Then the scintillator particles in red & grey and the substrate in white, this is then a pair of 2D structures. For this only the radioisotope tritium was employed, utilising the square packing and the sphere radius was fixed to 3.5 µm, as this is the optimal determined from the 2D data.

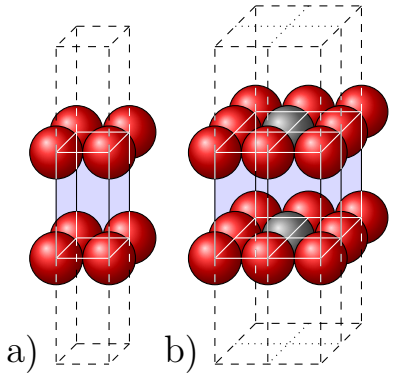


Figure 6.2.5: Diagram showing the structure of the layered 2D particulate scintillator. The source is in the blue part, scintillator spheres in red & grey and the substrate in white. a) and b) show a single unit cell and 2x2 array arrangement respectively.

A convergence study was conducted as to the ideal size of the array, for this the radioisotopes tritium and carbon 14 were employed. The structure was square packed and the radii were fixed to 3.5 µm and 150 µm for tritium and carbon 14, as these will maximise the energy deposited. The number of tiles in the simulation were varied to identify if an optimal exists, meaning, if more units cells are added beyond the

optimal there will not be an impact on the calculated energy deposited/initial energy ratio. The sizes of the arrays examined were $1^n$, $10^n$, $100^n$, $1000^n$ & $10{,}000^n$, where $n$ is the number of tiled dimensions. The data (Fig. 6.9.1) demonstrated that $1000^n$ was the optimal, all the simulations were then run with that size.

### 6.2.3 Data Analysis

The analysis code with Geant4 was broken down into several blocks:

1. Any particles escaping the unit cells and into the world gets removed from the simulation.

2. This simulation will investigate maximising the energy deposited from the radioisotope into the scintillator. As this simulation focuses on the energy deposition the scintillation photons do not need to be tracked. Therefore any optical photons created are killed after the first step, to prevent any interactions.

3. Extract the initial kinetic energy for each tritium beta particle and add to the running total of the tritium beta particles initial kinetic energy of beta particles generated. But not those that start inside a scintillator sphere.

4. Extract the energy deposited into the scintillator in each step from the tritium beta particles, and add to the running total of the deposited energy into the scintillator from the tritium beta particles.

Any simulation of a radiation detector system using a scintillator would have to simu-

late both the particle transport or interaction to the scintillator, and the scintillation photon transport to a photon detector (e.g. PMT). As is stated above, this simulation will focus on maximising the energy deposition into the scintillator. The reason for this focus is to generalise the results, as any inclusion of photon tracking would need to define the volumes that will reflect or absorb the photons. The errors associated with the quantities of Initial Kinetic Energy and Deposited Kinetic Energy were defined using a single pass variance, called Welford's Method [206, 207]. The implementation of Welford's method used is given below:

```
Number = 0;

OldMean = 0;

Mean = 0;

Var = 0;

for loop for each interaction{

     Number++;

     OldMean = Mean;

     Mean = Mean + (Value - Mean)/Number;

     Var = Var + (Value - Mean)*(Value - OldMean);

}

Variance = Var/(Number - 1);
```

The above method is used for a single quantity, *Value*, and calculates the associated variance. This form is employed once for the total initial energy and again for the total deposited energy to calculate the variance for each quantity.

### 6.2.4 Simulation Materials

The water was defined as above as hydrogen having an atomic number of 1 and molar mass of $1.01\,\mathrm{g\,mol^{-1}}$, and oxygen using an atomic number of 8 and molar mass of $16.00\,\mathrm{g\,mol^{-1}}$. With water itself being defined as $H_2O$ with density $1\,\mathrm{g\,cm^{-3}}$ [208]. Carbon and Silicon were defined using the NIST database, then used to create PDMS (Polydimethylsiloxane) as $C_2H_6OSi$ with density $0.97\,\mathrm{g\,cm^{-3}}$ [209].

The properties for $CaF_2$:Eu were defined as in Chapter 2. Using the NIST database the $CaF_2$ and Eu entries were combined, the Eu was doped at 2% and has a density of $5.243\,\mathrm{g\,cm^{-3}}$ [141]. The scintillating properties had the absoprtion length set to 1.0 m, the refractive index set to 1.47 [83] and the emission curve was approximated to 59 data points from literature [160] to provide sufficient accuracy (see Fig. 6.2.6) and the light yield set to $30\,000\,\mathrm{photons\,MeV^{-1}}$ [83]. The emission curve of the $CaF_2$:Eu scintillator is shown in Fig. 6.2.6. For PDMS the refractive index and attenuation length was set to 1.44 and 1 m respectively [209]. The scintillator thallium doped caesium iodide (CsI:Tl) was also simulated to compare with the $CaF_2$:Eu results with its properties also from Chapter 2. The above section describes that optical photons will not be tracked, for this reason the scintillation emission curve of CsI:Tl was simplified to only utilise 3 data points.

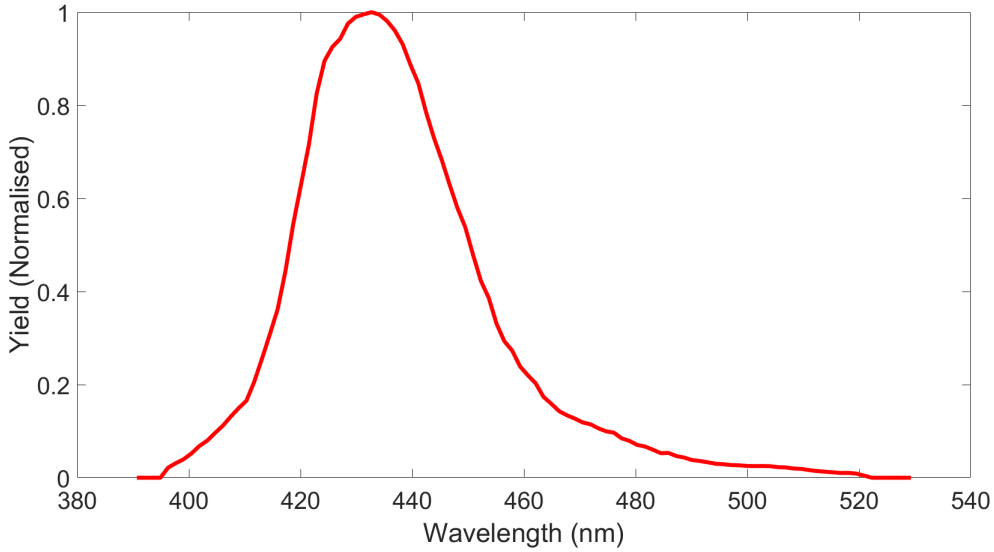


Figure 6.2.6: Approximation of the emission curve of $CaF_2$:Eu from reference data [160], produced using Geant4.

### 6.2.5 Physics Models Employed in Simulations

The physics models for e-/beta particles for the simulations in the this chapter are described below:

```
pmanager->AddProcess(new G4eMultipleScattering(),-1,1,1);
G4eIonisation* eIonisation = new G4eIonisation();
eIonisation->SetEmModel(new G4LivermoreIonisationModel());
pmanager->AddProcess(eIonisation,-1,2,2);
G4eBremsstrahlung* eBremsstrahlung = new G4eBremsstrahlung();
eBremsstrahlung->SetEmModel(new G4LivermoreBremsstrahlungModel());
pmanager->AddProcess(eBremsstrahlung,-1,-3,3);
```

For optical photons the models were, G4OpAbsorption, G4OpRayleigh, G4OpMieHG

& G4OpBoundaryProcess, for optical photon creation the models were G4Scintillation & G4Cherenkov. The electron/beta particle physics models were adjusted from the previous Chapter 4.3 with an aim towards increased accuracy. G4eIonisation was replaced with G4LivermoreIonisationModel and G4eBremsstrahlung was replaced with G4LivermoreBremsstrahlungModel, G4eMultipleScattering was unchanged. Chapter 3 explained that the Livermore models had increased accuracy when compared with the default models, including to lower energies. The physics simulation in Geant4 version 10.3 requires the use of a low energy cut-off for the beta transport, the default value for this is 1 keV. When a beta particles energy falls below the cut-off it will no longer be simulated. Fig. 6.2.7 shows a comparison of data with 1 keV and 100 eV cut offs. The $\hat{y}$ axis here is same ratio of total deposited energy against total initial energy as described in the above section. The cut-off here means that beneath this value the particle will no longer be tracked. This figure demonstrates that dropping the cut-off from 1 keV to 100 eV had no significant impact on the results.

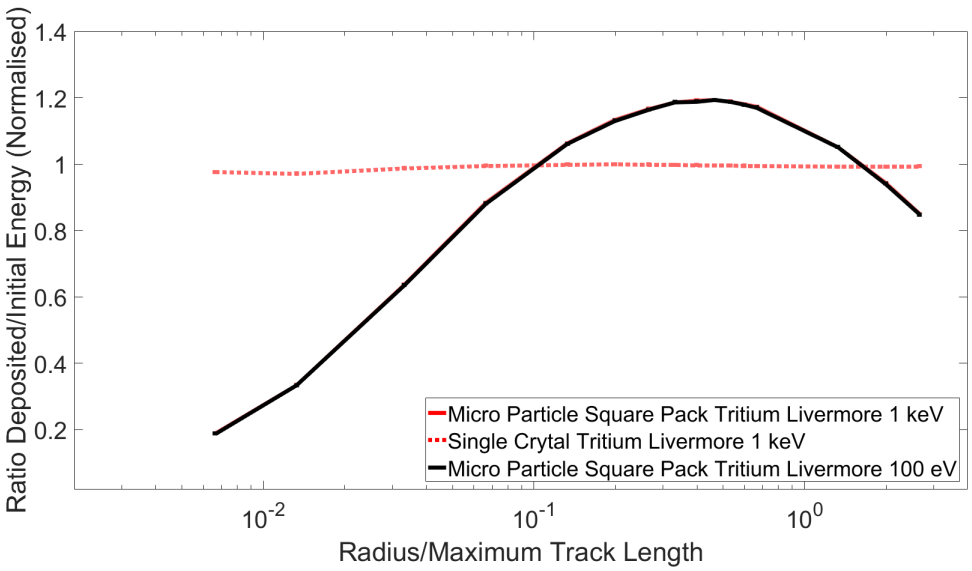


Figure 6.2.7: Comparison of simulation data showing the effect of reducing the minimum 'cut-off' kinetic energy, red curves and black curves denote the 1 keV and 100 eV energy cut off for the Livermore Models respectively. The solid black overlays the solid red line.

## 6.3 Geant4 Model Results Planar

The results for the 2D planar scintillator particle arrays data and all three radioisotopes is shown in Fig. 6.3.1. The $\hat{y}$ axis data for all the curves in the figure are normalised to the maximum value in the single crystal data for that particular isotope. It can be seen that the single crystal data for tritium, lead-210 and carbon-14 have a consistent efficiency. This is expected as the thickness is always adequate to absorb any particles and the increasing surface area is matched with a proportional increase in the surface area of the radiation source. The microparticle data curves all have a similar shape, and all have a single peak in the $\hat{y}$ axis to a value of $\sim$1.2, an approximate 20% increase. Those curves are shifted in the $\hat{x}$ axis due to the higher

energies of the beta particles. The radii of the scintillating at which each radioisotope has a maximum for the deposited energy in the microparticle unit cells are 3.5 µm, 30 µm and 150 µm for tritium, lead 210 and carbon 14 respectively. This specific result for tritium will be utilised in the next two sections in an experimental waterborne tritium detector.

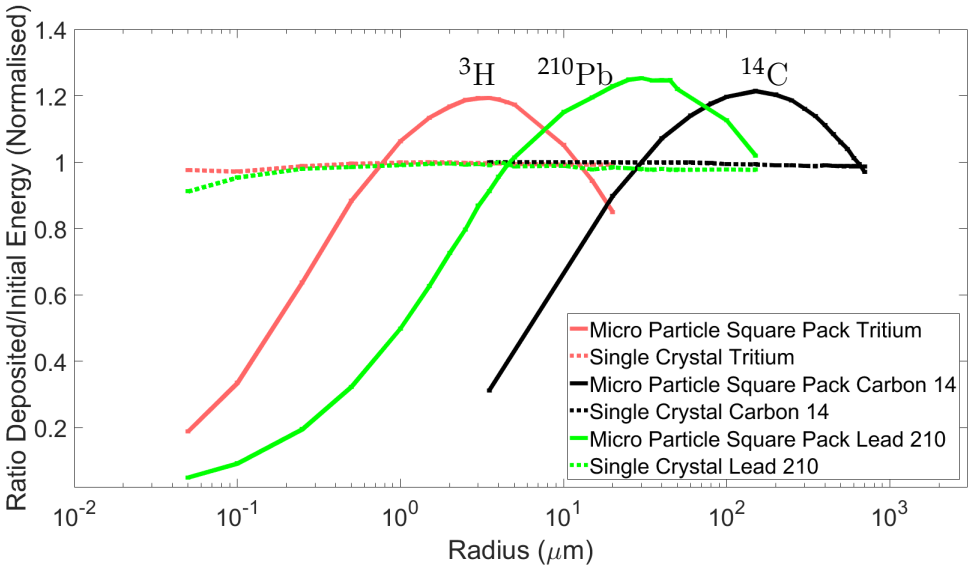


Figure 6.3.1: Results of the 2D Geant4 single crystal and heterogeneous scintillator simulations showing the radionuclides $^{3}$H, $^{14}$C & $^{210}$Pb. Face centred data is not plotted as it overlaps with the Square Pack data and the error bars are plotted but are of small magnitude.

## 6.4 Heterogeneous Planar Scintillator Fabrication

The simulation results as shown in the previous chapter were validated using an experimental setup. This chapter and the next detail the setup, followed by the results.

The scintillator was produced using single crystals ($CaF_2$:Eu) from Hellma [83]. These were crushed down using a mortar & pestle with particle size verified by dispersing in de-ionised water (using a MasterSizer 3000 instrument). The particle size distribution (most likely diameter at 7 µm diameter) can be seen in Fig. 5.4.1. PDMS was used as the substrate as it is optically transparent, has a similar refractive index to water and $CaF_2$:Eu and easy to cast to shape. A preliminary experiment was conducted to investigate the ease of depositing a powder onto the surface of PDMS. For this experiment a powder formed of crushed soda-lime glass was chosen as it is cheaper than $CaF_2$:Eu, this was crushed through the same method and its size and associated distribution verified using the same methodology. The size distribution of the soda-lime glass used in this preliminary experiment can be seen in Fig. 6.4.1, the most likely diameter is ∼30 µm. Time curing of the PDMS, using a 10:1 (base:curing agent) concluded that ∼22 h is ideal. A further preliminary experiment into the powder deposition method using a thin grating yielded a successful thin layer. Fig. 6.4.2 shows the cross section of crushed soda-lime glass powder deposited onto the PDMS substrate, it can be seen that the result is a single thin (∼80 µm) layer of glass particles. The method of using a thin grating is then suitable for depositing the heterogeneous scintillator onto PDMS.

The above method of fabricating the scintillating particles will be used to produce a scintillator for an experimental detector. The heterogeneous scintillator particles were deposited onto a substrate of PDMS [210], this was mixed to 10:1 base:curing agent.

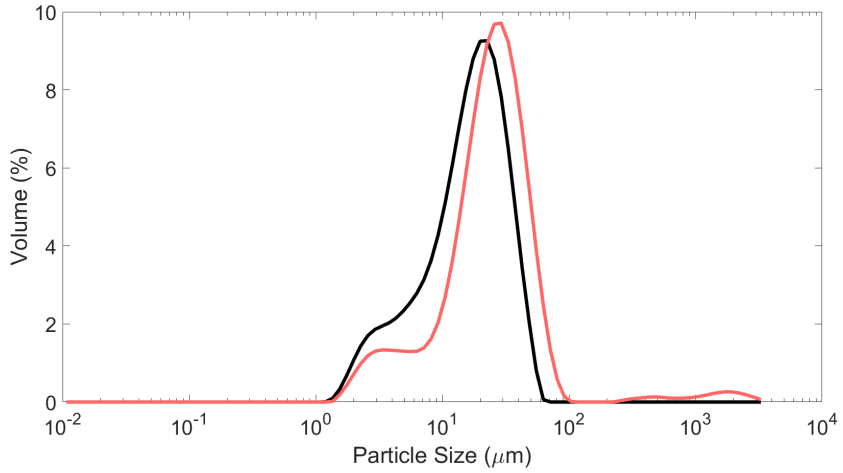


Figure 6.4.1: Results of two repeat measurements of the particle size distribution of soda-lime glass crushed using a mortar and pestle.

The deposition process itself involved partially curing the PDMS to 22 hours at room temperature under ambient conditions before the particle powder is deposited onto the top surface. This is then left to fully cure >48 hours. The particle size distribution of the soda lime particles adhered to the PDMS surface is shown in Fig. 5.4.1. An optical microscope image is included in Fig. 6.4.3.

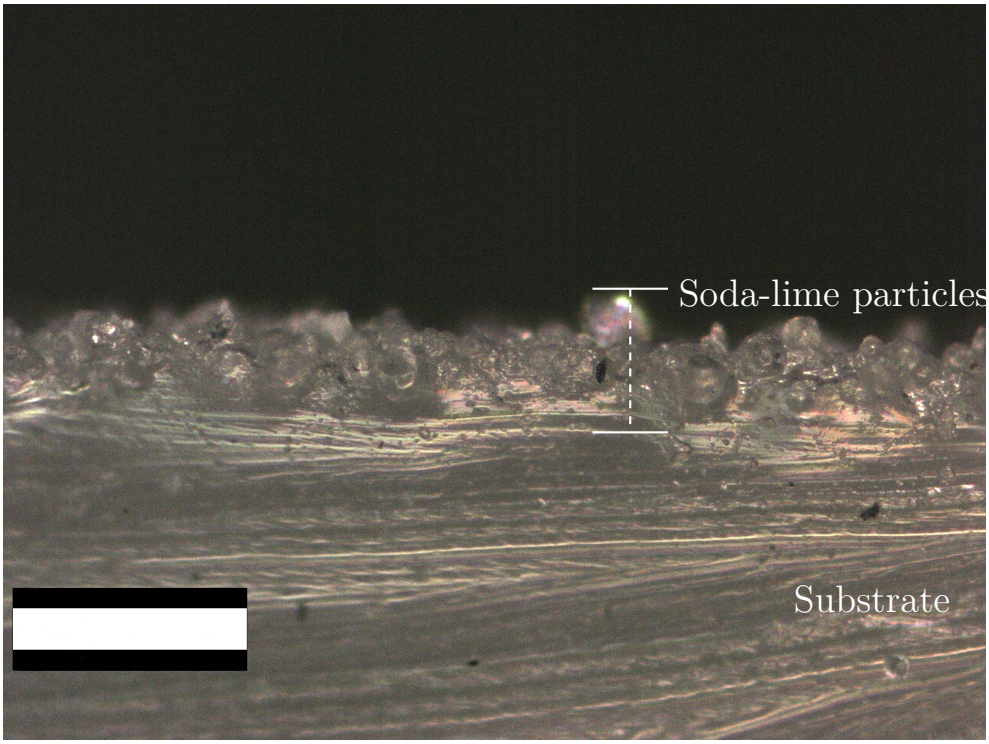


Figure 6.4.2: Optical microscope image of the cross section of the crushed soda-lime glass (Fig. 6.4.1) deposited onto the PDMS substrate. Image taken at 10x magnification and the scale bar equates to 200 µm.

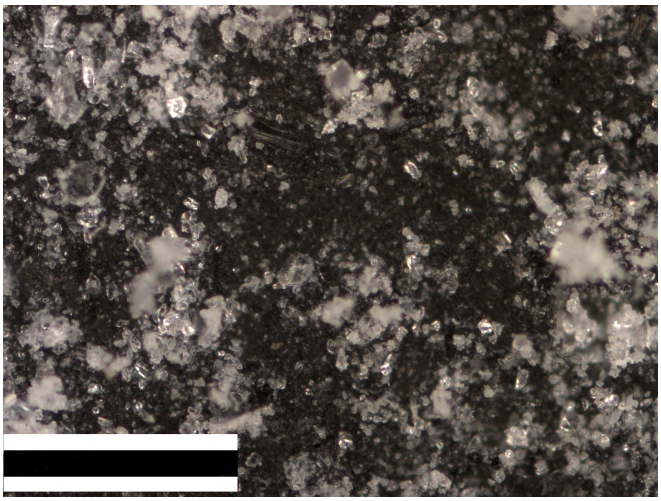

Figure 6.4.3: "Optical microscope bright field image of the surface of the particulate heterogeneous scintillator taken at 10x magnification. The scintillator chosen is $CaF_2$:Eu with PDMS as the substrate. The scale bar in the corner equates to 300 µm in length" [211].

The simulation results in Chapter 6.3 revealed that a layer of 3.5 µm radii $CaF_2$:Eu particles lead to more energy deposition than a comparable single crystal, Chapter 5.4 demonstrated that these particles could be produced through granulation with a mortar and pestle. If a single crystal had a radius of 5 mm it would have a projected surface area of 0.79 $cm^2$, however if the same crystal was granulated to form a single layer of particles the projected surface area would increase. To determine this increase the assumptions of the single crystal will be, a radius of 5 mm and a thickness of 2 mm. It will also be assumed that the particles produced all have a radius of 3.5 µm, are in a Square Packing formation, with a single layer and an equal number of units cells in each of its two axes ($\hat{x}$ & $\hat{y}$).

The equations used are listed in Eq. (6.4.1), (6.4.2), (6.4.3) & (6.4.4), with the terms,

$r$, the radius of the single crystal, $h$ the height and $R$ the radius of the granulated scintillator particle. The results are shown in Table 6.4.1, along with data for carbon 14 and lead 210 with their associated radii of 150 µm and 30 µm respectively. Whilst this is a idealised analysis the results show that the projected surface area does increase. This provides a further advantage, for a single crystal of a given volume it could be granulated for a larger surface area, leading to an increased detectable volume.

$$Single \quad Crystal \quad Volume = \pi r^2 h \tag{6.4.1}$$

$$Unit \quad Cell \quad Volume = \frac{4}{3}\pi R^3 \tag{6.4.2}$$

$$Number \quad Of \quad Unit \quad Cells = \frac{Eq.\ (6.4.1)}{Eq.\ (6.4.2)} \tag{6.4.3}$$

$$Length = \sqrt[2]{Eq.\ (6.4.3)} \cdot 2R \tag{6.4.4}$$

Table 6.4.1: Calculated results of a simple numerical prediction of the increase in surface area due to crushing a single crystal down to small uniform radius particles.

| Isotope | Particle Radius (µm) | Projected Surface Area ($cm^2$) |
|---|---|---|
| Tritium ($^3$H) | 3.5 | 428.49 |
| Carbon 14 ($^{14}$C) | 150 | 9.99 |
| Lead 210 ($^{210}$Pb) | 30 | 49.98 |

## 6.5 Experimental Detector Method & Results

### 6.5.1 Method

The experimental detector used the heterogeneous scintillator as described above (Chapter 6.4), the electronics in the detector were redesigned from those in Chapter 4. The redesigned circuit still employed a single Sensl C-Series 60035 SiPM, however the remainder of the circuit used surface mount components. The virtual ground circuit was improved (Fig. 6.5.1) and the TIA/CSP circuit (Fig. 6.5.2) now featuring a higher quality Op-Amp, LT6200-10, which has a lower noise voltage and bandwidth. The gain of the preamplifier was calculated using an LT Spice (version XVII) [212] simulation, Fig. 6.5.2. The input pulse was a single pulse of 1 mV & 0.5 µs square wave. The gain calculated from the output pulse is -3300.1. The feedback resistor and capacitor values are 600 kΩ & 33 pF respectively, this equates to a time constant of 19.8 µs. The ADC and light-proof box were identical to that from the earlier chapter. The radioisotope used was tritium with a concentration of 1500 $\mathrm{Bq\,mL^{-1}}$, this source of tritium was compared with a background sample of de-ionised water. The data produced from the detector was analysed using the peak detection code which used the Labview code [213] and operates through a threshold. When a data point passes a threshold and where the number of points in the peak exceed the user specified value the code will extract the value of the peak.

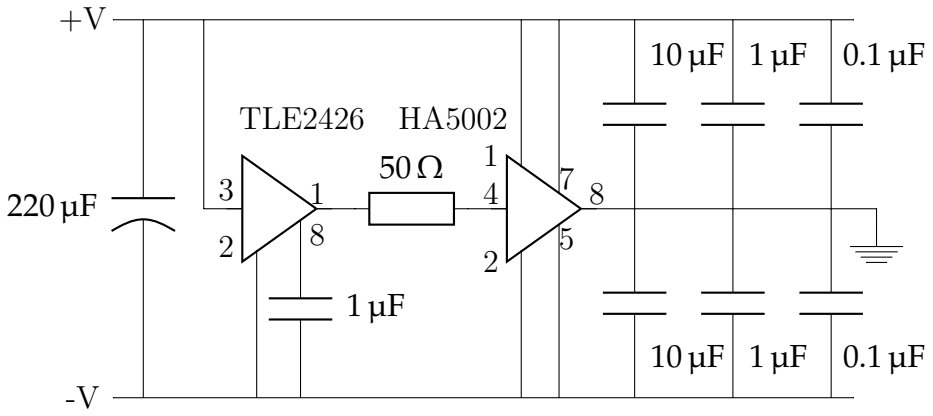


Figure 6.5.1: Circuit to power the pulse shaping part of the circuit using a TLE2426 and a HA5002 IC [214, 215].

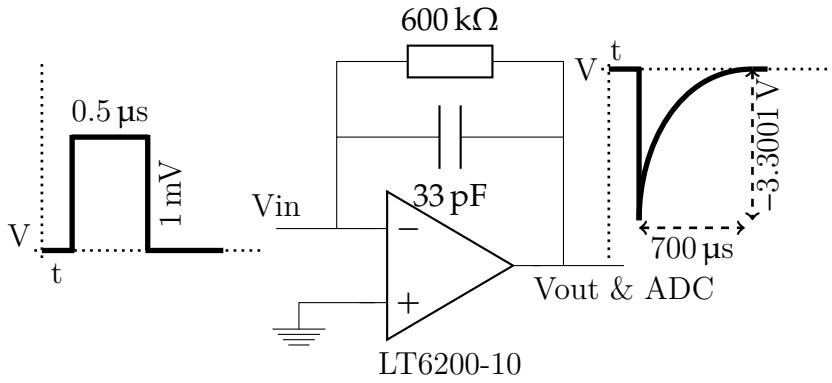


Figure 6.5.2: A circuit diagram of the updated Transimpedance preamplifier, using the LT6200-10 OpAmp [216]. This circuit was also employed in a simulation [212]. For this simulation the representations of the input and output pulses are shown.

### 6.5.2 Results & Discussion

The results from the heterogeneous scintillator and single crystal scintillator are shown in Table 6.5.1. The results reveal that there was an approximate ∼15% increase in the total counts when comparing the heterogeneous scintillator to the single crystal with the same projected surface area (actual surface area higher for the heterogeneous scintillator). The prediction from the Geant4 model highlighted that ∼20% more energy should be deposited in the scintillator when arranged as a layer of small particles. This result from experiment data is evidence for the accuracy of the Geant4 2D results.

Table 6.5.1: The results of the experimental setup of the single crystal scintillator and a comparable heterogeneous scintillator. Shown is the total counts i.e. those from tritium minus those from background. The prediction is taken to be a 20% increase of the single crystal with associated error [211].

| Counting Time | 600 s | 1200 s |
|---|---|---|
| Single Crystal Scintillator Total Counts | $151\,393 \pm 406$ | $293\,481 \pm 568$ |
| Prediction using the Single Crystal Scintillator | $181\,670 \pm 487$ | $352\,180 \pm 681$ |
| 2D Heterogeneous Scintillator Total Counts | $173\,421 \pm 228$ | $339\,450 \pm 305$ |

## 6.6 Normalisation of Geant4 Results

The results for the non-normalised Geant4 2D data has been shown previously in Fig. 6.3.1, a further method of analysing the data was used. The single crystal data in Fig. 6.3.1 maintains the same energy deposition despite the increasing projected surface area, the heterogeneous scintillator curves have the same overall shape, but at a different position on the $\hat{x}$ axis. The aim of the normalisation was to find a method of aligning the heterogeneous scintillator curves, the method was identical for the 2D SP, FCC & BCC unit cells, as well as the three radioisotopes. It specifically explored the normalisation through the maximum range of the beta particles in the medium. Two scenarios were considered, the true distance the particle travelled and the straight line distance the particle travelled, statistical expressions such as maximum, mean, geometric mean etc. were then applied. This range data has been produced using a simple simulation, a diagram is included in Fig. 6.6.1.

This simulation used a cube of $2\,\mathrm{m}^3$ of the medium, here water, with the beta particle source as a beam located at the centre. This beam in the $\hat{x}$ direction fired a total of $1\text{x}10^9$ particles, the remainder of the simulation such as physics models and material definitions were identical to those in Chapter 6.2. Two terms will be defined, the first is the Maximum Track Lengh. This is where the particles steps (i.e. the distance associated with each interaction) have been summed, then the maximum from all of these can be found. The other term is the Maximum Geometric Track Length which is the sum of the steps in the direction of the beam, likewise the maximum from all the particles can be found. Table 6.6.1 contains the two normalisation values as

mentioned, along with the additional values that were unsuccessful.

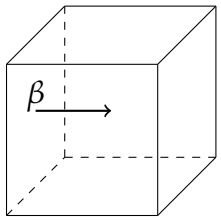


Figure 6.6.1: Simple diagram of beta particle range simulation using Geant4. The geometry was $2\,\mathrm{m}^3$ using water, the arrow denotes the beam of particles.

Table 6.6.1: Normalisation values used for the Geant4 heterogeneous scintillator data.

| Variable | Tritium ($^{3}$H) (µm) | Carbon 14 ($^{14}$C) (µm) | Lead 210 ($^{210}$Pb) (µm) |
|---|---|---|---|
| Max Track Length | 7.5405 | 340.004 | 63.5444 |
| Mean Track Length | 1.1992 | 53.2159 | 1.9190 |
| Geometric Mean Track Length | 0.5542 | 23.1442 | 0.4158 |
| Harmonic Mean Track Length | 0.0998 | 0.8567 | 0.0606 |
| Median Track Length | 0.7644 | 35.1438 | 0.5061 |
| Max Geometric Track Length | 4.0885 | 201.7240 | 36.5528 |
| Mean Geometric Track Length | 0.6104 | 27.9500 | 0.9887 |
| Geometric Mean Geometric Track Length | 0.2717 | 12.0033 | 0.1994 |
| Harmonic Mean Geometric Track Length | 0.0162 | 0.1388 | 0.0089 |
| Median Geometric Track Length | 0.3858 | 18.3627 | 0.2539 |

## 6.7 Geant4 Model Results 2D Normalised

The results for the non-normalised Geant4 2D data has been shown previously in Fig. 6.3.1 and Table 6.6.1 contains the data that was used for normalising. The aim of the normalisation was to align all the heterogeneous scintillator curves and the results are shown in Figs. 6.7.1 and 6.7.2 and Appendix A.5.1. The various figures show that only two of the variables worked, maximum track length and maximum geometric track length. All the of the normalisation variables are able to align the tritium and carbon 14 data, but only the aformentioned two can align all three curves. With the data now normalised and aligned, the peak in the heterogeneous data is located at $0.46\hat{x}$ and $0.81\hat{x}$, for maximum track length and maximum geometric track length respectively.

The initial energy spectra of the three radioisotopes have a different shape, with the lead 210 spectra being particularly different. The above method of normalisation is able to align the curves from the three radioisotopes, this could be applied to other beta emitters. If either of the two variables (maximum track length or maximum geometric track length) are known for a different $\beta^-$ emitting radioisotope, then the ideal radius can be predicted. With this prediction a 2D heterogeneous scintillator detector can be optimised for any waterborne $\beta^-$ emitting radioisotope.

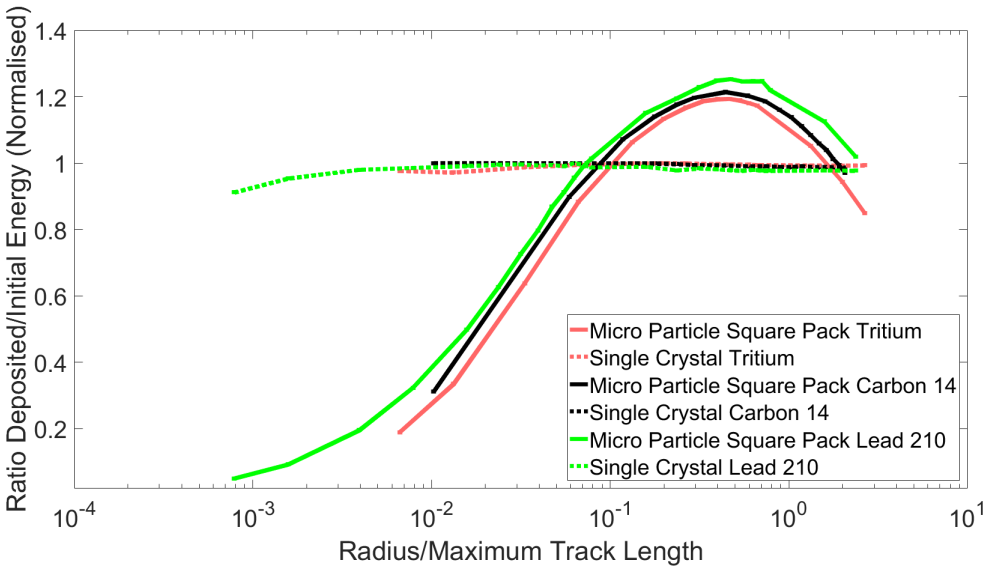


Figure 6.7.1: The results of the Geant4 2D single crystal and heterogeneous scintillator simulations using the $^{3}$H, $^{14}$C & $^{210}$Pb. These results are normalised using the Maximum Track Length values.

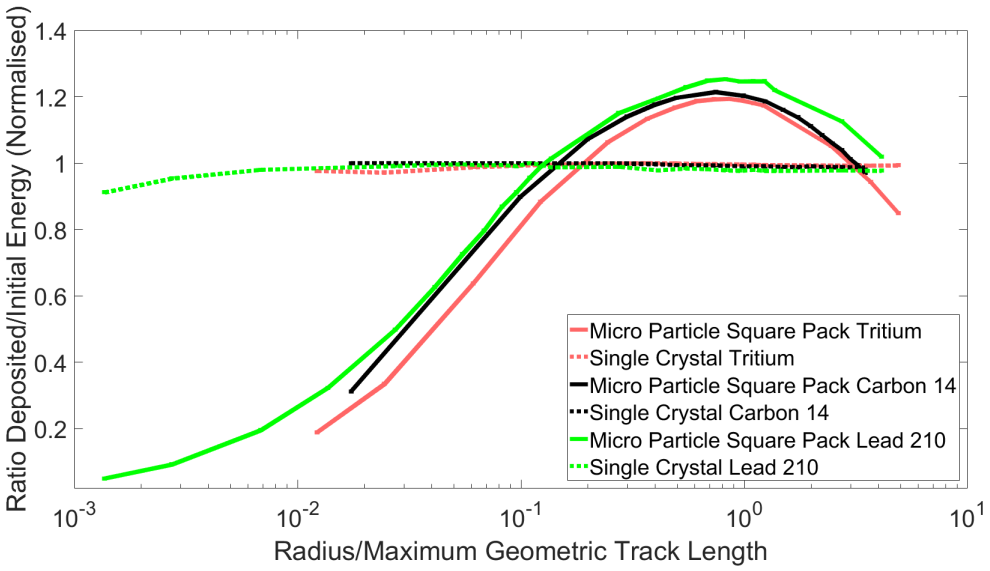


Figure 6.7.2: The results of the Geant4 2D single crystal and heterogeneous scintillator simulations using the $^{3}$H, $^{14}$C & $^{210}$Pb. These results are normalised using the Maximum Geometric Track Length values.

The results of the 2D multiple layers are located in Fig. 6.7.3. It can be seen that as the gap between the layers decreases the fraction of the total initial kinetic energy that gets deposited into the scintillator increases. This could then form the foundation of an experimental flow cell. A further figure has been included (Fig. 6.7.4) which demonstrates that the FCC data and SP data overlay one another. This data only displays the results for tritium.

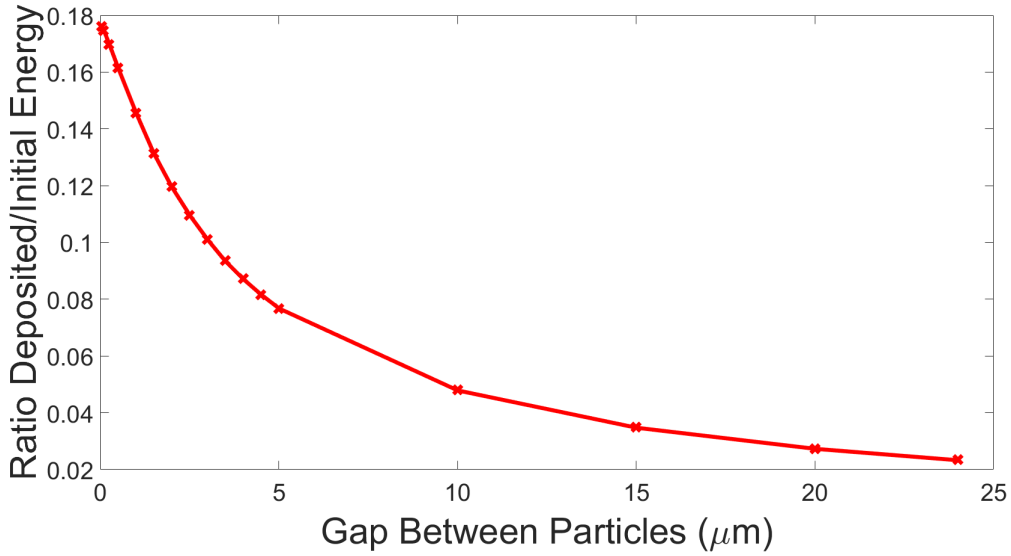


Figure 6.7.3: Geant4 simulation results of the dual layer of 2D $1000^2$ SP heterogeneous scintillator with tritium.

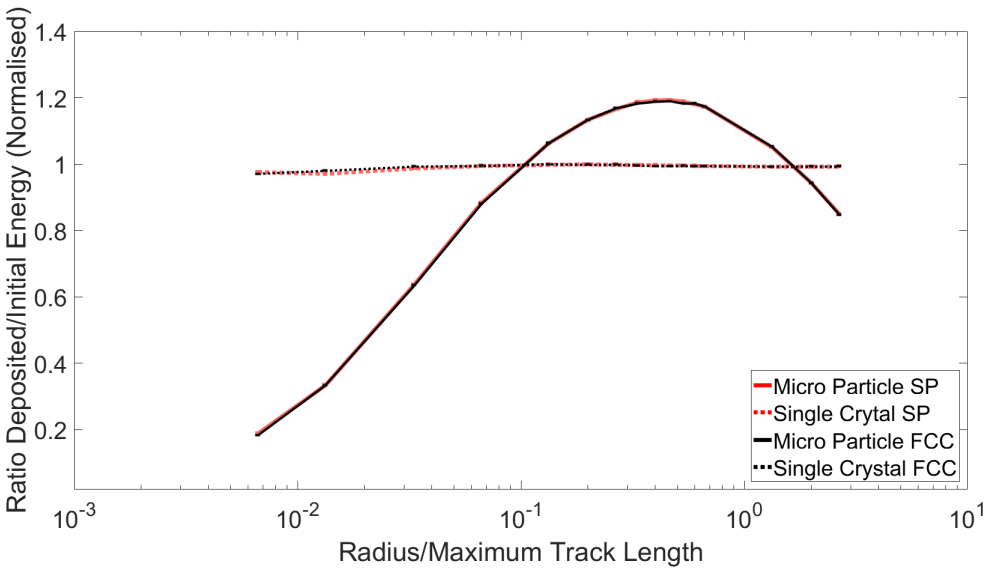


Figure 6.7.4: Geant4 Data showing the results of all the 2D structures, SP & FCC. The SP and FCC curves overlay one another.

## 6.8 Geant4 Model Definition 3D Packed Particle Configuration

This chapter has so far focused on 2D unit cells, that is where the particles are located in two spacial dimensions, and compared to planar single crystals. The focus now shifts to $3D$ unit cells, where the microparticles are positioned in three spacial dimensions. Aside from the change in geometry, the remainder of the simulation is the same, e.g. physics, materials definitions and data analysis code. These results will also be analysed using the same normalisation method as the 2D results.

### 6.8.1 Geometry

The 3D arrangements are built up from unit cells, in the same method as the 2D planar configurations. Here the packing structures chosen were Square Pack (SP), Face Centred Cubic (FCC) and Body Centred Cubic (BCC). The model for the 3D arrangements was designed to recreate a packed volume, i.e. a packed tube. For this reason, the material representing the volume between the spheres in the unit cell was defined to be water. These were again tiled up into larger arrays, see Figs. 6.8.1 and 6.8.2. The size of those unit cells in the $\hat{x}$, $\hat{y}$ & $\hat{z}$ axes was as follows:

- Square pack $\pm 2R$
- Face centred cubic $\pm 4Rsin(45deg)$
- Body centred cubic $\pm \frac{4R}{\sqrt{3}}$

As before the convergence study revealed that 1000 unit cells in each axis was sufficient to be considered infinite in extent, the data of this can be seen in Fig. 6.9.1.

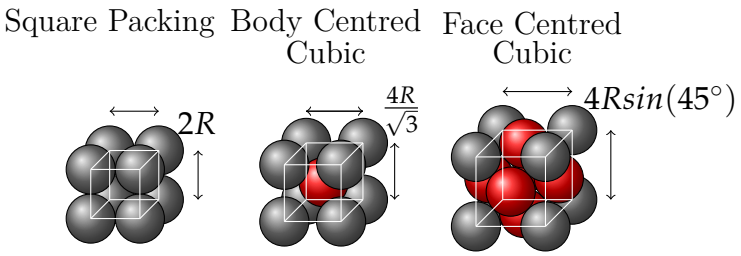


Figure 6.8.1: A diagram of the 3D geometries used in the heterogeneous Geant4 simulation, shown are the Square Packed, Face Centred Cubic and Body Centred Cubic unit cells. The grey and red colours denote the scintillator material and the white cube show the limits of the unit cell itself.

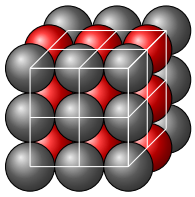

Figure 6.8.2: A diagram showing the 2x2 tiling of the 3D Square Packed unit cells, red and grey colours denote scintillating material. The void volume between spheres is occupied by the water and source.

## 6.9 Geant4 Model Results 3D

The convergence study employed by both 2D & 3D Geant4 configurations is shown in Fig. 6.9.1. For this, tritium and carbon 14 were chosen and the SP unit cells with the equivalent optimal radii calculated in the previous section from their data sets, e.g. 3.5 µm for the 2D tritium. The results reveal that for both 2D and 3D structures 1000 unit cells in each axis is the optimal.

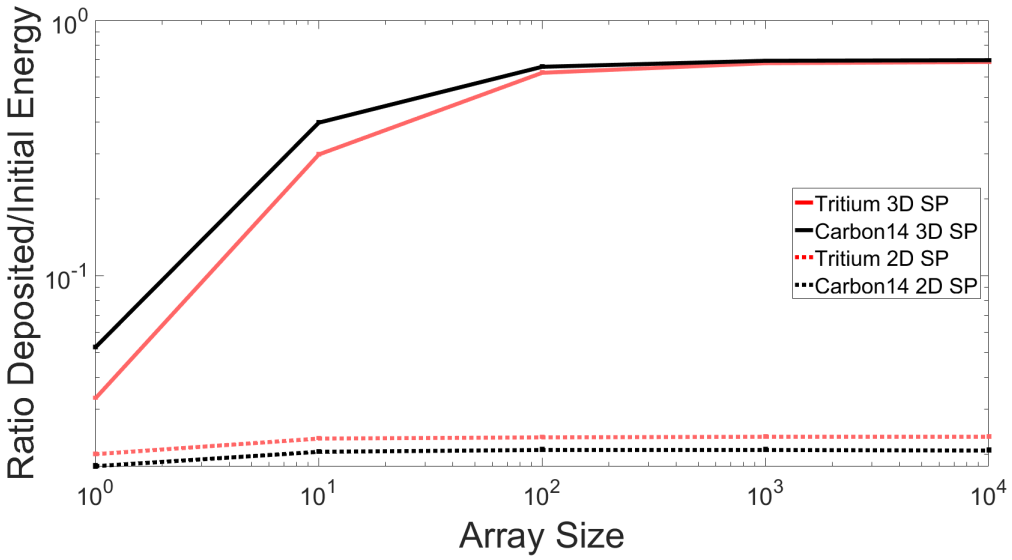


Figure 6.9.1: Results of the convergence test for the 2D & 3D square packed unit cells for tritium, carbon 14 & lead 210. Error bars are plotted but of small magnitude.

The raw non-normalised data for the 3D unit cells is located in Fig. 6.9.2, note that unlike the 2D data the $\hat{y}$ axis data is not normalised here. The results show that as the scintillator particles are reduced in size, the energy deposited in the scintillating particles, as compared to being attenuated in the water, increases, this is in agreement with previous research and explains why the liquid scintillator will always have the best possible detection efficiency as the scintillating particle is as small as possible. [113]. As with the 2D configurations the ideal normalisation method for the 3D data has been determined to be the maximum track length and maximum geometric track length value for each radioisotope. Figs. 6.9.3 and 6.9.4 show the 3D data normalised using the methods stated above. The remainder of the data with unsuccessful normalisation is located in the Appendix A.5.2. Whilst the 2D unit cells data (Chapter 6.7) showed that all three microparticle curves could be aligned using

these normalisation methods the same is not true for the 3D data. The methods do however give the best results as none of the other methods tested lead to such close alignment.

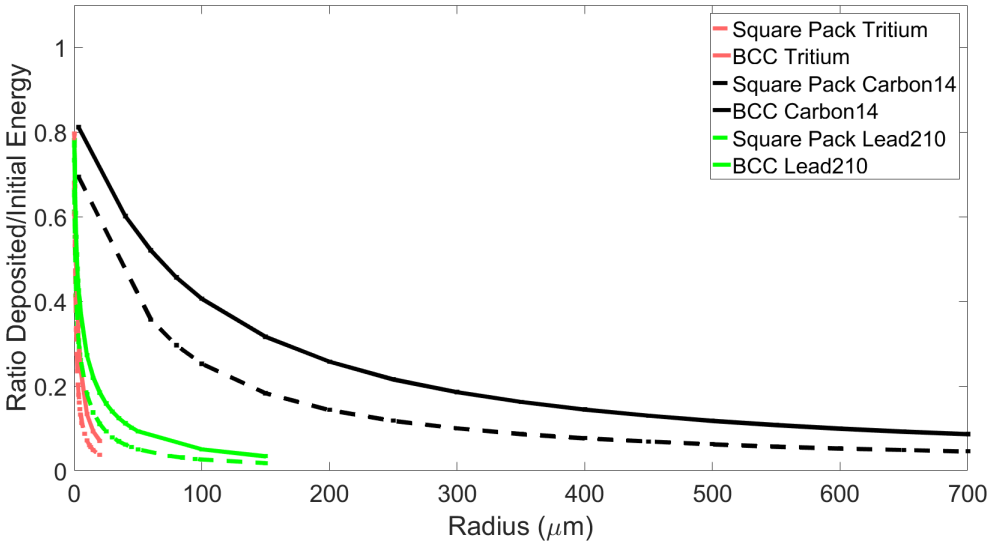


Figure 6.9.2: Results of the Geant4 3D heterogeneous scintillator simulation showing the radionuclides $^{3}$H, $^{14}$C & $^{210}$Pb. Face centred data is not plotted as it overlaps with the Square Pack data.

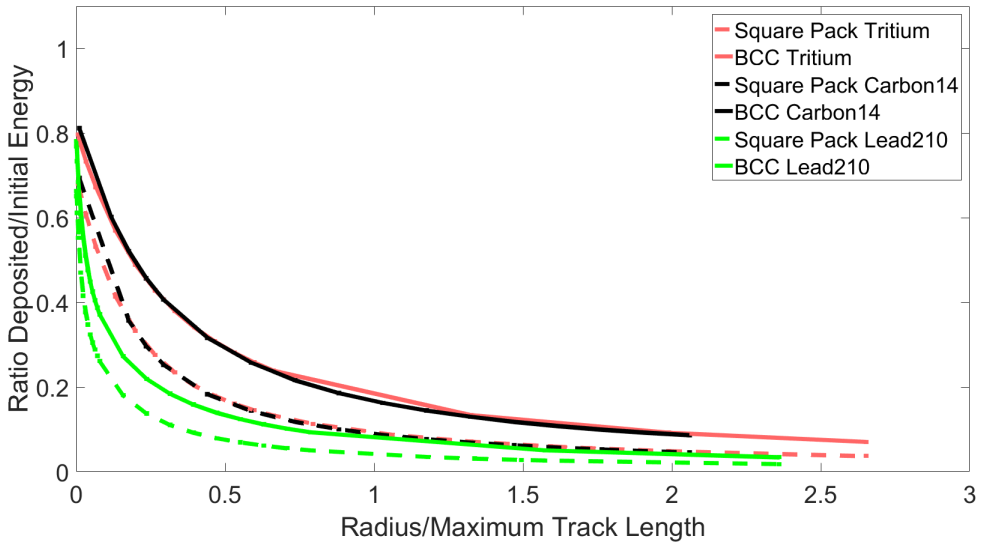


Figure 6.9.3: Results of the Geant4 3D heterogeneous scintillator simulation using $^{3}$H, $^{14}$C & $^{210}$Pb. These results are normalised using the Maximum Track Length values.

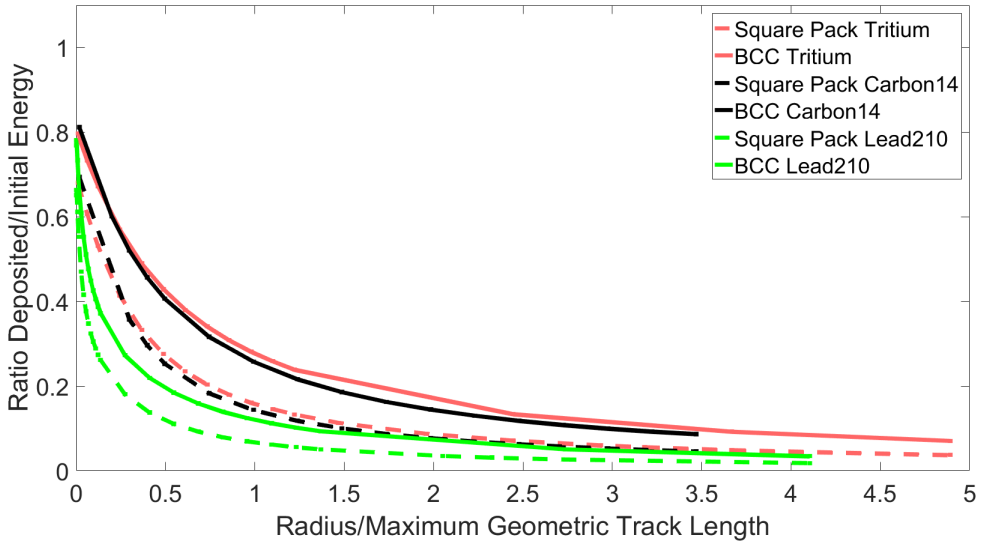


Figure 6.9.4: Results of the Geant4 3D heterogeneous scintillator simulation using $^{3}$H, $^{14}$C & $^{210}$Pb. These results are normalised using the Maximum Geometric Track Length.

Figure 6.9.5 reveals the similarity between the SP and FCC unit cells, with BCC plotted for comparison. As with the 2D data, the FCC curve overlays with the SP curve and so it has been omitted from the other figures in this section. The data showing the comparison between the use of $CaF_2$:Eu & CsI:Tl scintillators is located in Fig. 6.9.6. It can be seen that the physical properties of the scintillator do impact on the results. Although the curves are similar the simulations results are not independent of scintillator choice.

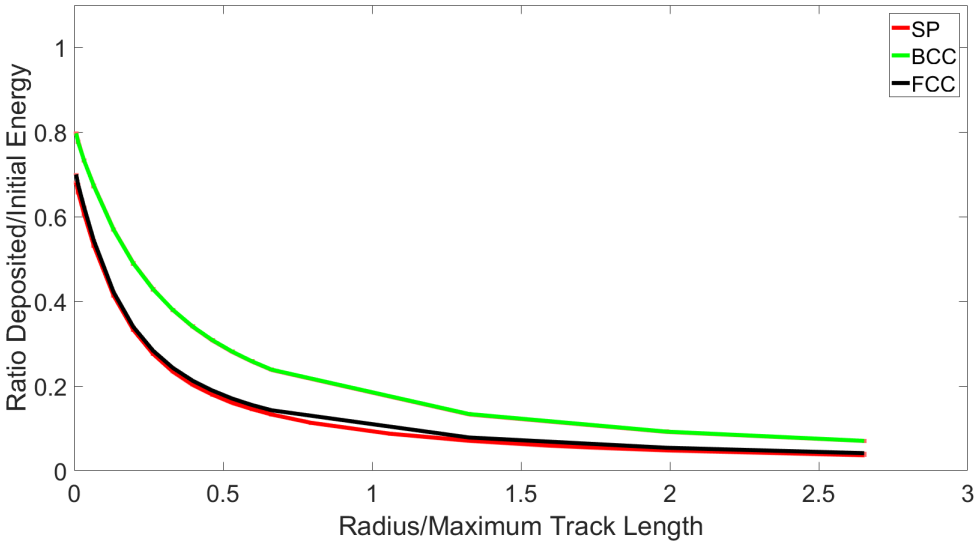


Figure 6.9.5: Geant4 simulation data of the 3D heterogeneous scintillator showing the 3D structures SP, FCC & BCC.

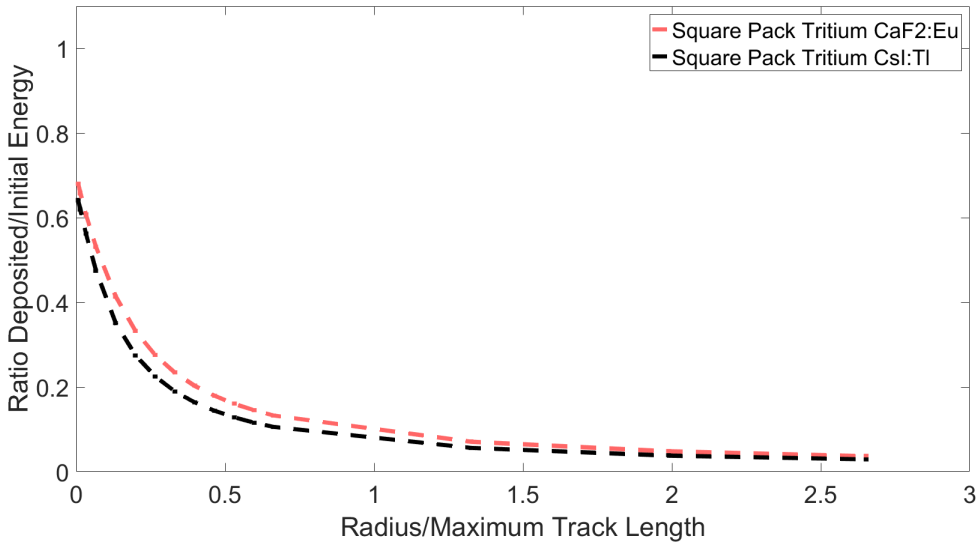


Figure 6.9.6: Geant4 simulation data of the 3D heterogeneous scintillator showing the $CaF_2$:Eu and CsI:Tl scintillators with a 3D SP $1000^3$ unit cells tritium arrangement.

## 6.10 Detector Flow Cell Model

The Geant4 model of the 3D unit cells was analysed further, this time including a simple calculation of the flow rate. Chapter 6.9 demonstrated through the 3D stacked particle unit cells that a practical flow-cell with small particles could achieve a high detection efficiency. This configuration has already been explored experimentally, e.g. [64]. One significant consequence is that there is a reduced flow rate. This section of the thesis explores the possibility of maximising both energy deposition detection and flow rate, leading to better detector designs. One potential application of the flow cell detectors is in detecting short lived concentration spikes of radioisotopes, such as an accidental spill into a river. It is in this situation that detectors with low flow rates are rendered ineffective, the purpose of this section is to maximise both the energy

deposition and flow rate through selecting an optimal scintillator particle radius.

### 6.10.1 Flow Rate Calculations

The flow rate through the 3D arrays has been analysed to determine whether particle size can affect transient concentration detection efficiency due to the restriction to flow and the time taken to fill a flow cell. The equation used to determine the flow rate is given in Eq. (6.10.1) [217, 218]. A number of assumptions have been made, as the flow cell will feature a pump, the provided pressure drop ($dp$) will be defined as 1000 Pa. This value is not reflective of an existing setup, a low pressure has also been chosen based on the situation, an in-situ detector will likely utilise a small low power pump, therefore a low pressure. The density of water has been assumed to be $1000\,\mathrm{kg\,m^{-3}}$, and the sphericity ($\Phi$) of the scintillator particle has been defined as 1. This is partly because the Geant4 simulation used the same assumption, likwise with simulations from other authors [113, 110], but also as the sphericity of the particles is not known. The length of the array ($dx$) as 100 mm, the void porosity ($\epsilon$) at 0.476, the viscosity ($\mu$) of water set to be 1.002 mPa s and the particle diameter ($D_p$) set to 3.5 µm. In using the equation Eq. (6.10.1) it is assumed that the flow is laminar, for this to apply the Reynolds Number should be less than one. The equation used for this is shown in (6.10.2) [219] and this work is featured fully in the Appendix A.7 section. The terms in (6.10.2) are, $R_e$ the Reynolds Number, $R$ the particle radius, $V_s$, the velocity of the fluid, $\mu$ the viscosity of water and $\epsilon$ the void porosity.

$$u = -\frac{dp}{dx}\frac{\Phi^2 D_p^2}{150\mu}\frac{\epsilon^3}{(1-\epsilon)^2} \tag{6.10.1}$$

$$R_e = \frac{2RV_s}{\mu(1-\epsilon)} \tag{6.10.2}$$

The energy deposition ratio and flow rate data for this section will be normalised in the $\hat{y}$ axis. This was completed by first subtracting the minimum value from each data set, then each data set was normalised to between 0 & 1. The optimal can then be found by multiplication of the ratio curve and flow rate curve.

### 6.10.2 Flow Cell Model Results

The results are plotted in Fig. 6.10.1 and the data has been normalised in both $\hat{x}$ & $\hat{y}$ axes. The $\hat{x}$ has been normalised through the maximum track length method, the $\hat{y}$ axis data has been normalised by the method stated in the previous section. The optimal radius values are then displayed in Table 6.10.1. The values for each radioisotope are the same with either $\hat{x}$ axis normalising method. The results can then be used to guide the design of a flow cell detector that approximates the 3D unit cell arrays.

Table 6.10.1: Data of the peak from the Optimal curves in Fig. 6.10.1. These values of Optimal Radius are unchanged with the $\hat{x}$ axis normalising method.

| Isotope | Optimal Radius (µm) |
|---|---|
| Tritium ($^{3}$H) | 10 |
| Carbon 14 ($^{14}$C) | 350 |
| Lead 210 ($^{210}$Pb) | 75 |

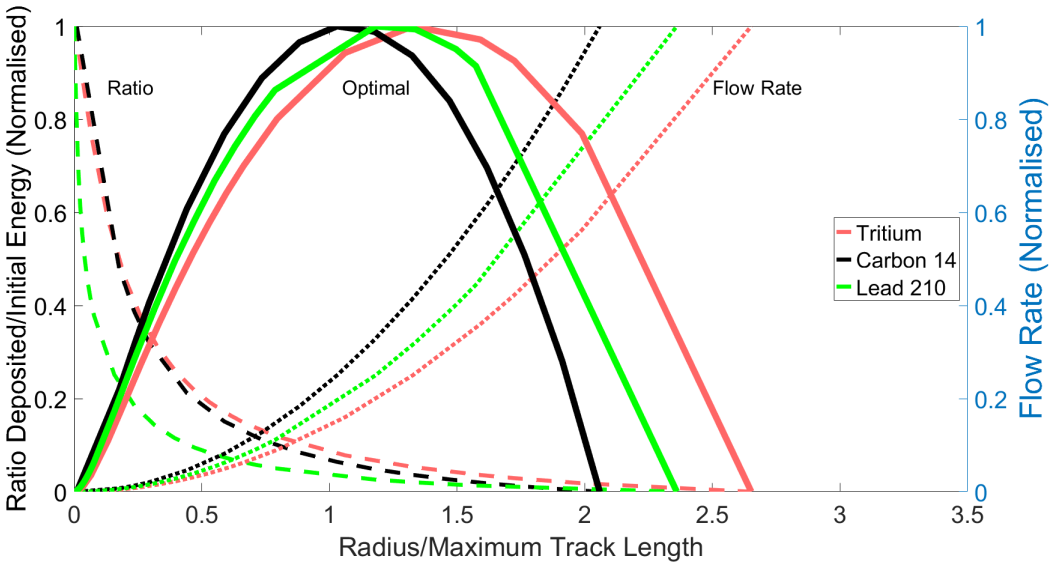


Figure 6.10.1: Data showing the optimal radius for a particulate heterogeneous 3D SP flow cell to maximise both the energy the beta particle desposits into the scintillator, and flow rate of the waterborne source.

## 6.11 Conclusions

The Geant4 simulations of the 2D microparticle unit cells reveal that a single layer leads to approximately 20% higher energy deposition in the scintillator, when compared with a single crystal. An experimental detector has been built employing a layer of $CaF_2$:Eu particles ($\sim$3.5 µm radius), this was compared with an equivalent single crystal with tritium in solution. The results show good agreement with the simulation. A number of methods have been attempted to normalise the simulation results along the $\hat{x}$ axis. Of these two were successful, as once normalised the peaks in the 2D data aligned. These two methods are the Maximum Track Length and Maximum Geometric Track Length and are related to the particles behaviour in water. The results of the dual 2D layer simulation revealed that with a very small gap between the layers there is an increase in the energy deposited. The simulations with the 3D unit cells showed that the energy deposited is maximised with the smallest radius. These results can also be normalised using the same method as the 2D, although the lead 210 data does not align as well. The combination of the 3D unit cell data and flow rate calculation demonstrates that while smaller scintillating particles mean less attenuation of the beta particles, it takes longer to fill flow cells with smaller particles making detection of transient activity levels less accurate.

The work investigating both the dual 2D layers, and optimising the radius for the 3D unit cells can provide a basis for experimental flow cell for radiation detection.

# Chapter 7

# Heterogeneous Scintillator Flow Cell

## 7.1 Introduction

The previous chapter demonstrated that a 2D planar heterogeneous scintillator experiences approximately 20% more energy deposition when compared with a single crystal that has the same projected area whilst using significantly less material. The advantage of more energy being deposited is that it will lead to an increase in the number of the scintillation photons produced, making detection of the radiation more efficient. The previous results were demonstrated for a single layer, which can be scaled up to be many layers, greatly increasing the surface area while still maintaining minimal material requirements. The advantage of this configuration is that it allows a significant flow rate through the cell as compared to equivalent 3D close-packed arrays, whilst still retaining the energy deposition increase over a single crystal. This chapter covers the development and testing of an experimental flow cell incorporating a heterogeneous scintillator comprised of multiple layers of 2D packed arrays of

scintillating particles, and its application to transient radioisotope detection.

## 7.2 Experimental Flow Cell Detector

The electronics for the detector were identical to the circuit from Chapter 6.5.1, and the same single Sensl C Series 60035 SiPM was employed. For the transient experiments, a peristaltic pump (120S with 114DV pump head) [220] was integrated with the flow cell. The shape of the flow cell can be seen in Fig. 7.2.1. The base and sides of the flow cell was machined from a single block of aluminium, the lid was made from transparent perspex. The top of the aluminium featured a rubber ring for the seal, with holes to screw the lid down and maintain a seal. The SiPM was mounted in the centre of the lid, with the remainder of the area covered in an optically reflective material. The inlet and outlet of the flow cell are located in the sides. A diagram of the aluminium base is shown in Fig. 7.2.1 and a photograph of the complete flow cell is located in Fig. 7.2.2. The integration of the flow cell and pump can be seen in the diagram in Fig. 7.2.3. The counting times used were 6 h with the source being either the tritium ($1500\,\mathrm{Bq\,mL^{-1}}$) or background de-ionised water. The flow rate of the pump when used was set to either $1\,\mathrm{mL\,min^{-1}}$ or $50\,\mathrm{mL\,min^{-1}}$. The fabrication of the scintillator discs is discussed in Appendix A.6.

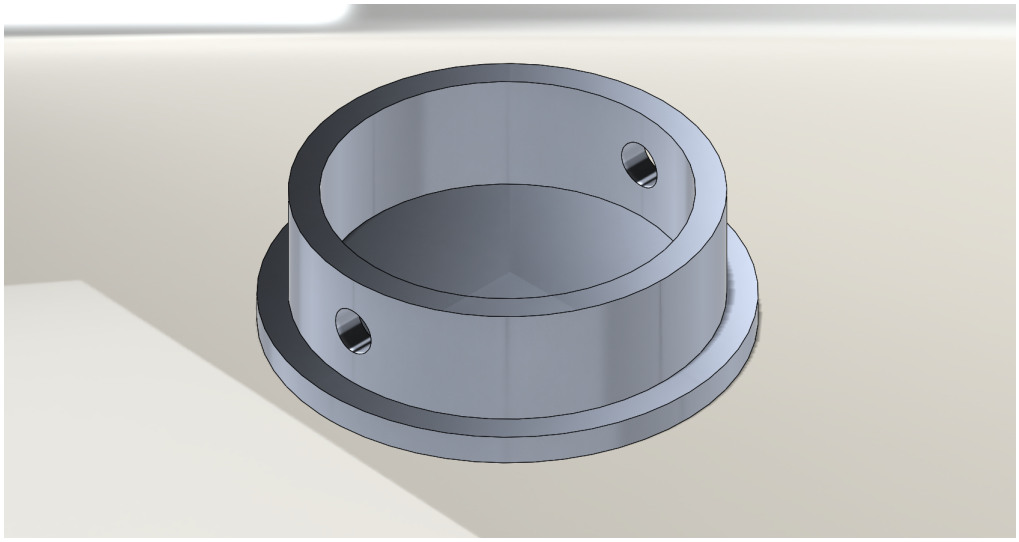

Figure 7.2.1: Diagram showing the aluminium base and sides of the flow cell.

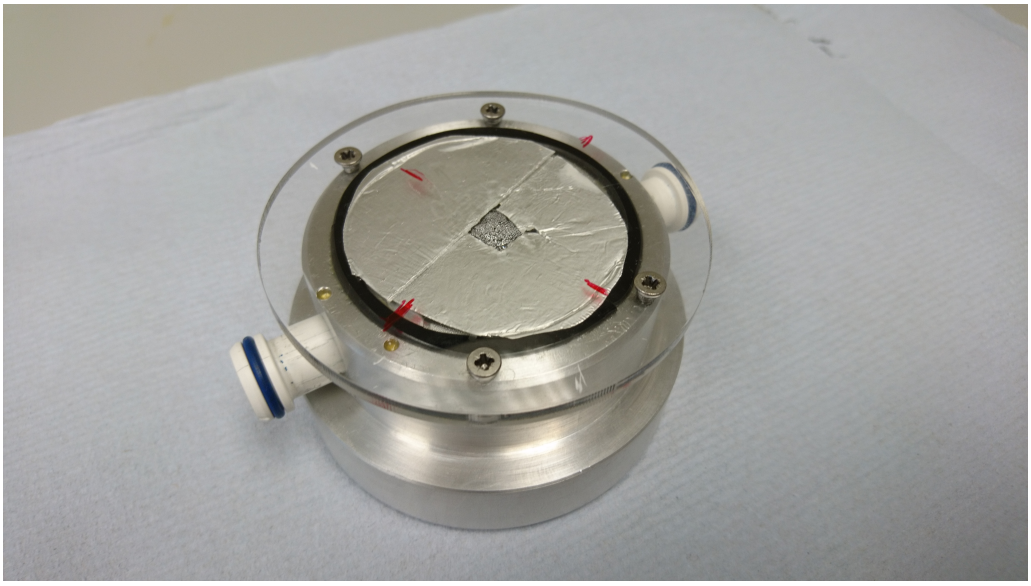

Figure 7.2.2: Image of the fabricated flow cell with the lid screwed on, the shape of base can be seen in the diagram in Fig. 7.2.1.

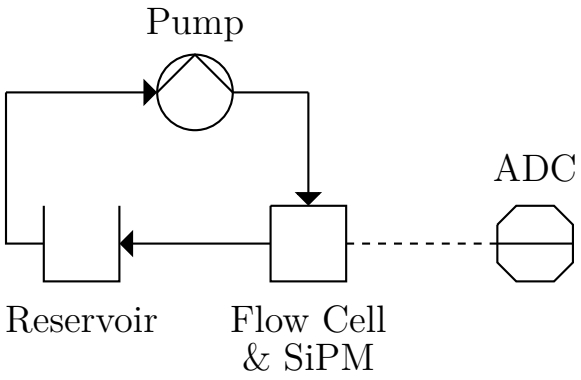


Figure 7.2.3: Diagram showing the components of the flow cell setup employed. The arrows indicate the flow of water & tritium source and dashed line the connection from the SiPM to the ADC.

### 7.2.1 Transient Radioisotope Concentration Level Detection

The concentration of a radioisotope in water can be transient and as such only detectable for a short period of time, such as an accidental discharge into a river. The full theory for detecting a transient radioisotope is in the Appendix A.7 [211]. A transient radioisotope is where the radioisotope only exists for a certain period of time, see Fig. A.7.1. As this theory explains, when a volume of water contaminated with a radioisotope passes the flow cell, it will then take time to fill the flow cell. As the contaminated volume passes through the flow cell the concentration of the radioisotope in the flow cell will decrease back to background. As the transient radioisotope fills the flow cell, the concentration of the flow cell volume will increase to equate to the transient source, the detector will then show a consistent count rate. However if the flow cell does not fill with the source, then the detected count rate will not plateau. Instead it will decrease with the cell becoming filled with non-contaminated water.

It is possible for the concentration inside the flow cell to not equate to the width of the transient source if it doesn't fill. There is then room to optimise an experimental detector to maintain a fast enough flow rate, and reasonable detection efficiency, and hence be able to detect a radioisotope that is only present for a short time.

The experimental setup used to validate this theory is shown in Fig. 7.2.4. Throughout the experiment the SiPM, flow-cell and readout electronics are inside of a light-proof box, with the pump and two beakers located outside. The transient experiment is conducted in four steps, the first is the circulation of DI water for a period of time using only a single beaker, labelled *Reservoir* in the figure. Then, step 2), a volume of known concentration of tritium is added into the same beaker and left to circulate and be counted. After a certain time has elapsed, the current beaker becomes the *Waste* beaker, then a second beaker *Reservoir* containing deionised water is used as the inlet to the pump, step 3). This will flush the system with deionised water, replacing all the now radiologically contaminated water with deionised water. At this point the outlet from the flow cell is placed into the reservoir, completing the circuit so that only deionised water is now in the system, step 4). The volumes and concentrations of tritium employed were based on the total volume of the system, not the amount of source added. For example if the total initial system volume is 100 mL of deionised water, and 200 mL of tritium with a concentration of $1500\,\mathrm{Bq\,mL^{-1}}$ is added, then the final concentration will be $1000\,\mathrm{Bq\,mL^{-1}}$.

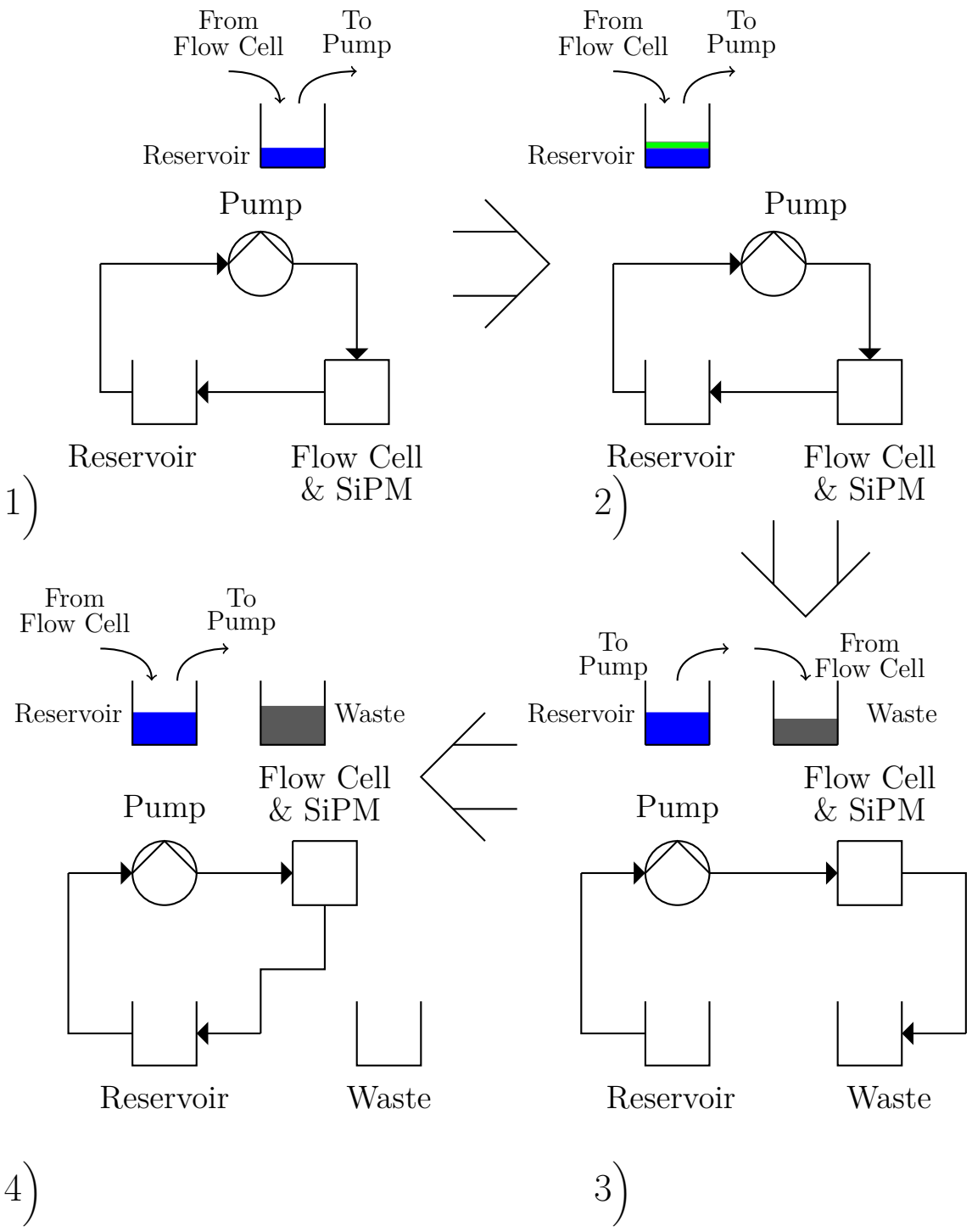


Figure 7.2.4: Diagram of the counting setup for a transient source of radiation. The experiment follows the setups shown numerically, blue denotes DI, green as tritium and grey as waste. The ADC is still included in the experimental setup but not shown in the figure.

## 7.3 Experimental Flow Cell Results

The results of the flow cell experiments can be seen in Table 7.3.1, the data here already has the background subtracted. The results demonstrate that increasing the number of layers leads to an increase in the detected counts from the same concentration of tritium validating the effectiveness of the methodology. The error for both tritium source and background was calculated as $\delta = \sqrt{N}$ [221], where $N$ is the number of counts. The equation used to calculate the error from the subtraction of the background count is shown in Eq. (7.3.1).

$$\delta_{Source-Background} = \sqrt{(\sqrt{\delta_{Source}})^2 + (\sqrt{\delta_{Background}})^2} \tag{7.3.1}$$

Table 7.3.1: Data showing the total counts of the two different scintillator experiments.

| Scintillation Detector | Total Counts in 6 h |
|---|---|
| Three layers 50 mL min$^{-1}$ flow rate | $271 \pm 31$ |
| Twelve layers 50 mL min$^{-1}$ flow rate | $11\,660 \pm 150$ |

An experiment was conducted to verify the transient radioisotope theory. For this a total of six hours were counted, the first hour of only deionised water, three hours with the tritium added and the final two hours of flushing the system with deionised water. During this, the flow rate was set to 1 mL min$^{-1}$ and the concentration of tritium after being added equated to 1000 Bq mL$^{-1}$. The results of this are shown in Fig. 7.3.1, with the background already subtracted. The experimental errors for the

subtraction of source and background are shown in Eq. (7.3.2). There is a DC offset in the data between the background and tritium, this is assumed to be the error, as it is also larger in magnitude than $\sqrt{N_{Source}}$. This method of calculating the error has not been applied to the previous data as this data set had a less consistent DC offset. The error in the tritium count is then:

$$Tritium \quad Error = \sqrt{(N_{Background})^2 + (N_{Source} \quad _{Error})^2} \tag{7.3.2}$$

The error in the averaged tritium data is calculated from error progagation [221]:

$$Averaged \quad Tritium \quad Error = \frac{Tritium \quad Error}{|Length \quad Of \quad Window \quad (hours)|} \tag{7.3.3}$$

The same dataset has been analysed in Figs. 7.3.1 and 7.3.2, the same peak detection algorithm from Chapter 6.5.1 has been utilised. The data has been analysed by using three windows for the cumulative counts, 15 min, 30 min and 60 min. Fig. 7.3.1 shows the raw total counts in each window, Fig. 7.3.2 presents the total counts divided by the length of counting window in hours. The same data set was further analysed using a rolling counting window, which can be seen in Figs. 7.3.3 and 7.3.4. It can be seen that with increasing the size sections analysed there is a smoothing effect. There is a single peak at ∼1.5 h in the data, this becomes less prominant with the 1 h windows of data. There is no known reason for this peak. The impact of the tritium on the data can be seen as the main peak starting at 4 h, the delay from when the source is added at 1 h is due to the low flow rate. Due to the length of tubing used it is estimated that the tritium will take ∼50 min to reach the flow cell, then a further ∼40 min to fill the flow cell. The prediction made in Appendix A.7 shows that with a low flow rate the peak will not plateau, as the flow cell never fills with the source.

This appears to be reflected in the data, however the larger 1 hour window does not show this due to the smoothing effect. From this data the 30 min window appears to be ideal, this is because there is a trade-off between smoothing out false positives and a rapid detection of the transient radioisotope.

An issue that arose in the data was the inconsistent signal offset, this can be seen in the presented data by the missing points at 4.5 h. Previous runs with the SiPM did show a signal offset which displayed minimal drift within the counting time, but varied a little day-to-day. The transient radioisotope data set contained a near 'step' change in the offset, which had not been observed before. Further attempts to run the experiment were made but yielded poor results, this has coincided with the unforeseen gradual failure of the SiPM. A new SiPM and associated PCB were used in attempted reruns of the experiment, the data initially displayed a reduced electronic noise and was missing the inconsistent signal offset of the failed one. Given that the SiPM failed gradually it would likely have affected the results in this section. In the transient radioisotope data (Figures 7.3.1 to 7.3.4) the presence of the peak at $\sim$1.5 h and the unexpectedly long delay before the main peak at 4 h could have been due to a failed or nearly failed SiPM. The inconsistent 'step' signal offset was not observed in the earlier data comparing the three and twelve layers with a static radioisotope concentration. These experiments were however not repeated with the new SiPM, therefore some caution should be exercised on the validity of those results.

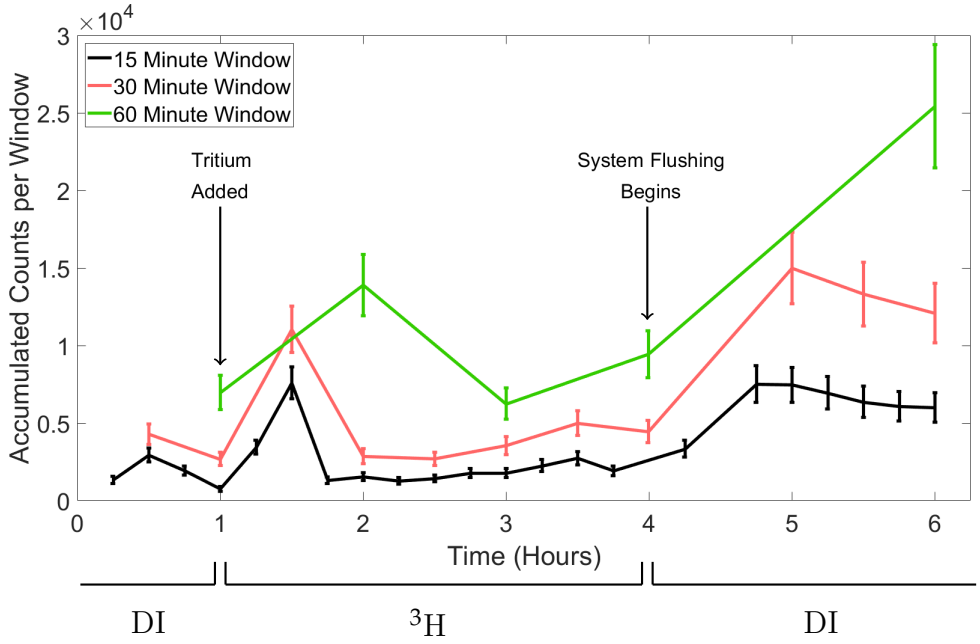


Figure 7.3.1: Data showing the transient flow experiment with the total counts per window of time. The data is analysed using the same data set.

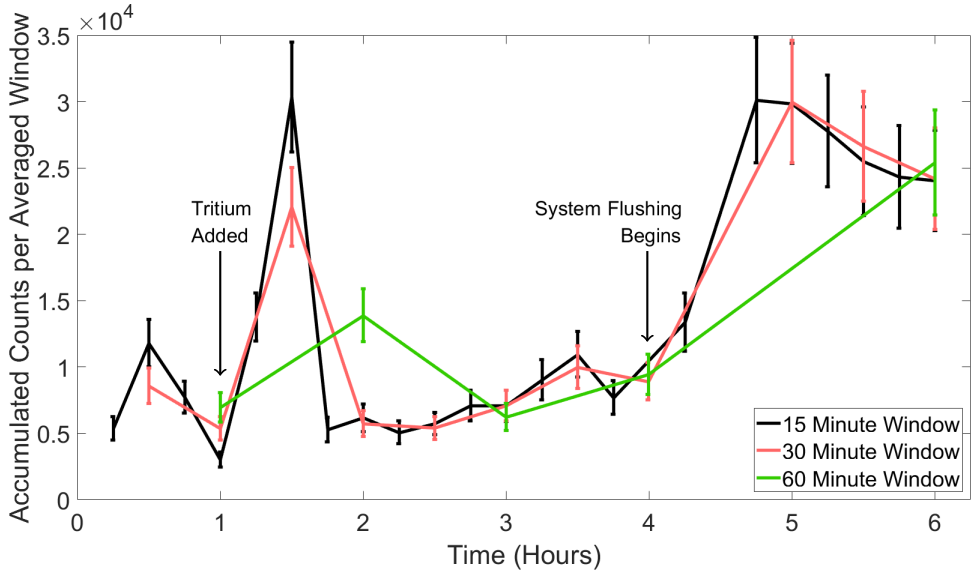


Figure 7.3.2: Data showing the transient flow experiment with the total counts per averaged window of time. The data is analysed using the same data set.

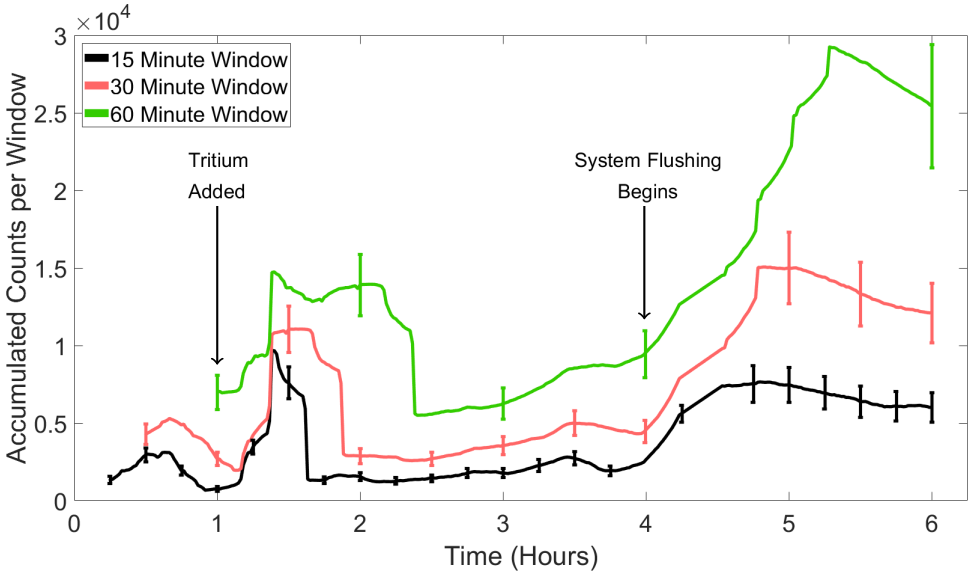


Figure 7.3.3: Data showing the transient flow experiment with the total counts per window of time. The data is analysed with a rolling counting window.

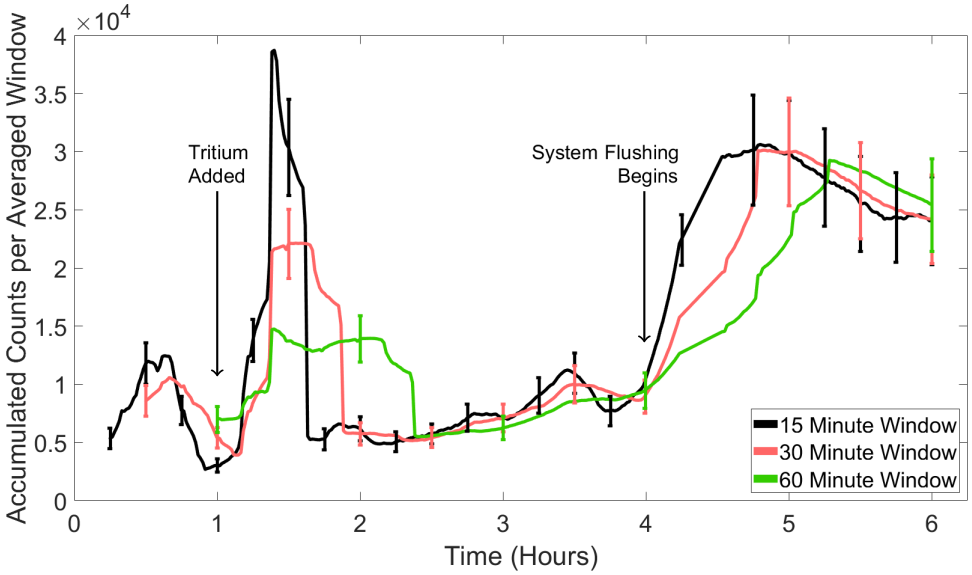


Figure 7.3.4: Data showing the transient flow experiment with the total counts per averaged window of time. The data is analysed with a rolling counting window.

## 7.4 Model of Averaging

A simple numerical model was used to investigate the effect of sampling for a window of time on the transient experimental data. This code was written in Matlab and modelled the count rate to follow the same shape as the numerical count rate prediction (Appendix A.7), the modelled data was then averaged using a moving window of fixed width. As the application of the transient flow cell detector is real-time monitoring, the sampling window and confidence in the cumulative counts data are important factors. The aim of this model is to determine the effect that the length of the counting window has on the detection confidence. The results for this are shown in Fig. 7.4.1, the black line is the modelled data with the averages as the coloured lines. This demonstrates that as the number of data points the average is performed over increases, the shape of the expected data is smoothed. In the in-situ situation the device would ideally detect very quickly when there is radiation present, in practice a large window of cumulative counting is needed for reasonable statistics. The larger the window the more confidence will be gained about possible detection, but this would delay the notification that radiation has been detected. A rolling cumulative windows could be used, it would still exhibit the same smoothing effect however.

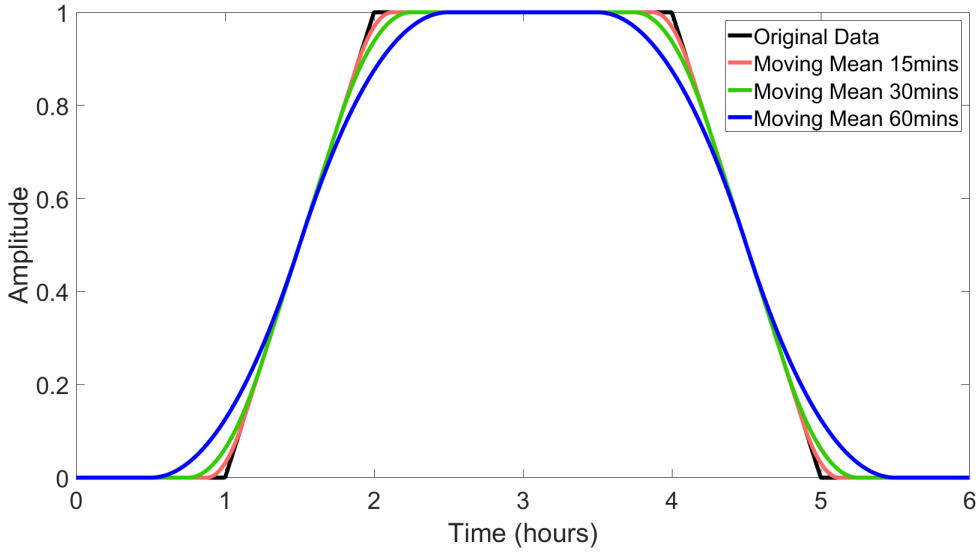


Figure 7.4.1: The results of the moving average model on expected data for the detection of a transient radioisotope. The black line is the expected data, the coloured lines for the moving average data.

## 7.5 Geant4 Model Definition

A model of the flow cell has been produced to examine the impact that a reflective top layer has on the detection efficiency. This model was written in Geant4 version 10.3 using the CentOS 7 VM. It is built & developed from the model used in Chapter 6.2.

### 7.5.1 Geant4 Flow Cell Geometry

The geometry employed is an evolution of the heterogeneous simulation from Chapter 6.2. The geometry was again built up from unit cells, although in this chapter only the square packed is used. The individual unit cell has a substrate with volumes of water above and beneath. Along with the scintillator spheres at both boundaries.

These unit cells were then tiled to form a thin cube, which is repeated vertically as required. These thin cubic layers reside in a hollow aluminium cylinder with an aluminium base to simulate the transmission or reflection of the scintillation photons on the flow cell walls, the experimental detector has this also which behaves as an optical reflector. Above this is the perspex/PMMA lid and a thin glass cube to represent the window to the SiPM. The diagram of a layer of the heterogeneous scintillator is shown in Fig. 7.5.1a, with two repeated layers in Fig. 7.5.1b.

The simulation was run twice to examine the impact that a reflective top surface had on the scintillation photon distribution, once with the top surface as transparent and once with it as reflective. For both runs the sphere radius was fixed to 3.5 µm, with 1001 unit cells in $\hat{x}$ & $\hat{y}$ axes. This number was selected as it was found to lead to a more stable simulation run, a total of six layers were used. The height of both the substrate layer and water layer was set to 5 mm. The SiPM had a height ($\hat{z}$) of 0.5 mm and widths ($\hat{x}$ & $\hat{y}$) of 6 mm.

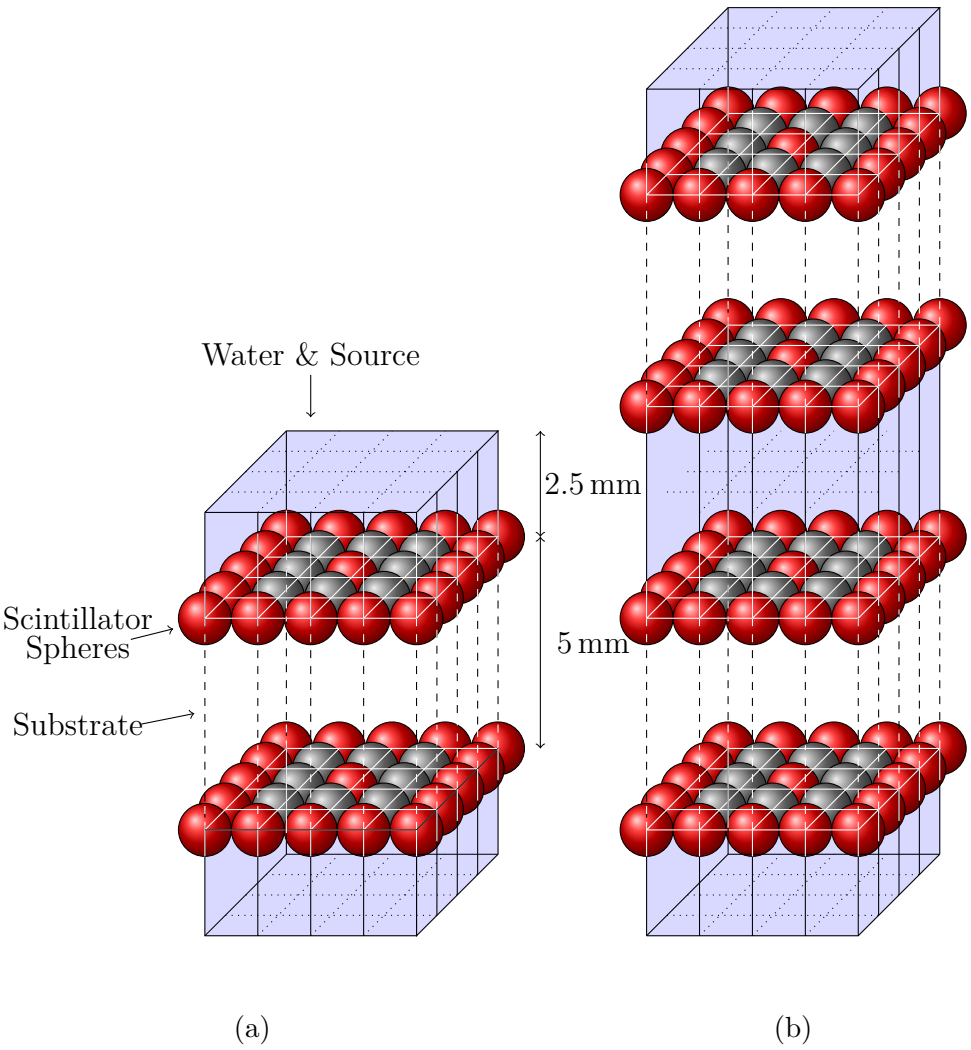


Figure 7.5.1: Diagram (a) showing the structure of a single layer of the 2D heterogeneous scintillator. This layer contains 4x4 ($\hat{x}$x$\hat{y}$) square pack unit cells, the substrate is shown in white. The scintillator in grey & red and the water and source volume in blue. (b) showing the structure of two repeated layers of a heterogeneous scintillator. This is a 4x4x2 ($\hat{x}$x$\hat{y}$x$\hat{z}$) arrangement using the same colour scheme as (a). The water volume is labelled as 2.5 mm as it is only half of the height between the layers of scintillator spheres.

### 7.5.2 Beta Source & Materials

The beta source used for this section employs the same histogram definition for the tritium energy spectrum as previous chapters. The beta source is represented in Fig. 7.5.1b by the blue cubic volumes.

The materials and their properties were modified from those in Chapter 6.2. The aluminium is included using the Geant4 NIST definition ($2.699\,\mathrm{g\,cm^{-3}}$) [141], PMMA defined as $C_5O_2H_8$, $1.18\,\mathrm{g\,cm^{-3}}$ [222, 223] and Polycarbonate defined as $C_{16}H_{18}O_5$, $1.21\,\mathrm{g\,cm^{-3}}$ [224, 225].

The optical properties of Al were assumed to be a reflectivity of 0.9 and electrophoton efficiency of 0.0. PMMA has a refractive index of 1.49 [223] and absorption length assumed to be 1.0 m, Polycarbonate has a refractive index of 1.585 [226] and absorption length assumed to be 1.0 m.

### 7.5.3 Data Analysis

The data has been analysed in a similar method to Chapter 6.2 in that there was a running total of the initial kinetic energies of all generated beta particles as well as summing the total energy deposited into the scintillator from all the beta particles. The photons were tracked and summed, both the initial number due to scintillation and the number arriving at the SiPM. The number of initial photons and those arriving at the SiPM for each event were printed.

For the same reasons as Chapter 6.2 any beta particles generated in a scintillator

sphere were killed immediately.

### 7.5.4 Physics Models Employed in Simulation

The physics selected for this section was a modification from Chapter 6.2, the changes were designed to further increase accuracy. The Livermore models for eIonisation and eBremsstrahlung were again used, G4EmParameters was called with the minimum energy set to 10 eV, lowest electron energy 100 eV and the SetIntegral to false. Atomic de-excitation (G4UAtomicDeexcitation) was enabled along with SetFluo, SetAuger and SetPIXE being set to true for fluorescence, the Auger effect and particle induced X-Ray emission.

## 7.6 Geant4 Results & Discussion

The results from the Geant4 model are shown in Figs. 7.6.1 and 7.6.2. The data reveals that making the top surface optically reflective makes a significant improvement to the number of photons arriving at the SiPM. These losses are due to the scintillation photons escaping from the non-reflective surface, and therefore not being detected by the SiPM. This will improve the detection efficiency due to the increased number of photons arriving at the SiPM, which is confirmed by the Geant4 results. No experimental data was collected to compare the Geant4 results with.

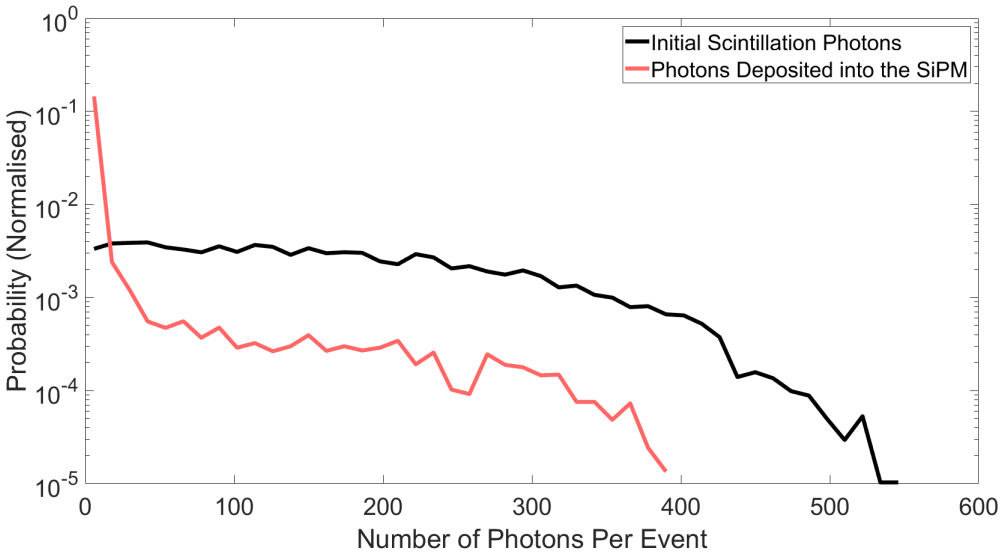


Figure 7.6.1: Simulation data showing the light collection losses by not having the top surface surrounding the SiPM as reflective.

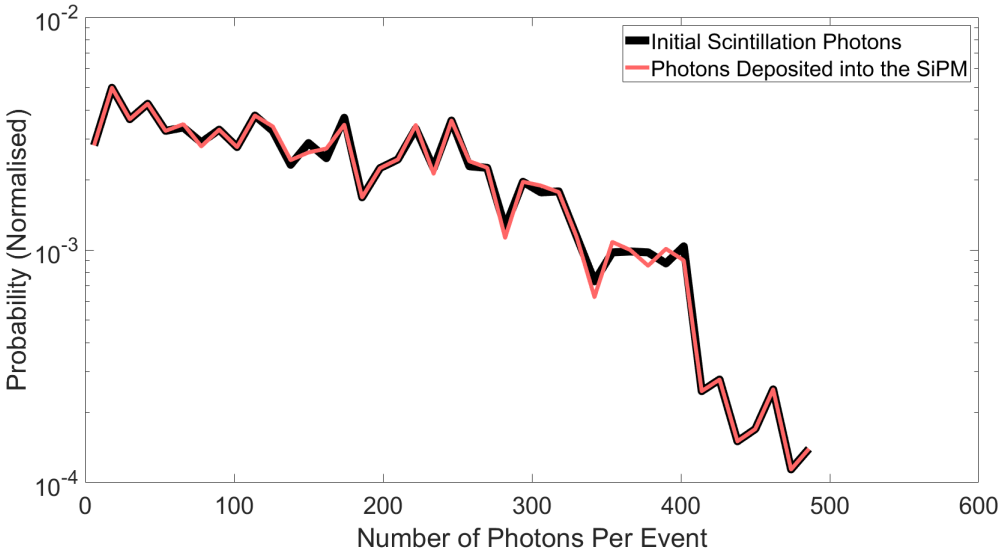


Figure 7.6.2: Simulation data showing the light collection efficiency when the top surface surrounding the SiPM is reflective.

## 7.7 Conclusions

The data of the perspex and polycarbonate layers show the expected increase in count rate with the flowing tritium source. Later equipment failure means that there is likely a systematic error in the static concentration data. The experimental data for the transient concentration shows only some agreement with the analytical prediction. It is anticipated that when the flow rate is too low the detector will not fill and therefore the count rate will never maximise. Instead there will be a broad peak, which is observed. Gradual failure of the SiPM used for detection casts doubt on the validity of the experimental data, the detection of an unexpected peak at 1.5 h and delayed main peak offer some validation for this assessment. The two experimental series, static concentration and transient concentration have not been repeated with a new setup, therefore it is not possible to verify the associated theory wthout these systematic errors.

The Geant4 simulation data reveals the importance of a complete optically reflective flow cell, when the lid was left transparent a significant number of the photons escaped.

# Chapter 8

# Conclusions

This final chapter provides an overview of the conclusions gained from this body of work. Recommendations will also be made regarding the direction of future work on this topic.

## 8.1 Thesis Conclusions

- When the tritium is located in water, i.e. tritiated water, it acts as a self-attenuating volume. This self-attenuation has two main effects on the beta particle as emitted due to the tritium decay, firstly that the range of the particles is reduced when compared with a medium that attenuates less, and secondly that the energy spectrum of those attenuated particles is shifted. This second result has been demonstrated through Monte Carlo simulation data of a volume of tritiated water and a single crystal inorganic scintillator. It has also been

verified through an analytical model of the attenuation. This result is important as any detection of tritium from tritiated water will need to account for this shift in the energy spectrum in order to discriminate between radioisotopes via spectra comparison. The same simulation data revealed that a 5 µm thick volume of the tritium was sufficient to replicate an infinitely thick volume of tritiated water, aiding in simulation design.

- A detector was made using a single crystal inorganic scintillator ($CaF_2$:Eu) and the associated electronics such as power regulation, pulse shaping and amplification.

- The radioisotope and scintillator were modelled using Geant4 Monte Carlo simulation software, the pulse shaping and amplification was modelled through circuit analysis and Matlab. Two beta emitting radioisotopes were examined, with the results show good agreement between the model and experimental detector. This model is then an accurate representation of the detector and can be refined as the detector improves.

- The most common approach to the fabrication of small particles of $CaF_2$:Eu is to grow them from a combination of precursor chemicals, however another method using a mortar and pestle was tested. The data presented shows that the mortar and pestle method achieved the desired particles size. The size of particles desired was 3.5 µm and the results showed a reasonable agreement.

- Geant4 modelling was used to investigate a novel heterogeneous scintillator

using 2D planar structure. This focused on the use of small particles of an inorganic scintillator arranged as a flat layer. This was compared with a single crystal of the same material in the situation where the source was a volume of radioisotope in solution. The results revealed that of the three beta emitters ($^{3}$H, $^{14}$C & $^{210}$Pb) simulated, each had an optimal radii of scintillator particle that 20% more energy was deposited into the scintillator for the heterogeneous scintillator in relation to the single crystal of equivalent projected surface area. This was validated experimentally utilising small $CaF_2$:Eu particles fabricated using the mortar & pestle method.

- Alongside simulation of this 2D planar heterogeneous scintillator 3D closed packed arrays of spheres were also simulated to act as a comparison. The data for 2D & 3D scintillators, along with three radioisotopes ($^{3}$H, $^{14}$C & $^{210}$Pb) were normalised using two constants, the maximum track length & maximum geometrical track length. These being the furthest the beta particle will travel in the medium, including scattering effects and straight line distance.

- The 3D packed arrays demonstrated that with decreasing radii of the particle, the percentage of the beta particles energy deposited increases. However the flow rate prediction showed that the decreasing radii reduces flow rate. By normalising the data, an optimal was found for each radioisotope that maximised both flow rate and energy deposited.

- The application of a scintillator for the detection of a transient radioisotope was explored. The analytical theory was paired with an experimental flow cell

featuring repeated layers of the 2D planar scintillator. The results offered some validation to the theory, showing the predicted lack of a plateau due to the flow cell not being filled with the tritium source. The results also show the impact that the sampling window has on the data, which is in agreement with the numerical prediction. The gradual failure of a key piece of instrumentation has introduced systematic errors into the experimental results.

- The main conclusion of this thesis is that for the detection of pure beta emitting radioisotopes in water by inorganic scintillator, a 2D planar heterogeneous scintillator will have 20% more energy deposited than a comparable single crystal.

## 8.2 Future Work

- The simulations investigating the 2D planar heterogeneous scintillator highlighted that the choice of inorganic scintillator did impact the results, this could be further explored in case there is a normalising factor to explain the data.

- The results for the 2D & 3D heterogeneous scintillator could be explored for other radioisotopes, including $^{14}$C and $^{210}$Pb. Other $\beta$ and $\alpha$ emitters could also be investigated such as those commonly discharged or leaked into the environment.

- The normalisation of the heterogeneous scintillator results were more effective with the 2D planar data than the 3D stacked particles. Additional normalisation methods might exist that could be as effective with the 3D data as with the 2D

data, such as scintillator physical properties.

- The results for the transient radioisotope and associated flow cell could be utilised in the design of a detector that could be field tested. This would also include the electronic and computational alterations needed for in-situ work. This would show how the device performs in the real situation, not in a lab.

- Whilst the design of the flow-cell has focused around tritium, due to its inherent detection challenges, it is worth considering other radioisotopes. Environmental discharges from nuclear facilities could benefit from a flow-cell that could detect and discriminate a number of $\beta$ and possibly $\alpha$ emitters too.

# Appendix A

# Appendix

## A.1 Penetration Lengths

Penetration length data not shown in the earlier Chapter 3.2, below is the remainder of the data.

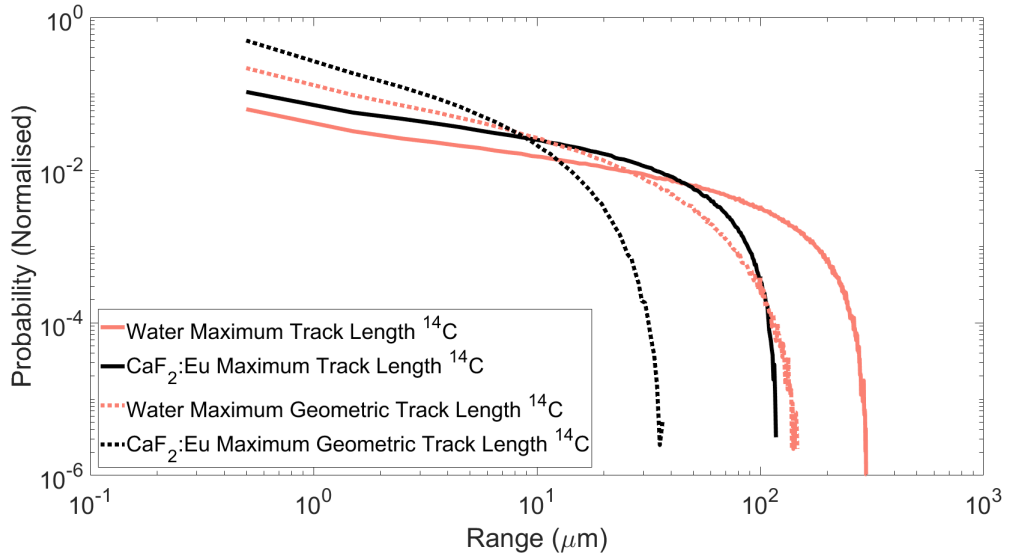


Figure A.1.1: Data showing the range of carbon 14 ($^{14}$C) beta particles in both water and $CaF_2$:Eu. The data is produced using a simple Geant4 simulation and the Livermore physics packages. Error bars are plotted but are of small magnitude.

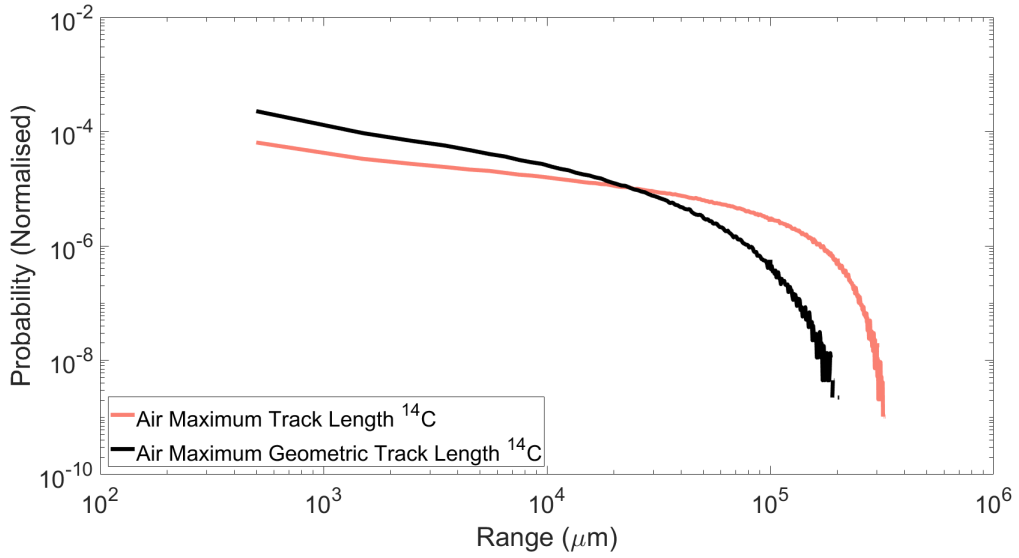


Figure A.1.2: Data showing the range of carbon 14 ($^{14}$C) beta particles in air. The data is produced using a simple Geant4 simulation and the Livermore physics packages. Error bars are plotted but are of small magnitude.

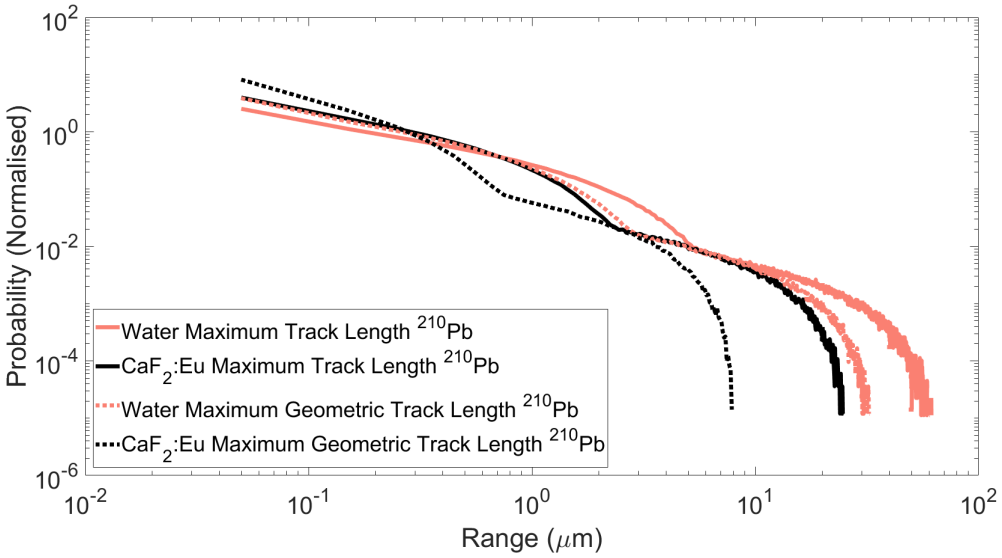


Figure A.1.3: Data showing the range of lead 210 ($^{210}$Pb) beta particles in both water and $CaF_2$:Eu. The data is produced using a simple Geant4 simulation and the Livermore physics packages. Error bars are plotted but are of small magnitude.

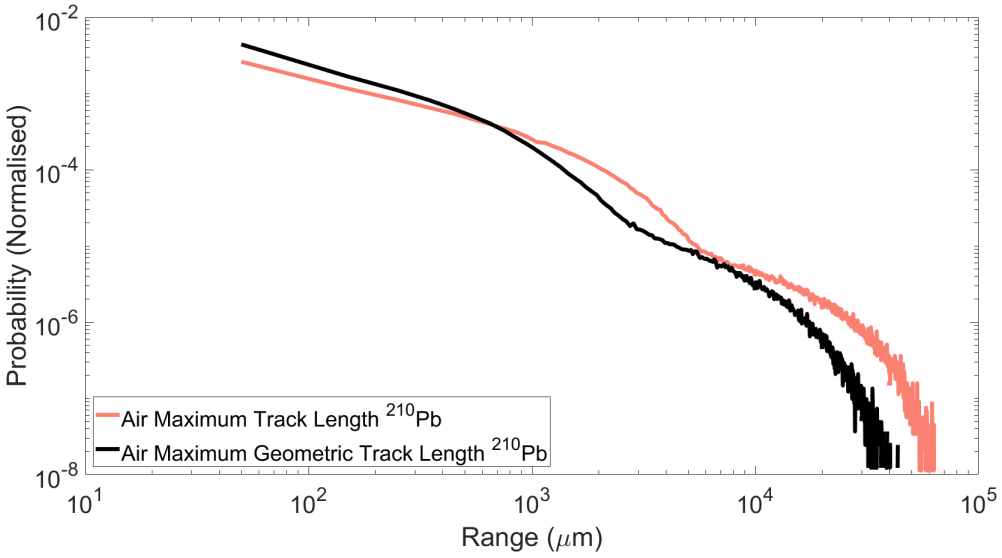


Figure A.1.4: Data showing the range of lead 210 ($^{210}$Pb) beta particles in air. The data is produced using a simple Geant4 simulation and the Livermore physics packages. Error bars are plotted but are of small magnitude.

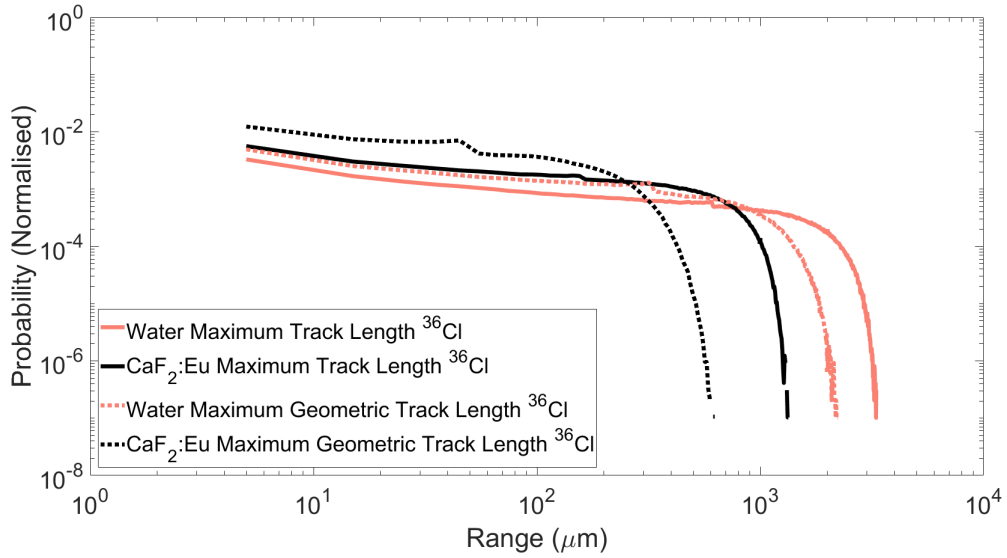


Figure A.1.5: Data showing the range of chlorine 36 ($^{36}$Cl) beta particles in both water and $CaF_2$:Eu. The data is produced using a simple Geant4 simulation and the Livermore physics packages. Error bars are plotted but are of small magnitude.

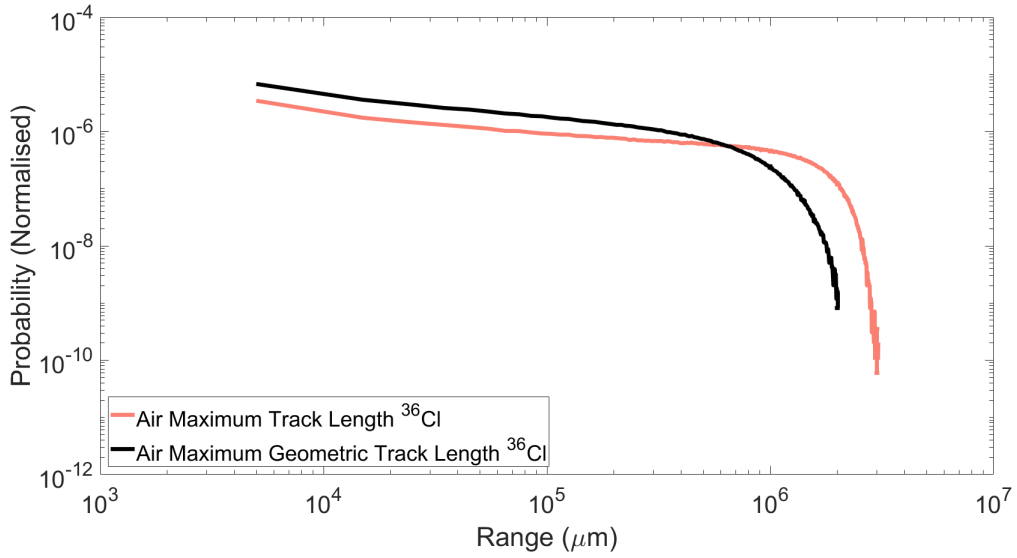


Figure A.1.6: Data showing the range of chlorine 36 ($^{36}$Cl) beta particles in air. The data is produced using a simple Geant4 simulation and the Livermore physics packages. Error bars are plotted but are of small magnitude.

## A.2 SiPM Bias Circuit

The following is the circuit diagram showing the method used to provide the bias voltage to the SiPM. This biasing method has been employed in Chapters 4.2. In this diagram the thick dashed line represents the SiPM, with the common cathode above and anode below. Whilst there are a few biasing circuits available this one was selected as the VBias is positive and the output pulse is with reference to 0 V. In this setup the Fast Out is left floating and only the Standard Out is used, labelled *Output*.

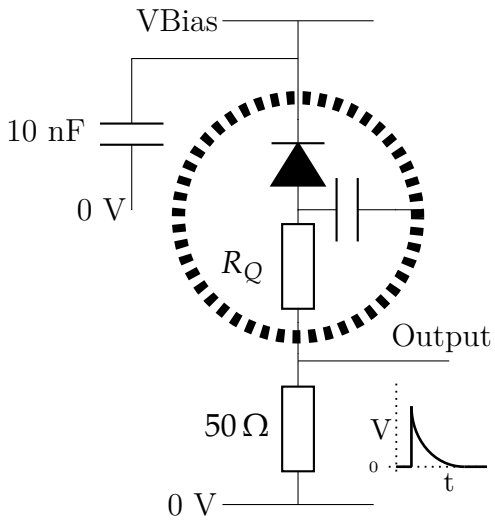


Figure A.2.1: SiPM voltage bias circuit, adapted from [227]. The SiPM is represented by the thick dashed line and the representation has been simplified to only a single diode, resistor and capacitor.

## A.3 Attenuation Numerical Prediction

The following is taken verbatim from the article [151] and covers the numerical prediction of the attenuated energy spectrum of tritium for Chapter 4.4, the figures have been removed.

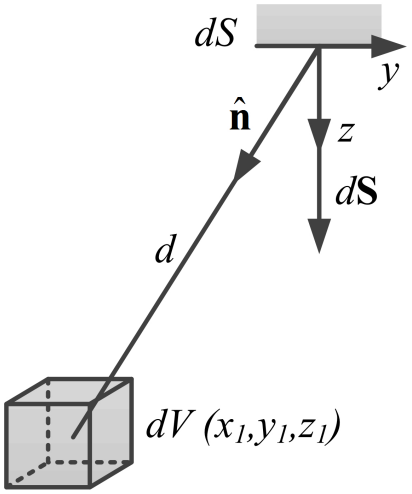


Figure A.3.1: "Geometry of β-particle interaction from a volume of tritiated water, $dV$, to an area on the scintillator $dS$. $d$ is the shortest distance from $dV$ to $dS$ and $\hat{n}$ is the unit vector from $dV$ to $dS$"[151].

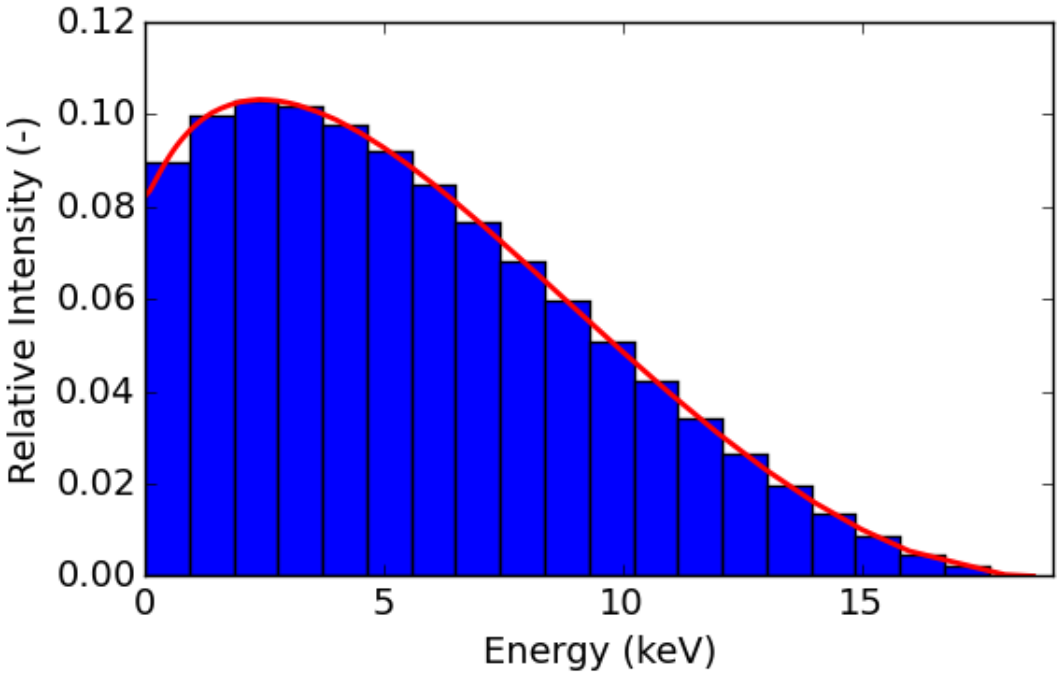


Figure A.3.2: "Probability mass functionof the relative intensity of β-particles emitted with a given initial kinetic energy $T_i$. The red line denotes the continous relative distribution N(T). Note k=20 for this figure, although it was 1000 during subsequent calculations"[151].

Consider a cylinder scintillator in contact with the surface of a volume of tritiated water with activity density A. The scintillator has a radius R and length h. An elemental volume of the tritiated water, where dV=dxdydz see Fig. A.3.1, emits beta particles in all directions with equal probability. The attenuation and scattering of the beta particles as it travels through the water is captured to first order by a linear attenuation coefficient (in $cm^{-1}$), denoted by $\mu$. Use of this coefficient assumes an exponential decrease in kinetic energy as the particle travels through the medium [228]. The rate of flux, $\Phi$, of beta particles passing through area dS on the scintillator surface is the product of the number of beta particles emanating from volume dV per second per steradian and the solid angle subtended by the area element and the exponential attenuation factor:

$$d\Phi = (\frac{AdV}{4\pi})\frac{\hat{n}\cdot d^2}{d^2}(e^{-\mu d}) = \frac{Ae^{-\mu d}}{4\pi d^2}\hat{n}\cdot dSdV \tag{A.3.1}$$

d is the shortest distance from dV to dS and $\hat{n}$ is the unit vector from dS to dV. Setting the base of the scintillator to be perpendicular to the z-axis as shown in Fig. A.3.1, an elemental area on the base, positioned at (x,y,0), can be denoted as dS=(0,0,1)dxdy. The rate of flux of beta particles emanating from volume dV and reaching area dS is therefore:

$$d\Phi = \frac{Ae^{-\mu d}}{4\pi d^2}\hat{n}dSdV = \frac{Az_1 exp\Big(-\mu[(x-x_1)^2+(y-y_1)^2+z_1^2]^{\frac{1}{2}}\Big)}{4\pi[(x-x_1)^2+(y-y_1)^2+z_1^2]^{\frac{3}{2}}}\quad dxdydz \tag{A.3.2}$$

Therefore the total flux of beta particles that can reach the base of the scintillator is:

$$\Phi_D = \int_{-\infty}^{0}\int_{-\infty}^{\infty}\int_{-\infty}^{\infty}\int_{-R}^{R}\int_{-\sqrt{R^2-x^2}}^{\sqrt{R^2-x^2}} \frac{Az_1 exp\Big(-\mu[(x-x_1)^2+(y-y_1)^2+z_1^2]^{\frac{1}{2}}\Big)}{4\pi[(x-x_1)^2+(y-y_1)^2+z_1^2]^{\frac{3}{2}}}\, dxdydx_1dy_1dz_1 \tag{A.3.3}$$

In practice, as the energy of the beta particles is small, numerical integration of Eq. A.3.2 can be over a much smaller domain (i.e. non-infinite) than suggested and still get accurate results. To simply this integral, the axisymmetry of the problem can be exploited by setting $x = rcos\phi$,$y = rsin\phi$,$dxdy = rdrd\phi$, $x_1 = r_1 cos\phi_1$,$y_1 = r_1 sin\phi_1$,$dx_1dy_1 = r_1dr_1d\phi_1$ yielding:

$$\Phi_D = \int_0^{2\pi}\int_0^{2\pi}\int_0^{R_v}\int_0^{R}\int_{-H_v}^{0} \frac{Arr_1z_1 exp\Big(-\mu[r^2+r_1^2-2rr_1cos(\phi-\phi_1)+z_1^2]^{\frac{1}{2}}\Big)}{4\pi[r^2+r_1^2-2rr_1cos(\phi-\phi_1)+z_1^2]^{\frac{3}{2}}}\, dz_1drdr_1d\phi d\phi_1 \tag{A.3.4}$$

This integral becomes singular when $r^2 + r_1^2 - cos(\theta) + z_1^2 = 0$ making it difficult to solve using brute force Monte Carlo and quadrature integration methods. This is because when $z_1 \to 0$ and $cos(\theta) \to 1$, the integral becomes singular when $r \to r_1$ which is an area inconveniently in the middle of the domain of integration preventing good convergence using the previously mentioned methods. However, the Vegas algorithm [229] which utilises both importance sampling and adaptive stratified sampling as implemented in Python using the Vegas 3.0 algorithm [230] yields satisfactory results. The mass attenuation was determined using the built in cross section files,

the mean free path and therefore the mass attenuation can be determined. The mass attenuation is a function of the initial kinetic energy of the beta particle. The mass attenuation can be calculated from Geant4 using the mean free path data at various energies, when fitting to this data a standard power-law relationship is observed:

$$\left(\frac{\mu}{\rho}\right) = \frac{1.28}{T^{1.74}} \tag{A.3.5}$$

where T is the initial kinetic energy of the beta particle in MeV and ρ is the density of water $\mathrm{g\,cm^{-3}}$. The coefficient in Eq. A.3.6 are 1.28±0.0390 and 1.74±0.0061 respectively where the errors denote a 95% confidence level. The coefficient of determination [231] for the fit is 0.938 (see Fig. 4.4.4). The beta particles are emitted from the tritiated water with a spectrum of possible energies as shown in Fig. A.3.2. This can be conveniently presented by a probability mass function so that the ith group of beta particles can be treated as a monoenergetic beam with initial kinetic energy:

$$T_i = \frac{Q}{k}\left(i - \frac{1}{2}\right) \tag{A.3.6}$$

here Q is the maximum kinetic energy (18.59 keV) and k is the total number of groups. The relative emitted intensity, i.e. the proportion of beta particles that are emitted with kinetic energy $T_i$ can be shown to be:

$$I_i = \frac{\int_{T_{i-\frac{1}{2}}}^{T_{i+\frac{1}{2}}} N(T) \quad dT}{\int_0^Q N(T) \quad dT} \tag{A.3.7}$$

where N(T) is the energy spectrum for tritium. In this way, the energy spectrum can be represented in Fig. A.3.2. The flux on the scintillator surface due to beta particles

of initial kinetic energy $T_i$ being emitted over the entire volume of tritiated water is therefore:

$$\Phi_i = \int_0^{2\pi} \int_0^{R_v} \int_0^{R} \int_{-H_v}^{0} \frac{AI_i r r_1 z_1 exp\Big( - \mu [r^2 + r_1^2 - 2rr_1 cos(\theta) + z_1^2]^{\frac{1}{2}} \Big)}{2[r^2 + r_1^2 - 2rr_1 cos(\theta) + z_1^2]^{\frac{1}{2}}} \quad dz_1 dr dr_1 d\theta \tag{A.3.8}$$

The total flux is defined simply as:

$$\Phi_T = \sum_{i=0}^{k} \Phi_i \tag{A.3.9}$$

The attenuated energy spectrum of the beta particles colliding with the scintillator surface is:

$$N_A = \sum_{i=0}^{k} \left( T_i \Phi_i \frac{1}{n} \sum_{j=0}^{n} exp(-\mu_i d_j) \right) \tag{A.3.10}$$

for all $d_j$. This can be calculated by randomly generating a list of n (where n is very large, here $10^6$ was used) pairs of coordinates, where one set of coordinates spans the whole volume of tritium and the other set is over the entire surface of the scintillator.

## A.4 Heterogeneous Scintillator Fabrication

This chapter presents the remainder of the data from Chapter 5.3.2.

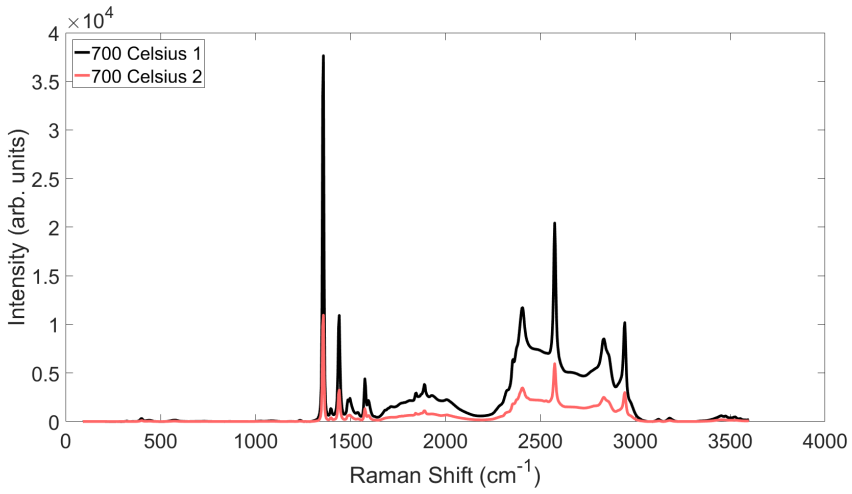


Figure A.4.1: Raman results of the spray deposited $CaF_2$:Eu onto a 200 °C hot plate, which were annealed at 700 °C.

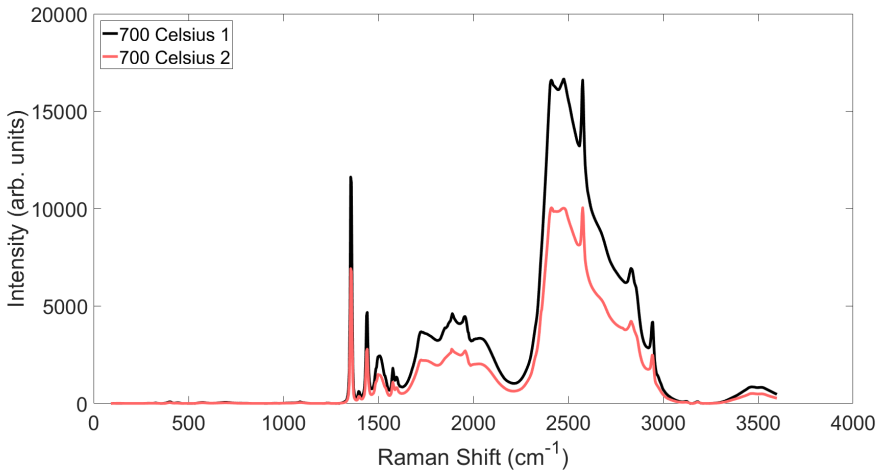


Figure A.4.2: Raman results of the spray deposited $CaF_2$:Eu, which were annealed at 700 °C.

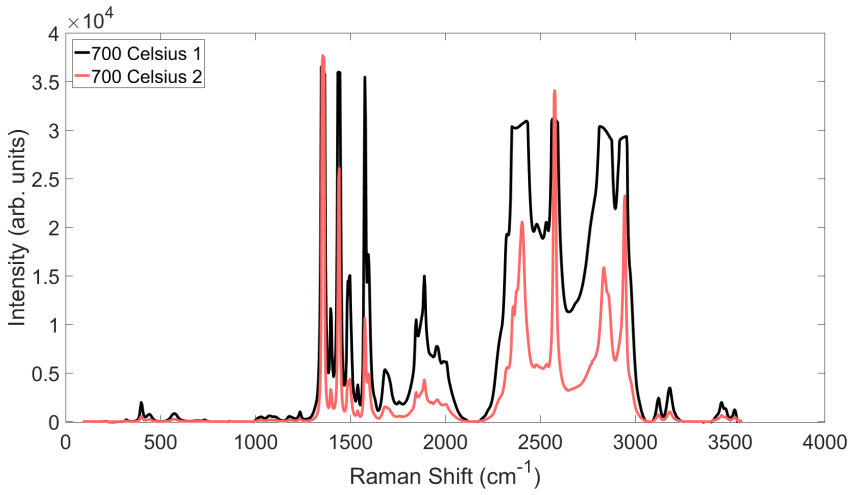


Figure A.4.3: Raman results of the spray deposited $CaF_2$:Eu, which were annealed at 700 °C.

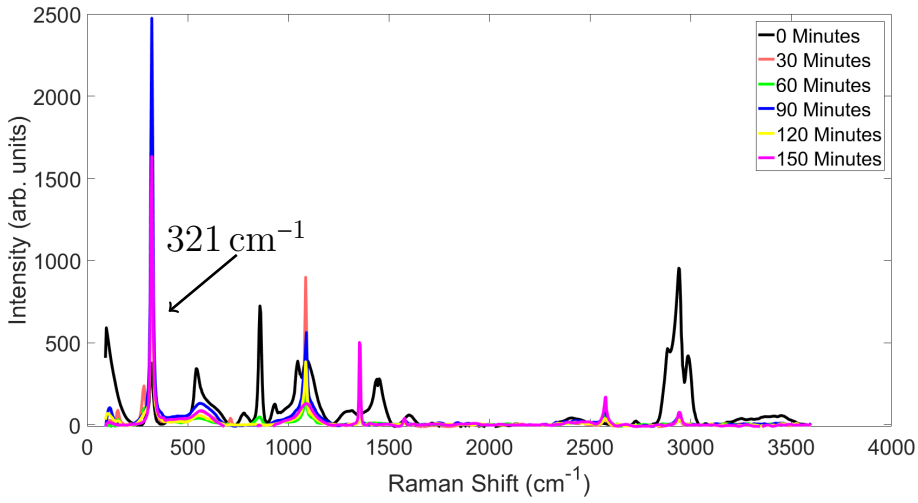


Figure A.4.4: Raman spectra of the $CaF_2$ samples spray desposited at 150 °C and annealed at 700 °C with annealing times shown.

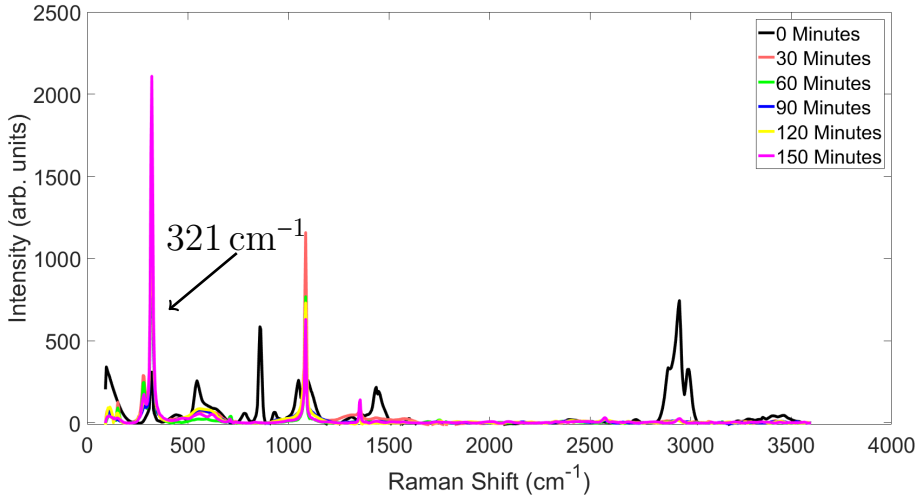


Figure A.4.5: Raman spectra of the $CaF_2$ samples spray desposited at 200 °C and annealed at 700 °C with annealing times shown.

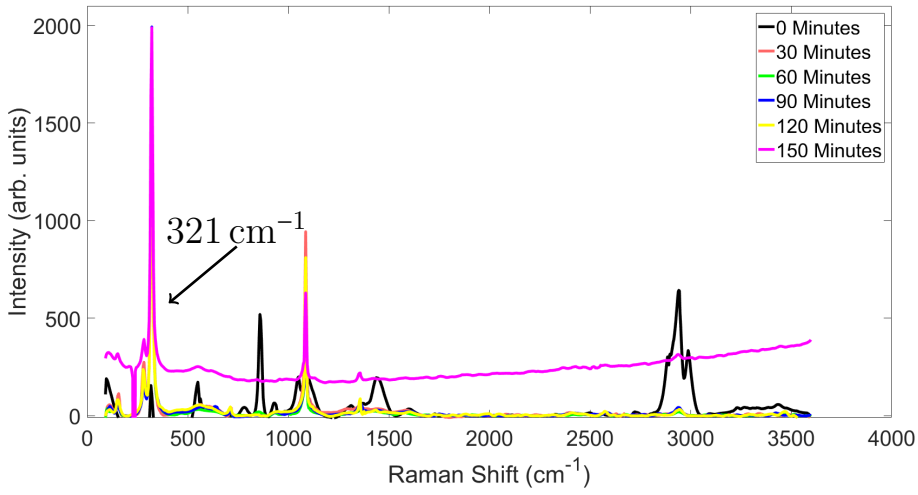


Figure A.4.6: Raman spectra of the $CaF_2$ samples spray desposited at 250 °C and annealed at 700 °C with annealing times shown.

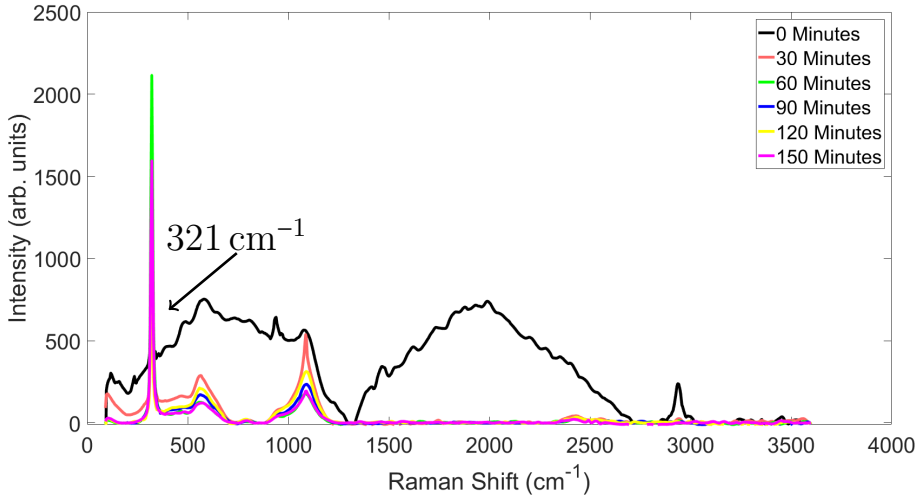


Figure A.4.7: Raman spectra of the $CaF_2$ samples spray desposited at 300 °C and annealed at 700 °C with annealing times shown.

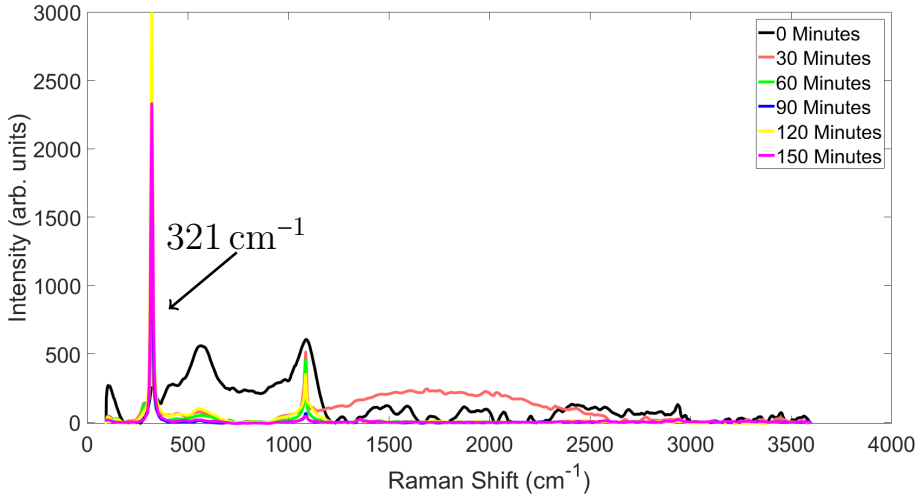


Figure A.4.8: Raman spectra of the $CaF_2$ samples spray desposited at 350 °C and annealed at 700 °C with annealing times shown.

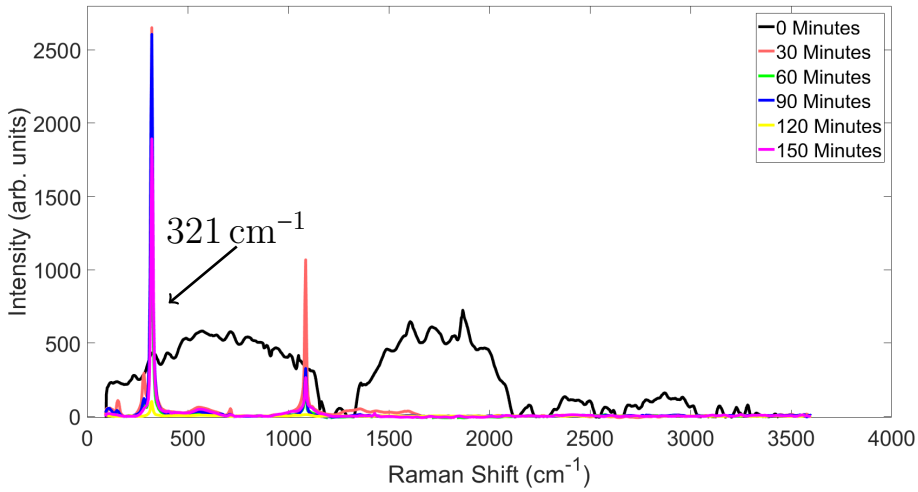


Figure A.4.9: Raman spectra of the $CaF_2$ samples spray desposited at 400 °C and annealed at 700 °C with annealing times shown.

## A.5 Heterogeneous Scintillator Simulation

This chapter contains the remaining Geant4 simulation results investigating heterogeneous scintillator normalisation from Chapter 6.7 & 6.9 respectively.

### A.5.1 2D Structure Results

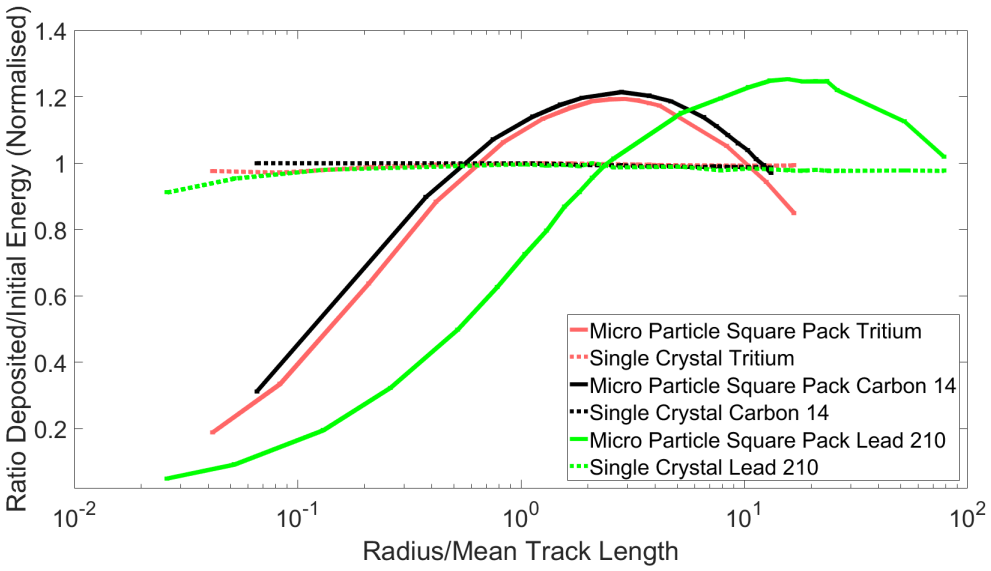


Figure A.5.1: The results of the Geant4 2D single crystal and heterogeneous scintillator simulations using the $^{3}$H, $^{14}$C & $^{210}$Pb. These results are normalised using the Mean Track Length values.

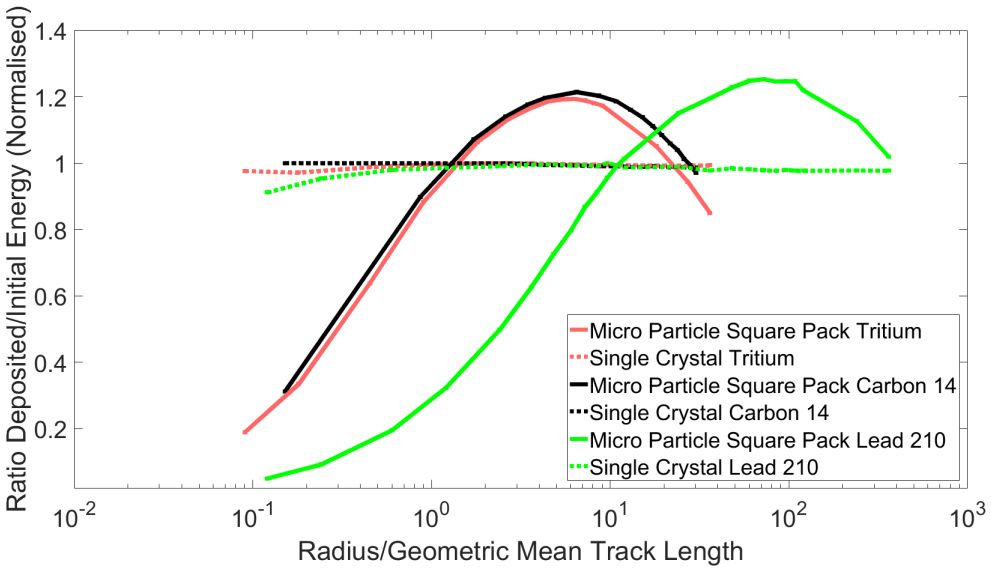


Figure A.5.2: The results of the Geant4 2D single crystal and heterogeneous scintillator simulations using the $^{3}$H, $^{14}$C & $^{210}$Pb. These results are normalised using the Geometric Mean Track Length values.

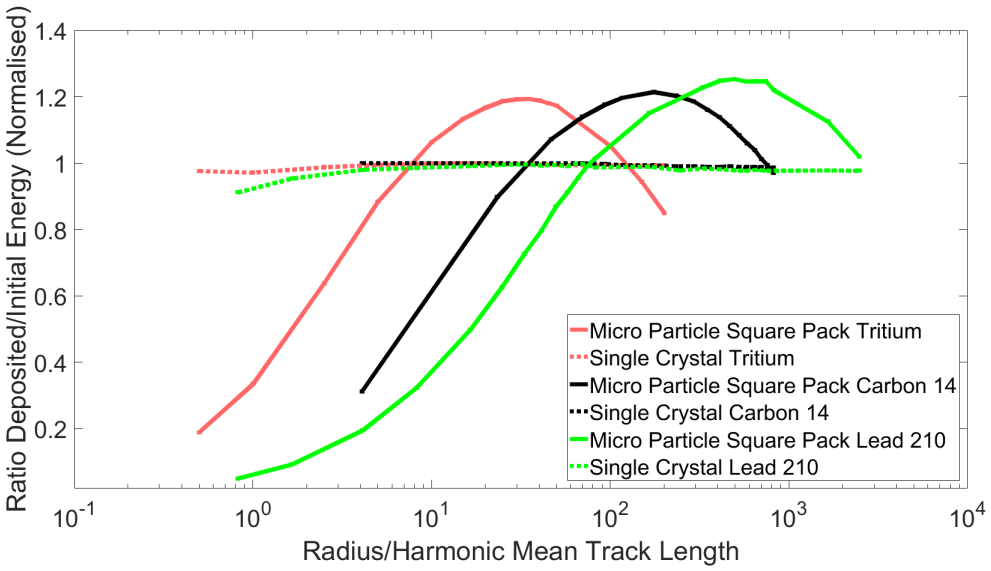


Figure A.5.3: The results of the Geant4 2D single crystal and heterogeneous scintillator simulations using the $^{3}$H, $^{14}$C & $^{210}$Pb. These results are normalised using the Harmonic Mean Track Length values.

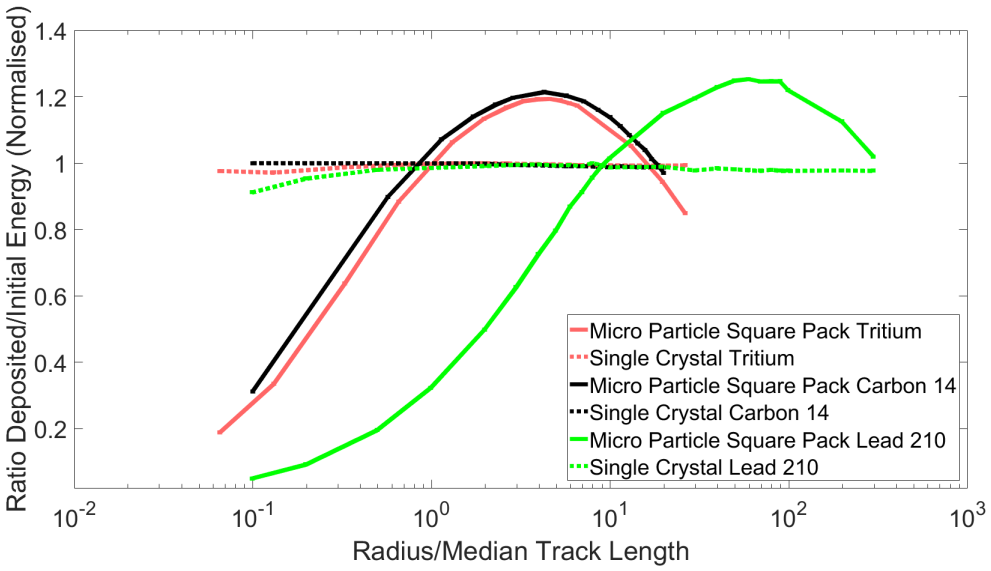


Figure A.5.4: The results of the Geant4 2D single crystal and heterogeneous scintillator simulations using the $^{3}$H, $^{14}$C & $^{210}$Pb. These results are normalised using the Median Track Length values.

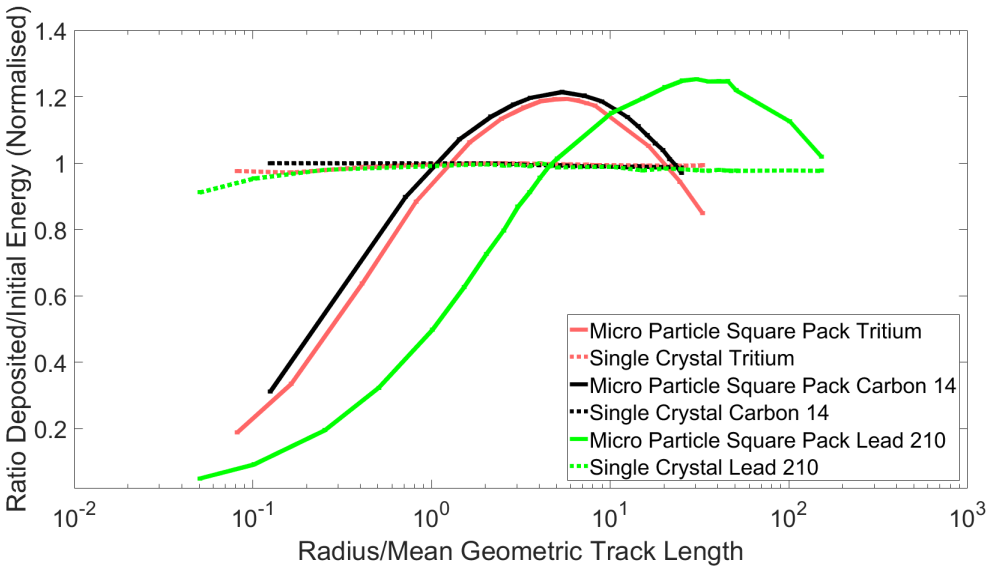


Figure A.5.5: The results of the Geant4 2D single crystal and heterogeneous scintillator simulations using the $^{3}$H, $^{14}$C & $^{210}$Pb. These results are normalised using the Mean Geometric Track Length values.

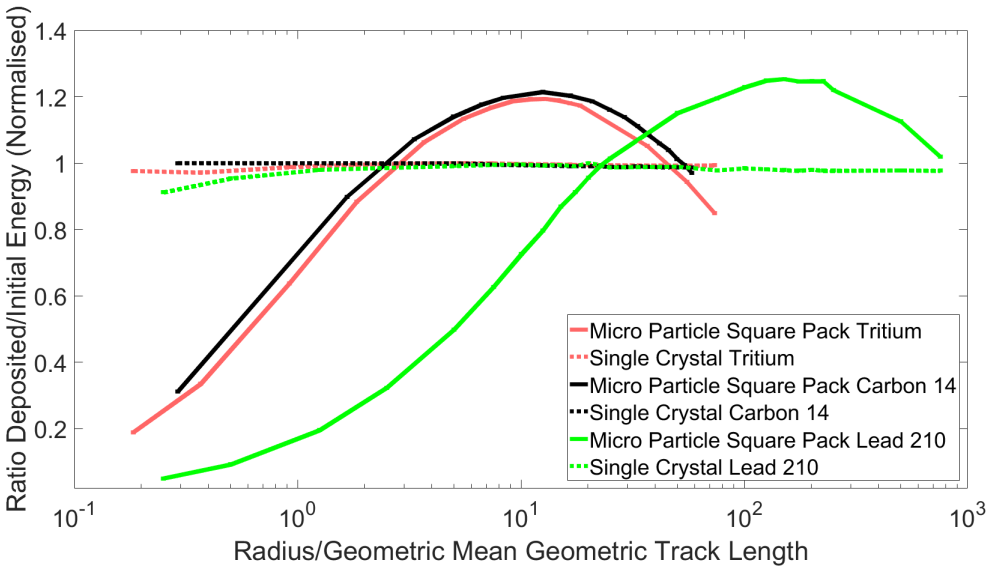


Figure A.5.6: The results of the Geant4 2D single crystal and heterogeneous scintillator simulations using the $^{3}$H, $^{14}$C & $^{210}$Pb. These results are normalised using the Geometric Mean Geometric Track Length values.

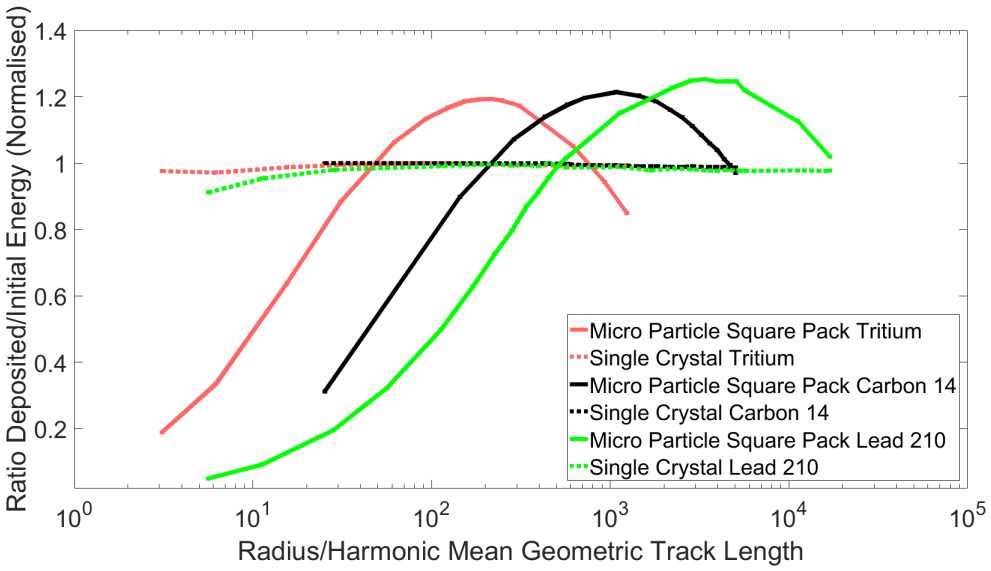


Figure A.5.7: The results of the Geant4 2D single crystal and heterogeneous scintillator simulations using the $^{3}$H, $^{14}$C & $^{210}$Pb. These results are normalised using the Harmonic Mean Geometric Track Length values.

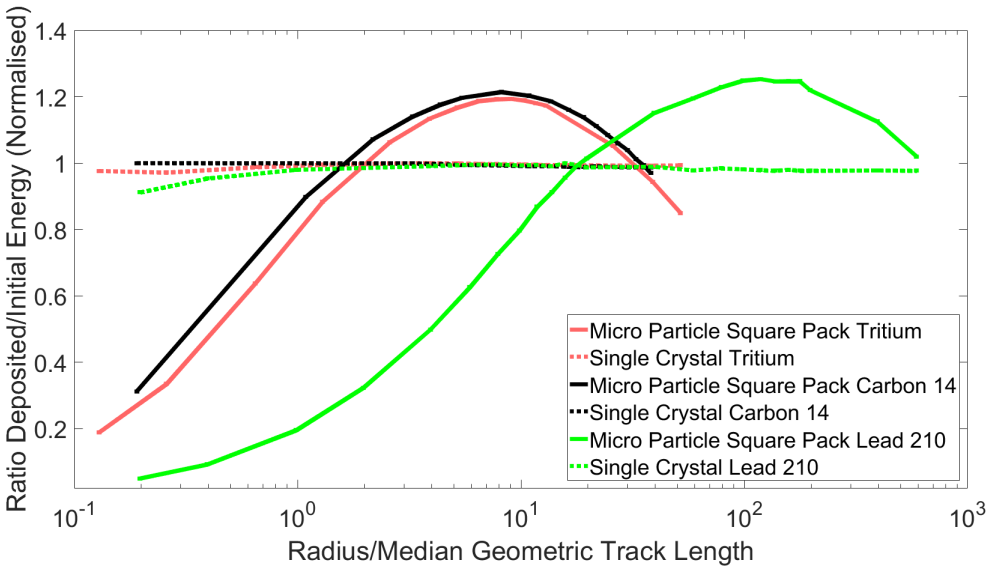


Figure A.5.8: The results of the Geant4 2D single crystal and heterogeneous scintillator simulations using the $^{3}$H, $^{14}$C & $^{210}$Pb. These results are normalised using the Median Geometric Track Length values.

### A.5.2 3D Structure Results

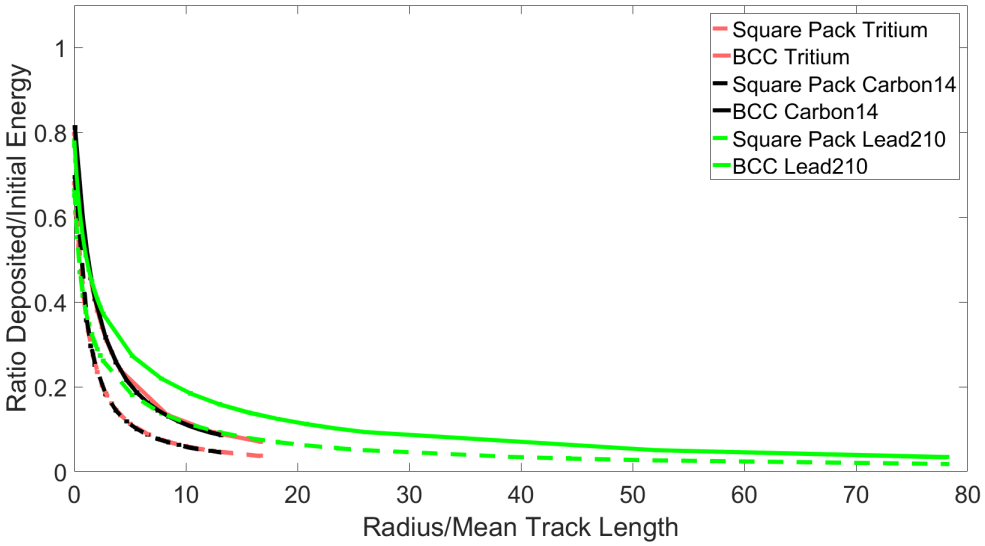


Figure A.5.9: Results of the Geant4 3D heterogeneous scintillator simulation using $^{3}$H, $^{14}$C & $^{210}$Pb. These results are normalised using the Mean Track Length.

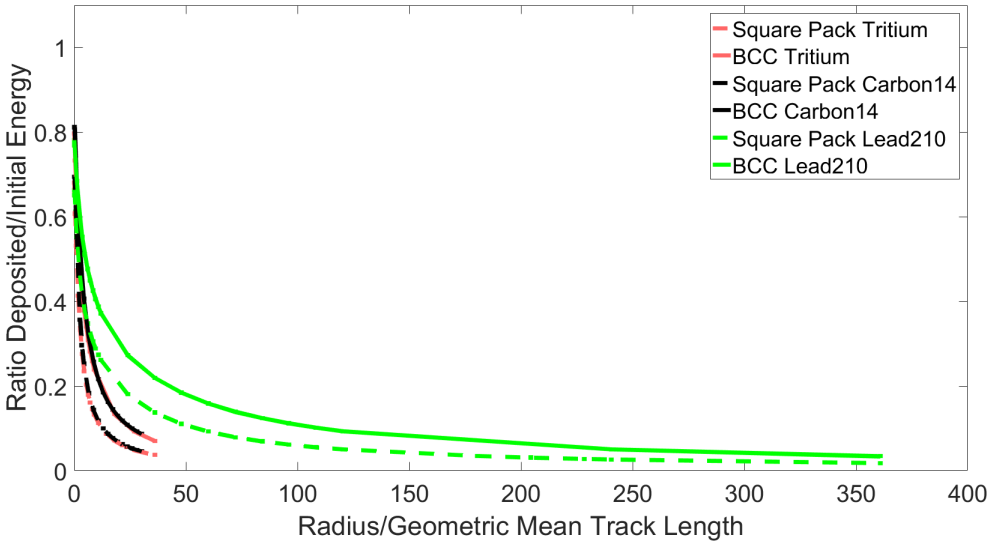


Figure A.5.10: Results of the Geant4 3D heterogeneous scintillator simulation using $^{3}$H, $^{14}$C & $^{210}$Pb. These results are normalised using the Geometric Mean Track Length.

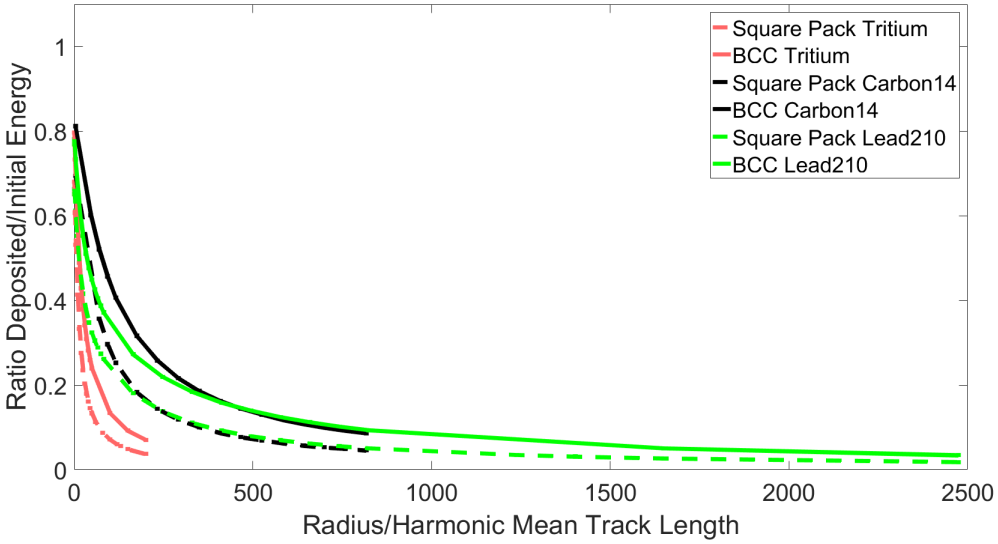


Figure A.5.11: Results of the Geant4 3D heterogeneous scintillator simulation using $^{3}$H, $^{14}$C & $^{210}$Pb. These results are normalised using the Harmonic Mean Track Length.

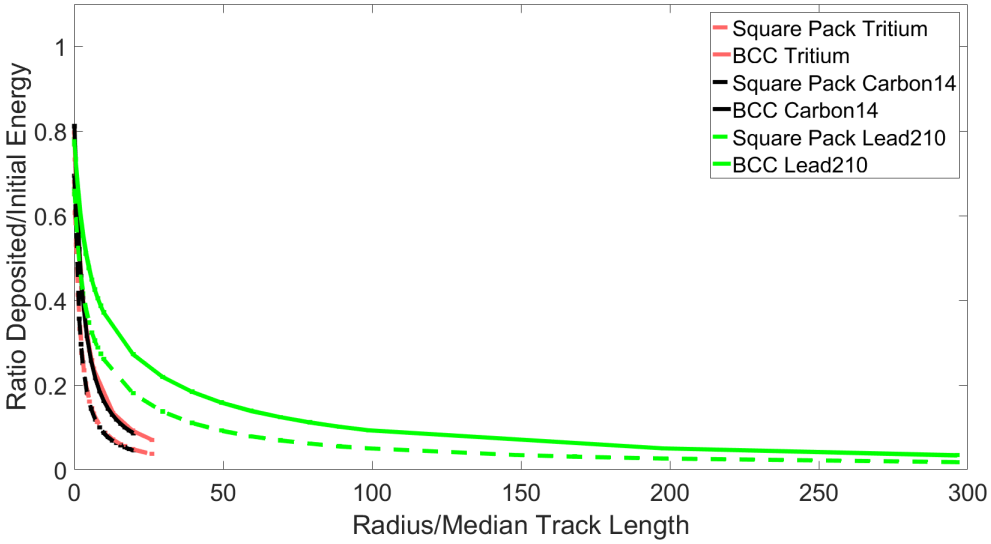


Figure A.5.12: Results of the Geant4 3D heterogeneous scintillator simulation using $^{3}$H, $^{14}$C & $^{210}$Pb. These results are normalised using the Median Track Length.

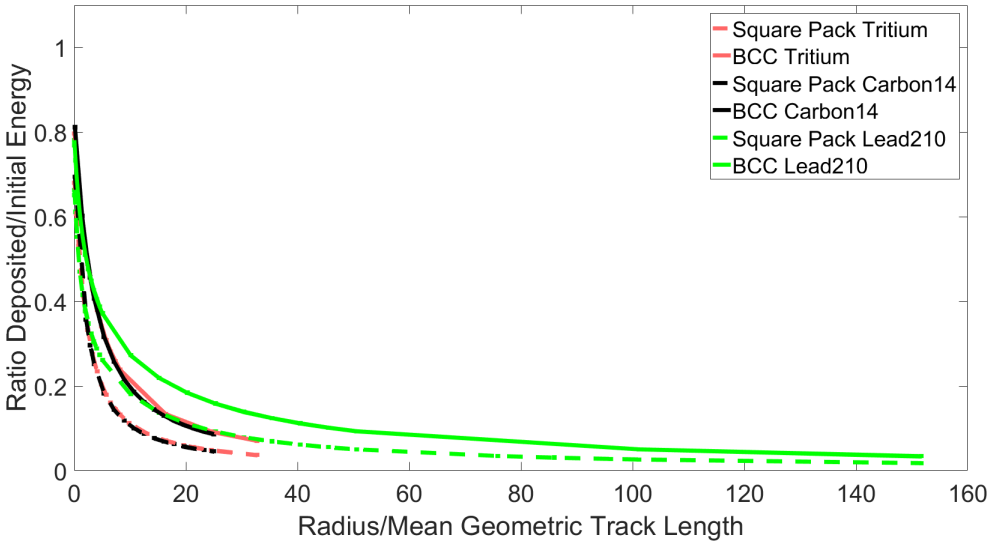


Figure A.5.13: Results of the Geant4 3D heterogeneous scintillator simulation using $^{3}$H, $^{14}$C & $^{210}$Pb. These results are normalised using the Mean Geometric Track Length.

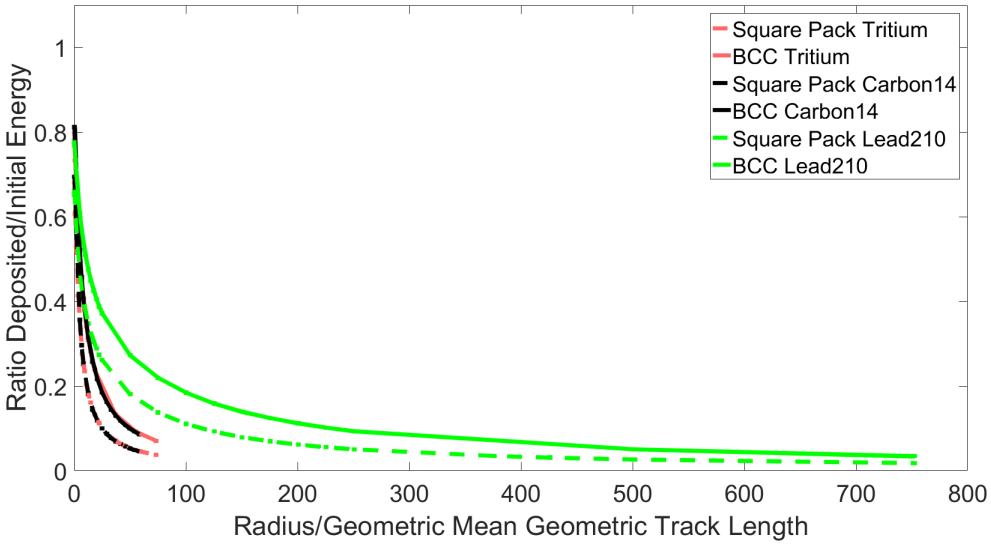


Figure A.5.14: Results of the Geant4 3D heterogeneous scintillator simulation using $^{3}$H, $^{14}$C & $^{210}$Pb. These results are normalised using the Geometric Mean Geometric Track Length.

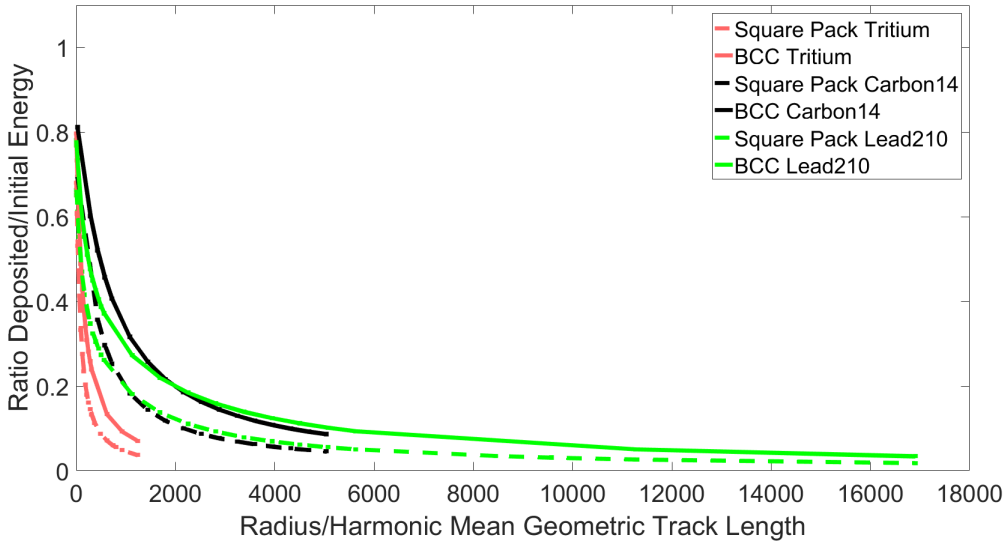


Figure A.5.15: Results of the Geant4 3D heterogeneous scintillator simulation using $^{3}$H, $^{14}$C & $^{210}$Pb. These results are normalised using the Harmonic Mean Geometric Track Length.

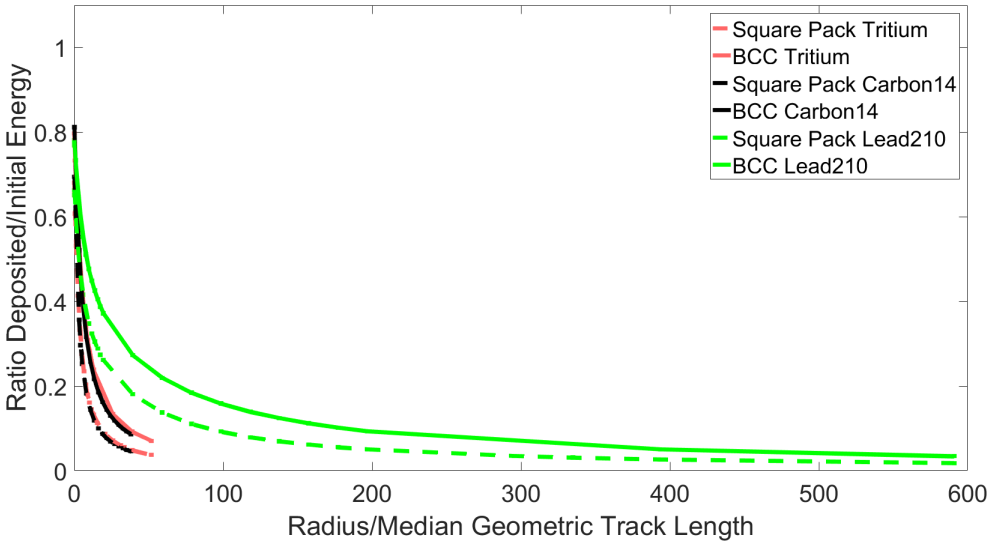


Figure A.5.16: Results of the Geant4 3D heterogeneous scintillator simulation using $^{3}$H, $^{14}$C & $^{210}$Pb. These results are normalised using the Median Geometric Track Length.

## A.6 Flow Cell Scintillator Fabrication

The scintillators for these experiments were manufactured as two sets of scintillator discs. The first as a set of three 4 mm thick perspex discs, 4 cm in diameter, with the gap between the layers as 8 mm. The second set was twelve polycarbonate discs of 1 mm thick, 4 cm in diameter and the gap between them as 1 mm. The $CaF_2$:Eu powder for both of these was made through the same process as Chapter 6.4. The process used to form the thin layer involved a thin layer of an acrylic adhesive EvoStik ExtruFix, a metallic grating was utilised through which the powder was deposited onto the disc, and repeated to cover both sides. The polycarbonate discs were further processed by the use of 3M Scotchbright 7447 handpad to enhance the optical transparency of each disc, the transparency was not measured.

## A.7 Transient Radioisotope

This section is taken verbatim from the article [211]. This theory is used in Chapter 6.8 for prediciting the flow rates of packed volumes, this theory is also used to underpin how to detect a transient radioisotope which is employed in Chapter 7.2.1.

Consider the scenario in Fig. A.7.1, whereby a detector comprised of a porous heterogeneous scintillator is being used to monitor the concentration of beta particle emitting radionuclides in an open channel, such as a river. At some past time, contaminated water was released into the channel. This contaminated water contains a concentration, $C_0$, of a beta particle emitting radionuclide such as tritium. The

contamination is assumed to flow as a plug of width, w, at a velocity, v. Note that this neglects issues such as dispersion, evaporation, decay etc. but the conclusions apply quite generally.

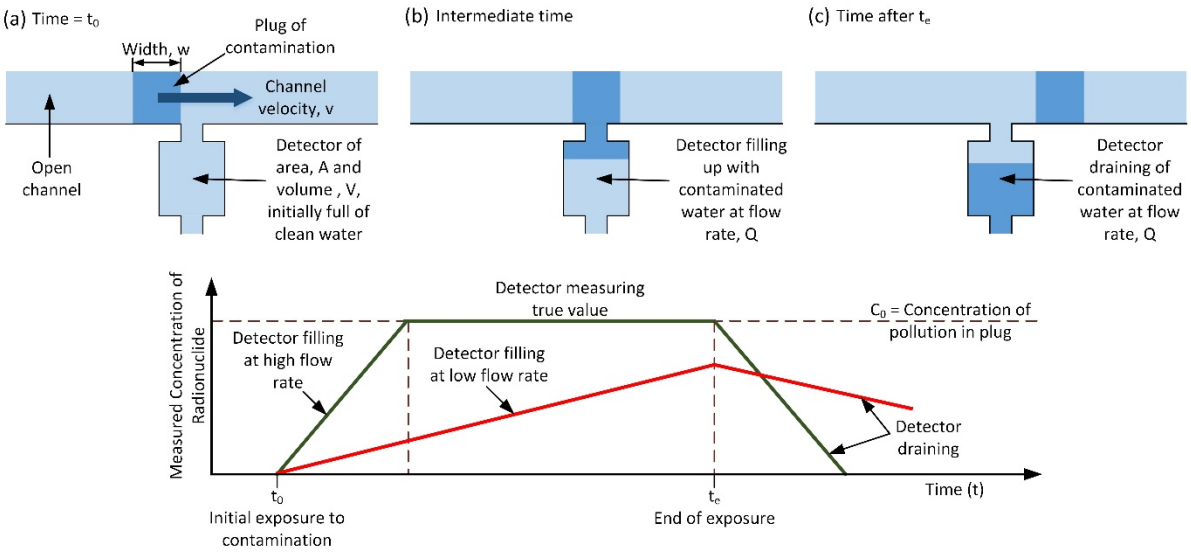


Figure A.7.1: "Top row depicts schematics of the fill level of a porous scintillator-based detector at various times, i.e. (a) before exposure, (b) during exposure where the detector is filling up with contaminated water and (c) after exposure where the detector is draining but still contains contaminated water. Bottom figure shows the effective concentration as measured by the detector at different times assuming both high and low flow rates though the detector." [211].

Naturally, what is desired is for the detector to measure the true concentration of the contaminated water. However, the detector is only exposed to the contamination for a finite time, $T_e$=$t_e$-$t_0$=w/v (assuming the length/diameter of inlets to be negligible) and the detector takes a finite time to fill, $t_f$=V/Q, where Q is the flow rate

through the porous scintillator, see Fig. A.7.1. If the flow rate into the flow cell is too slow, then it is possible that the detector may never read the true concentration of the contamination. This may be the case for 3D packed structures comprised of very small particles. The volume of contaminated water in the detector at a given time is:

$$V_t(t) = \begin{cases} if \quad t_f > T_e \quad Q \cdot (t - t_0) \quad for \quad t_0 < t \leq t_e \\ otherwise \quad Q \cdot (t - t_0) \quad for \quad t_0 < t \leq t_f \\ V \quad for \quad (t_0 + t_f) < t \leq t_f \\ V_t(t_e) - Q \cdot (t - t_e) \quad for \quad t > t_e \\ 0 \quad for \quad t < t_0 \quad and \quad t > (t_e + t_f) \end{cases} \tag{A.7.1}$$

The flow rate through the porous scintillator is given by the Carman-Kozeny equation [217, 218]:

$$\frac{dp}{dx} = -\frac{150\mu}{\Phi^2 D_p^2} \frac{(1-\epsilon)^2}{\epsilon^3} u \tag{A.7.2}$$

where dp/dx and u is the pressure gradient and mean flow velocity through the porous scintillator respectively, $\mu$ is the viscosity of the fluid, taken here to be effectively water so that $\mu = 1.002\,\mathrm{mPa\,s^{-1}}$, $\varepsilon$ is the scintillator porosity ($\varepsilon = 0.476$ for cubic packed spheres), $\Phi$ is the sphericity which equals 1 and $D_p$ is the mean scintillator particle diameter.

If $C_0$ $[\mathrm{mol\,L^{-1}}]$ is the concentration of the radionuclide in the contaminated water and the specific radioactivity is [81]:

$$a[Bq/g] = \frac{1.32 \times 10^{16}[mol^{-1}]}{T_{1/2}[year] \times m[gmol^{-1}]} \tag{A.7.3}$$

where $T_{1/2}$ is the half-life of the radionuclide and m is its mass number, the activity

measured by the detector as a function of time is:

$$A[Bq] = V_t(t)[L] \times C_0[molL^{-1}] \times m[gmol^{-1}] \times a[Bqg^{-1}] \tag{A.7.4}$$

As an example, consider a river following at $1\,\mathrm{m\,s^{-1}}$ contaminated by 0.1 nmol of tritiated water such that it forms a plug 100 m long (exposure time of $\mathrm{T}_e = 100\,\mathrm{s}$). The mass number and half-life of tritiated water is $22.0315\,\mathrm{g\,mol^{-1}}$ and 12.3 years respectively and so it has a specific activity of $4.87 \times 10^{13}\,\mathrm{Bq\,g^{-1}}$. At this concentration, the activity per volume will be $107.3\,\mathrm{kBq\,L^{-1}}$, which is at dangerous levels. Let the scintillator be 100 mm x 100 mm x 100 mm (V = 1 L) in size and comprised of cubic packed spherical particles of diameter 10 µm so that the maximum water volume in the scintillator is $\varepsilon.\mathrm{V} = 0.476\,\mathrm{L}$. Let the pump apply 10 kPa across the scintillator (a low pressure as not to cause loss of the scintillator material). In this case, by rearranging Eq. (A.7.2), the flow velocity through the scintillator can be found to be:

$$u = \frac{dp}{dx}\frac{D_p^2\epsilon^3}{150\mu(1-\epsilon)^2} = 2.94 \times 10^{-5} ms^{-1} \tag{A.7.5}$$

Multiplying this velocity by the cross-sectional area of the scintillator gives the flow rate. In this case $\mathrm{Q} = 0.29\,\mathrm{mL\,s^{-1}}$ and so filling time, $\mathrm{t}_f = 1618\,\mathrm{s}$. The filling of the flow cell and the monitoring of the activity within the flow cell will be continuous and simultaneous, as the experimenter will not know when the contamination will reach and leave the flow cell. In this scenario, the detector never completely fills up with contaminated water and so the maximum measured count rate would be 3.16 kCPS (1.62 kCPS average counts over $\mathrm{t_0}<\mathrm{t}<\mathrm{t_0}+\mathrm{t}_e+\mathrm{V}_t\ (\mathrm{t}_e)/\mathrm{Q}$) while the maximum possible expected total counts would be 51.08 kCPS (neglecting detection inefficiencies and

attenuation effects). Therefore, to the experimenter, the contamination would appear to have a triangular profile over 200 s with an average and peak concentration of 3.17 pmol and 6.19 pmol respectively, far from the constant 0.1 nmol concentration for 100 s that is expected. However, if the scintillator particles had a mean diameter of 100 µm the fill time would be much reduced ($t_f = 16.2$ s) so it would be completely filled by contaminated water. Therefore, the maximum possible measured count rate would be 51.08 kCPS as expected with an average count rate of 46.68 kCPS. The experimenter would therefore see a near constant contamination concentration of 0.1 nmol for 80 s with an average of 0.091 nmol over 120 s which is much closer to the actual value.

# Bibliography

[1] Dr. Gillian MacKinnon SUERC. Tritium in the aquatic environment. https://fukushima.jaea.go.jp/english/outline/pdf1410/4a-2_MacKinnon.pdf, 2017. [Online Accessed 03/11/2017].

[2] Annual discharge and monitoring reports. http://sustainability.sellafieldsites.com/environment/environment-page/annual-discharge-monitoring-reports/, 2014. [Online; Accessed 10 December 2014].

[3] Review of risks of tritium. https://www.gov.uk/government/uploads/system/uploads/attachment_data/file/335151/RCE-4_Advice_on_tritium.pdf, 2017. [Online Accessed 04/12/2017].

[4] radionuclide fact sheet: Tritium and the environment. http://www.irsn.fr/EN/Research/publications-documentation/radionuclides-sheets/environment/Documents/Tritium_UK.pdf, 9 August 2012. [Online Accessed 30/03/2018].

[5] Tritium fact sheet. https://hps.org/documents/tritium_fact_sheet.pdf, 2016. [Online Accessed 31/05/2016].

[6] A. A. Korsheninnikov, E. Yu. Nikolskii, E. A. Kuzmin, A. Ozawa, K. Morimoto, F. Tokanai, R. Kanungo, I. Tanihata, N. K. Timofeyuk, M. S. Golovkov, A. S. Fomichev, A. M. Rodin, M. L. Chelnokov, G. M. Ter-Akopian, W. Mittig, P. Roussel-Chomaz, H. Savajols, E. Pollacco, A. A. Ogloblin, and M. V. Zhukov. Experimental evidence for the existence of $^{7}$H and for a specific structure of $^{8}$He. Phys. Rev. Lett., 90:082501, Feb 2003.

[7] Yu. B. Gurov, D. V. Aleshkin, M. N. Behr, S. V. Lapushkin, P. V. Morokhov, V. A.. .. Pechkurov, N. O. Poroshin, V. G. Sandukovsky, M. V. Tel'kushev, B. A. Chernyshev, and T. D. Tschurenkova. Spectroscopy of superheavy hydrogen isotopes in stopped-pion absorption by nuclei. Physics of Atomic Nuclei, 68(3):491–497, Mar 2005.

[8] Table of isotopic masses and natural abundances. https://projects.ncsu.edu/ncsu/chemistry/msf/pdf/IsotopicMass_NaturalAbundance.pdf, 2015. [Online Accessed 14/04/2018].

[9] Human health fact sheet: Tritium (hydrogen-3). http://hpschapters.org/northcarolina/NSDS/tritium.pdf, 2001. [14/04/2018].

[10] M.L.E. Oliphant, P. Harteck, and Lord Rutherford. Transmutation effects observed with heavy hydrogen. Proceedings of the Royal Society A, 144:692–703, 1934.

[11] Luis W. Alvarez and Robert Cornog. Helium and hydrogen of mass 3. Physical Review, 56:613, 1939.

[12] Rainer Lässer. Tritium and Helium-3 in Metals. Springer-Verlag, Berlin, 2013. Springer Series in Materials Science 9.

[13] A.S. Eve. Rutherford. Cambridge University Press, Cambridge, 1939.

[14] H. Kragh. Rutherford, Radioactivity, and the Atomic Nucleus. ArXiv e-prints, February 2012.

[15] H3 table de radionucléides. http://www.nucleide.org/DDEP_WG/Nuclides/H-3_tables.pdf, 2007. [Online Accessed 03/11/2017].

[16] Beta decay of a tritium atom. http://frhewww.physik.uni-freiburg.de/SideBar/l5_Lectures/SS2011/Uebungen/UebungenLoesungen/Uebungen_07_SS2011-ExIV-HELM.pdf, 2017. [Online Accessed 03/11/2017].

[17] Rad toolbox v. 3.0.0. https://crpk.ornl.gov/software/, 2015. [Online Accessed 24/06/2015].

[18] IAEA. Tritium in the atmosphere. http://www-naweb.iaea.org/napc/ih/documents/global_cycle/vol%20II/cht_ii_05.pdf, 2017. [Online Accessed 03/11/2017].

[19] L.L. Newkirk. Calculation of low-energy neutron flux in the atmosphere by $s_n$ the method. Journal of Geophysical Research, 68:1825–1833, 1963.

[20] N. Paunescu, D. Galeriu, and N. Mocanu. Environmental tritium around a new can du nuclear power plant. Radioprotection, 37:1253–1258, 2002.

[21] Enhancements in the thorp reprocessing plant. https://www.iaea.org/inis/collection/NCLCollectionStore/_Public/32/033/32033963.pdf, 2005. [Online Accessed 05/03/2018].

[22] Pwr tritium issues. http://hps.ne.uiuc.edu/rets-remp/PastWorkshops/2008/Session%203%20-%20Greg%20Jones%20-%20Presentation.ppt, 2008. [Online Accessed 02/06/2018].

[23] Fundamental safety overview, volume 3: Environmental impact, chapter d: Potential environmental and health effects. http://www.epr-reactor.co.uk/ssmod/liblocal/docs/V3/Volume%203%20-%20Environmental%20Impact/3.D%20-%20Potential%20Environmental%20and%20Health%20Effects/3.D.7%20-%20Health%20effects/3.D.7.1%20-%20Introduction.pdf, 2007. [Online Accessed 02/06/2018].

[24] Yuri Kageyama phys.org. Japan prepares for release of tritium from fukushima plant. https://phys.org/news/2016-04-japan-tritium-fukushima.html, 2017. [Online Accessed 03/11/2017].

[25] J. Paatero, K. Haemeri, T. Jaakkola, M. Jantunen, J. Koivukoski, and R. Saxen. Airborne and deposited radioactivity from the chernobyl accident. a review of investigations in finland. Boreal Environment Research, 15:19–33, 2010.

[26] Vyacheslav Shestopalov. Chernobyl Disaster and Groundwater. A.A. Balkema Publisher, 2002.

[27] K. Rozanski, R. Gonfiantini, and L. Araguas-Araguas. Tritium in the global atmosphere: distribution patterns and recent trends. Journal of Physics G: Nuclear and Particle Physics, 17(S):S523, 1991.

[28] Frédérique Eyrolle, Loïc Ducros, Séverine Le Dizès, Karine Beaugelin-Seiller, Sabine Charmasson, Patrick Boyer, and Catherine Cossonnet. An updated review on tritium in the environment. Journal of Environmental Radioactivity, 181:128–137, 2018.

[29] Tritium in drinking water. `http://nuclearsafety.gc.ca/eng/resources/health/tritium/tritium-in-drinking-water.cfm`, 2009. [Online Accessed on 04/02/2015].

[30] John Hunt, Kinson Leonard, and Linda Hughes. Artificial radionuclides in the irish sea from sellafield: remobilisation revisited. Journal of Radiological Protection, 33(2):261, 2013.

[31] Monitoring our environment discharges and environmental monitoring annual report 2013. `http://sustainability.sellafieldsites.com/files/2013/05/2013-Annual-Report-Final-Low-Res.pdf`, 2013. [Online; Accessed 10 December 2014].

[32] B. Fievet, J. Pommier, C. Voiseux, P. Bailly du Bois, P. Laguionie, C. Cossonnet, and L. Solier. Transfer of tritium released into the marine environment by

french nuclear facilities bordering the english channel. Environmental Science and Technology, 47:6696–6703, 2013.

[33] C. Varlam, V. Patrascu, R.M. Margineanu, I. Faurescu, I. Vagner, D. Faurescu, and O.G. Duliu. Tritium activity concentration along the western shore of the black sea. Journal of Radioanalytical and Nuclear Chemistry, 298:1679–1683, 2013.

[34] M.A. Kulkova and A.V. Davidochkina. Tritium in the environment of gulf of finland. International Journal of Chemical Engineering and Applications, 2:8–11, 2011.

[35] Tritium: Health consequences. `https://www.nirs.org/wp-content/uploads/factsheets/tritiumbasicinfo.pdf`, 2008. [Online Accessed 30/03/2018].

[36] Z. Pietrzak-Flis, I. Radwan, and L. Indeka. Tritium in rabbits after ingestion of freeze-dried tritiated food and tritiated water. Radiation Research, 76:420–428, 1978.

[37] E. L. Etnier, C. C. Travis, and D. M. Hetrick. Metabolism of organically bound tritium in man. Radiation Research, 100:487–502, 1994.

[38] J. D. Harrison, A. Khursheed, and B. E. Lambert. Uncertainties in dose coefficients for intakes of tritiated water and organically bound forms of tritium by members of the public. Radiation Protection Dosimetry, 98:299–311, 2002.

[39] John Harrison. Doses and risks from tritiated water and environmental organically bound tritium. Journal of Radiological Protection, 29:335–349, 2009.

[40] Relative biological effectiveness of low-energy electrons and photons. https://www.epa.gov/sites/production/files/2015-05/documents/epa-rbe-report-11-04-2013.pdf, 2017. [Online Accessed 04/12/2017].

[41] Sources, effects and risks of ionizing radiation: Annex c- biological effects of selected internal emitters—tritium. http://www.unscear.org/docs/publications/2016/UNSCEAR_2016_Annex-C.pdf, 2017. [Online Accessed 06/12/2017].

[42] Health effects, dosimetry and radiological protection of tritium. http://nuclearsafety.gc.ca/pubs_catalogue/uploads/CNSC_Health_Effects_Eng-web.pdf, 2017. [Online Accessed 05/11/2017].

[43] Stochastic radiation effect. https://www.euronuclear.org/info/encyclopedia/s/stochastic-radiation-effect.htm, 2018. [Online Accessed 11/11/2018].

[44] Cocktails for liquid scintillation counting. http://www.perkinelmer.co.uk/lab-solutions/resources/docs/APP_Cocktails-for-Liquid-Scintillation-Counting-011940_01.pdf, 2017. [Online Accessed 06/11/2017].

[45] Msds for ultima gold. http://www.perkinelmer.com/Content/

MSDSDatabase/MSDS_6013329_Ultima_Gold_(GB).pdf, 2016. [Online Accessed 20/06/2016].

[46] K.S. Shah, M.R. Squillante, and G. Entine. $Hgi_2$ low energy beta particle detector. IEEE Transactions on Nuclear Science, 37:152–154, 1990.

[47] Hygroscopic: Definition. http://www.ilpi.com/msds/ref/hygroscopic.html, 2016. [Online Accessed 15/03/2018].

[48] C.D. Bass, E.J. Beise, H. Breuer, C.R. Heimbach, T.J. Langford, and J.S. Nico. Characterization of a 6li-loaded liquid organic scintillator for fast neutron spectrometry and thermal neutron detection. Applied Radiation and Isotopes, 77:130 – 138, 2013.

[49] Alexander S. Crowell. Cross-Section Measurements of Star Configurations in Neutron-Deuteron Breakup at 16.0 MeV. PhD thesis, Department of Physics, Duke University, 2001. http://www.tunl.duke.edu/~gsheu/Theses/PhD/Crowell_2001.pdf, [Online Accessed 11/11/2018].

[50] Zoltán Köllő. A plastic scintillator-based activity monitor for tritated water in the gbq/l range. Nuclear Instruments and Methods in Physics Research Section A, 798:24–29, 2015.

[51] Zoltán Köllő. Studies on a plastic scintillator detector for activity measurement of tritiated water. PhD thesis, Karlsruher Institut für Technologie (KIT), July 2015. https://publikationen.bibliothek.kit.edu/1000049424/3694161.

[52] K.G. Falter and M.L. Bauer. Tritium monitoring for near ambient measurements. IEEE Transactions on Nuclear Science, 39:962–965, 1991.

[53] T. Uda, T. Kawano, M. Tanaka, S. Tomatsuri, and T. Ito. Detection efficiency of plastic scintillator for gaseous tritium sampling and measurement system. Fusion Engineering and Design, 85:1474–1478, 2010.

[54] Enhancing the safety of nuclear decommissioning and engineering. https://cdn.qumucloud.com/origin/lr.kulu.net/9c7259e0-bfa2-11e4-9af8-6cb443312e52/h6NVzBA7tqh/canonical.pdf?stime=20180706125413&etime=20180707125513&hash=02dedd9668afd086594f8&oauth_token=cb0a48ca28f5b1ddceb513c1aafce384&oauth_timestamp=1530881653&oauth_consumer_key=cdn&oauth_signature_method=HMAC-SHA1&oauth_nonce=4456286971914326&oauth_version=1.0&oauth_signature=EbCTiEAfNLvhYbPjKUqGBPLGqMM%3D, 2014. [Online Accessed 06/07/2018].

[55] Nanodot2: Nanomaterials for the radiometric detection of tritium. http://gtr.ukri.org/projects?ref=NE%2FN017293%2F1, 2016. [Online Accessed 06/07/2018].

[56] Nanodot+: Nanomaterials for the radiometric detection of tritium - placement with users. http://gtr.ukri.org/projects?ref=NE%2FR007195%2F1, 2017. [Online Accessed 06/07/2018].

[57] M.J. Rudin, W.M. Richardson, P.G. Dumont, and W.H. Johnson. In-situ mea-

surement of transuranics using a calcium fluoride scintillation detection system. Journal of Radiochemical and Nuclear Chemistry, 248:445–448, 2001.

[58] A.A. Kozlov, B.M. Shapiro, M.Yu. Shrom, S.V. Bryzgalov, N.D. Betenekov, L.V. Viktorov, E.I. Denisov, A.Yu. Kuznetsov, and B.V. Shul'gin. Caf2-eu single-crystal scintillation blocks for detecting -radiation. Atomic Energy - AT ENERGY-ENGL TR, 76:191–194, 3 1994.

[59] K. Shirahashi, G. Izawa, Y. Murano, Y. Muramastu, and K. Yoshihara. Radio-liquid chromatogrphy for tritium labelled organic compounds using caf2/eu/ scintillator. Journal of Radioanalytical and Nuclear Chemistry, 86:1–9, 1984.

[60] T.A. DeVol and R.A. Fjeld. Development of an on-line scintillation flow-cell detection system with pulse shape discrimination for quantification of actinides. IEEE Transactions on Nuclear Science, 42:959–963, 1995.

[61] T.A. DeVol, M.E. Keillor, and L.W. Burggraf. Influence of radionuclide adsorption on detection efficiency and energy resolution for flow-cell radiation detectors. IEEE Transactions on Nuclear Science, 43:1310–1315, 1996.

[62] J.R. DeVore and M.A. Buckner. Tritium monitoring techniques. Technical report, Oak Ridge National Laboratory, 1996. [Online Accessed 20/06/2018].

[63] A.N. Singh, M. Ratnakaran, and K.G. Vohra. An on-line tritium-in-water monitor. Nuclear Instruments and Methods in Physics Research Section A: Accelerators, Spectrometers, Detectors and Associated Equipment, 236(1):159 – 164, 1985.

[64] T. Kawano, T. Uda, T. Yamamoto, and H. Ohashi. Tritium water monitoring system based on caf2 flow-cell detector. Fusion Science and Technology, 60:952–955, 2011.

[65] T. Kawano, H. Ohashi, Y. Hamada, and E. Jamsranjav. Shielding effect on tritium water monitoring system based on caf2 flow-cell detector. Nuclear Science And Techniques, 25:S010401–3, 2014.

[66] T. Kawano, H. Ohashi, Y. Hamada, and E. Jamsranjav. Comparative testing of various flow-cell detectors fabricated using caf2 solid scintillator. Fusion Science and Technology, 67:404–407, 2015.

[67] Marvin J Weber. Inorganic scintillators: today and tomorrow. Journal of Luminescence, 100(1):35 – 45, 2002.

[68] Handling and care of crystal scintillation detectors. `https://www.crystals.saint-gobain.com/sites/imdf.crystals.com/files/documents/handling-and-care-of-crystal-scintillation-detectors_70413.pdf`, 2016. [Online Accessed 02/04/2018].

[69] Yso(ce) scintillation crystal. `https://www.x-zlab.com/product/yso-scintillation-crystal/`, 2017. [Online Accessed 11/10/2017].

[70] Yag(ce) scintillation crystal. `https://www.x-zlab.com/product/yag-scintillation-crystal/`, 2017. [Online Accessed 11/10/2017].

[71] Yap(ce) scintillation crystal. `https://www.x-zlab.com/product/yap-scintillation-crystal/`, 2017. [Online Accessed 11/10/2017].

[72] Csi(tl)- caesium iodide (thallium). http://www.advatech-uk.co.uk/csi_tl.html, 2017. [Online Accessed 11/10/2017].

[73] Csi(tl) scintillation crystal. https://www.x-zlab.com/product/csi-scintillation-crystal/, 2017. [Online Accessed 11/10/2017].

[74] General purpose plastic scintillator ej-200, ej-204, ej-208, ej-212. http://www.eljentechnology.com/images/products/data_sheets/EJ-200_EJ-204_EJ-208_EJ-212.pdf, 2017. [Online Accessed 10/10/2017].

[75] D. Kulp. Ionizing Radiation Detectors. Springer New York, New York, 2012.

[76] Bgo bismuth germanate scintillation material. https://www.crystals.saint-gobain.com/sites/imdf.crystals.com/files/documents/bgo-material-data-sheet_69763.pdf, 2016. [Online Accessed 02/04/2018].

[77] Baf2 barium fluoride. https://www.crystals.saint-gobain.com/products/baf2-barium-fluoride, 2018. [Online Accessed 02/04/2018].

[78] Cef3 - cerium fuoride. http://www.advatech-uk.co.uk/cef3.html, 2018. [Online Accessed 02/04/2018].

[79] General properties of pbwo4 scintillator. http://www.epic-crystal.com/shop_reviews/pbwo4-scintillator/, 2018. [Online Accessed 02/04/2018].

[80] J.Menefee, C.F. Swinehart, and E.W. O'Dell. Calcium fluoride as an x-ray and charged particle detector. IEEE Transations on Nuclear Science, 13:720–724, 1966.

[81] G.F. Knoll. Radiation Detection and Measurement. Wiley, 2nd edition, 1989.

[82] B.V. Shul'gin, Buzmakova, S.I., L.V. Viktorov, A.L. Krymov, V.L. Petrov, S.V. Podurovskii, A.A. Kozlov, B.M. Shapiro, M.Yu. Shrom, A.I. Nepomnyashchikh, P.V. Figura, and V.M. Lakhov. Scintillation detectors working with caf2-eu single crystals. Atomic Energy, 75:534–538, 1993.

[83] Radiation detection materials cebr3 sri2:eu caf2:eu baf2. `http://www.hellma-materials.com/html/seiten/output_adb_file.php?id=63`, 2015. [Online Accessed 25/02/2015].

[84] Caf2(eu) scintillation crystal. `https://www.x-zlab.com/product/caf2-scintillation-crystal/`, 2017. [Online Accessed 11/10/2017].

[85] Csi(ti) scintillator. `http://www.epic-crystal.com/shop_reviews/csitl-scintillator/`, 2017. [Online Accessed 11/10/2017].

[86] T.A. DeVol, S.B. Chotoo, and R.A. Fjeld. Evaluation of granulated bgo, gso:ce, yag:ce, caf2:eu and zns:ag for alpha/beta pulse shape discrimination in a flow cell radiation detector. Nuclear Instruments and Methods in Physics Research A: Accelerators, Spectrometers, Detectors and Associated Equipment, 425:228–231, 1999.

[87] Sam Beddar and Luc Beaulieu. Scintillation Dosimetry. CRC Press, 2016.

[88] C. Plettnor, G. Pausch, F. Scherwinski, C.M. Herbach, R. Lentering, Y. Kong, K. Romer, J. Stein, T. Szczesniak, M. Grodzicka, J. Iwanowska, and M. Moszyn-

ski. Caf2(eu): An old scintillator revisited. Journal of Instrumentation, 8:236–242, 2013.

[89] H. Nagayoshi, S. Nishimura, and K. Terashima. Optical properties of eu doped caf2 crystal for solar cell application. Conference Record of the 2006 IEEE 4th World Conference on Photovoltaic Energy Conversion, 1:150–153, 2006.

[90] P.A. Rodnyi. Physical Processes in Inorganic Scintillators, volume 14. CRC Press, 1997.

[91] Wahyu Setyawan, Romain M. Gaume, Stephanie Lam, Robert S. Feigelson, and Stefano Curtarolo. High-throughput combinatorial database of electronic band structures for inorganic scintillator materials. ACS Combinatorial Science, 13(4):382–390, 2011. PMID: 21644557.

[92] M.J. Weber. Scintillation: mechanisms and new crystals. Nuclear Instruments and Methods in Physics Research Section A: Accelerators, Spectrometers, Detectors and Associated Equipment, 527(1–2):9 – 14, 2004. Proceedings of the 2nd International Conference on Imaging Technologies in Biomedical Sciences.

[93] A. Chaudhry, R. Boutchko, S. Chourou, G. Zhang, N. Grønbech-Jensen, and A. Canning. First-principles study of luminescence in $eu^{2+}$-doped inorganic scintillators. Phys. Rev. B, 89:155105, Apr 2014.

[94] G. Bizarri. Scintillation mechanisms of inorganic materials: From crystal characteristics to scintillation properties. Journal of Crystal Growth, 312(8):1213 – 1215, 2010. The 17th American Conference on Crystal Growth and Epitaxy/The

14th {US} Biennial Workshop on Organometallic Vapor Phase Epitaxy/The 6th International Workshop on Modeling in Crystal Growth.

[95] J.Y Yeom, H Takahashi, T Ishitsu, M Nakazawa, and H Murayama. Development of a multi-channel waveform sampling asic for animal pet with doi information. Nuclear Instruments and Methods in Physics Research Section A: Accelerators, Spectrometers, Detectors and Associated Equipment, 525(1):221 – 224, 2004. Proceedings of the International Conference on Imaging Techniques in Subatomic Physics, Astrophysics, Medicine, Biology and Industry.

[96] Solid scintillator counting compositions. https://patents.google.com/patent/US4692266A/en, 1987. US Grant: US4692266A, [Online Accessed 07/05/2018].

[97] Scintillation proximity assay. https://patents.google.com/patent/US4271139A/en, 1981. US Grant: US4271139A, [Online Accessed 07/05/2018].

[98] Scintillator including a scintillator particulate and a polymer matrix. https://patents.google.com/patent/US8633449B2/en, 2014. US Grant: US8633449B2, [Online Accessed 07/05/2018].

[99] Neutron detector using neutron absorbing scintillating particulates in plastic. https://patents.google.com/patent/US20050135535A1/en, 2005. US Application: US20050135535A1, [Online Accessed 07/05/2018].

[100] Distributed phosphor scintillator structures. https://patents.google.com/

patent/US4362946A/en, 1982. US Grant: US4362946A, [Online Accessed 07/05/2018].

[101] John Betteley Birks. The Theory and Pratice of Scintillation Counting: International Series of Monographs in Electronics and Instrumentation. Pergamon Press, 2013.

[102] C. Dujardin, D. Amans, A. Belsky, F. Chaput, G. Ledoux, and A. Pillonnet. Luminescence and scintillation properties at the nanoscale. IEEE Transactions On Nuclear Science, 57:1348–1354, 2010.

[103] N.V. Klassen, V.N. Kurlov, S.N. Rossolenko, O.A. Krivko, A.D. Orlov, and S.Z. Shmurak. Scintillation fibers and nanoscintillators for improving the spatial, spectrometric, and time resolution of radiation detectors. Bulletin of the Russian Academy of Sciences: Physics, 73:1369–1373, 2009.

[104] Edward A. McKigney, Rico E. Del Sesto, Luiz G. Jacobsohn, Peter A. Santi, Ross E. Muenchausen, Kevin C. Ott, T. Mark McCleskey, Bryan L. Bennett, James F. Smith, and D. Wayne Cooke. Nanocomposite scintillators for radiation detection and nuclear spectroscopy. Nuclear Instruments and Method in Physics Research Section A: Accelerators, Spectrometers, Detectors and Associated Equipment, 579:15–18, 2007.

[105] L.G. Jacobsohn, C.L. McPherson, K.B. Sprinkle, E.G. Yukihara, T.A. DeVol, and J. Ballato. Scintillation of rare earth doped fluoride nanoparticles. Applied Physics Letters, 99:113111, 2011.

[106] P.H. Holloway, M. Davidson, and L.G. Jacobsohn. Strategy for enhanced light output from luminescent nanoparticles. www.dtic.mil/cgi-bin/GetTRDoc?Location=U2&doc=GetTRDoc.pdf&AD=ADA582679. [Online Accessed on 26 January 2015].

[107] F. Esfandi and S. Saramad. Simulation, optimization and testing of a novel high spatial resolution x-ray imager based on zinc oxide nanowires in anodic aluminium oxide membrane using geant4. Journal of Instrumentation, 10(07):P07019, 2015.

[108] P. Kleimann, J. Linnros, C. Fröjdh, and C.S. Petersson. An x-ray imaging pixel detector based on scintillator filled pores in a silicon matrix. Nuclear Instruments and Methods in Physics Research Section A: Accelerators, Spectrometers, Detectors and Associated Equipment, 460(1):15 – 19, 2001. Proc. 1st Int. Workshop on Radiation Imaging Detectors.

[109] Ali Taheri, Shahyar Saramad, Samira Ghalenoi, and Saeed Setayeshi. Fabrication, testing and simulation of a high spatial resolution alpha-particle imager based on zno nanowires in a polycarbonate nanoporous membrane. The European Physical Journal C, 73(12):2649, Nov 2013.

[110] http://www.dtic.mil/dtic/tr/fulltext/u2/a289313.pdf, 1994. [Online Accessed 24/01/2018].

[111] M. E. Keillor and L. W. Burggraf. Detecting alpha radiation by scintillation in

porous materials. IEEE Transactions on Nuclear Science, 44(5):1741–1746, Oct 1997.

[112] Harley Ross. Liquid scintillation counting and organic scintillators. In Harley Ross, John E. Noakes, and Jim D. Spaulding, editors, Liquid Scintillation Counting and Organic Scintillators, chapter 17, pages 195–211. Lewis Publishers Inc., 121 South Main Street, Chelsea, Michigan 48118, 1991.

[113] H. Tan and T.A. DeVol. Monte carlo modeling of heterogeneous scintillation flow-cell detectors. Nuclear Instruments and Methods in Physics Research Section A: Accelerators, Spectrometers, Detectors and Associated Equipment, 515:624–633, 2003.

[114] Geant4 virtual machine. `http://geant4.in2p3.fr/spip.php?rubrique8&lang=en`, 2017. [Online Accessed 30/11/2017].

[115] S. Monk, B.A. Shippen, B.R. Colling, D. Cheneler, H. al Hamrashdi, and T. Alton. A comparison of mcnp6-1.0 and geant 4-10.1 when evaluating the neutron output of a complex real world nuclear environment: The thermal neutron facility at the tri universities meson facility. Nuclear Instruments and Methods in Physics Research Section B: Beam Interactions with Materials and Atoms, 399:48–61, 2017.

[116] K. Abe, J. Amey, C. Andreopoulos, L. Anthony, M. Antonova, S. Aoki, A. Ariga, Y. Ashida, S. Ban, M. Barbi, G. J. Barker, G. Barr, C. Barry, M. Batkiewicz, V. Berardi, S. Berkman, S. Bhadra, S. Bienstock, A. Blondel,

S. Bolognesi, S. Bordoni, B. Bourguille, S. B. Boyd, D. Brailsford, A. Bravar, C. Bronner, M. Buizza Avanzini, J. Calcutt, R. G. Calland, T. Campbell, S. Cao, S. L. Cartwright, M. G. Catanesi, A. Cervera, A. Chappell, C. Checchia, D. Cherdack, N. Chikuma, G. Christodoulou, J. Coleman, G. Collazuol, D. Coplowe, A. Cudd, A. Dabrowska, G. De Rosa, T. Dealtry, P. F. Denner, S. R. Dennis, C. Densham, F. Di Lodovico, S. Dolan, O. Drapier, K. E. Duffy, J. Dumarchez, P. Dunne, S. Emery-Schrenk, A. Ereditato, T. Feusels, A. J. Finch, G. A. Fiorentini, G. Fiorillo, C. Francois, M. Friend, Y. Fujii, D. Fukuda, Y. Fukuda, A. Garcia, C. Giganti, F. Gizzarelli, T. Golan, M. Gonin, D. R. Hadley, L. Haegel, J. T. Haigh, D. Hansen, J. Harada, M. Hartz, T. Hasegawa, N. C. Hastings, T. Hayashino, Y. Hayato, A. Hillairet, T. Hiraki, A. Hiramoto, S. Hirota, M. Hogan, J. Holeczek, F. Hosomi, K. Huang, A. K. Ichikawa, M. Ikeda, J. Imber, J. Insler, R. A. Intonti, T. Ishida, T. Ishii, E. Iwai, K. Iwamoto, A. Izmaylov, B. Jamieson, M. Jiang, S. Johnson, P. Jonsson, C. K. Jung, M. Kabirnezhad, A. C. Kaboth, T. Kajita, H. Kakuno, J. Kameda, D. Karlen, T. Katori, E. Kearns, M. Khabibullin, A. Khotjantsev, H. Kim, J. Kim, S. King, J. Kisiel, A. Knight, A. Knox, T. Kobayashi, L. Koch, T. Koga, P. P. Koller, A. Konaka, L. L. Kormos, Y. Koshio, K. Kowalik, Y. Kudenko, R. Kurjata, T. Kutter, J. Lagoda, I. Lamont, M. Lamoureux, P. Lasorak, M. Laveder, M. Lawe, M. Licciardi, T. Lindner, Z. J. Liptak, R. P. Litchfield, X. Li, A. Longhin, J. P. Lopez, T. Lou, L. Ludovici, X. Lu, L. Magaletti, K. Mahn, M. Malek, S. Manly, L. Maret, A. D. Marino, J. F. Martin, P. Martins, S. Martynenko, T. Maruyama, V. Matveev, K. Mavrokoridis, W. Y.

Ma, E. Mazzucato, M. McCarthy, N. McCauley, K. S. McFarland, C. McGrew, A. Mefodiev, C. Metelko, M. Mezzetto, A. Minamino, O. Mineev, S. Mine, A. Missert, M. Miura, S. Moriyama, J. Morrison, Th. A. Mueller, T. Nakadaira, M. Nakahata, K. G. Nakamura, K. Nakamura, K. D. Nakamura, Y. Nakanishi, S. Nakayama, T. Nakaya, K. Nakayoshi, C. Nantais, C. Nielsen, K. Nishikawa, Y. Nishimura, P. Novella, J. Nowak, H. M. O'Keeffe, K. Okumura, T. Okusawa, W. Oryszczak, S. M. Oser, T. Ovsyannikova, R. A. Owen, Y. Oyama, V. Palladino, J. L. Palomino, V. Paolone, N. D. Patel, P. Paudyal, M. Pavin, D. Payne, Y. Petrov, L. Pickering, E. S. Pinzon Guerra, C. Pistillo, B. Popov, M. Posiadala-Zezula, J.-M. Poutissou, A. Pritchard, P. Przewlocki, B. Quilain, T. Radermacher, E. Radicioni, P. N. Ratoff, M. A. Rayner, E. Reinherz-Aronis, C. Riccio, E. Rondio, B. Rossi, S. Roth, A. C. Ruggeri, A. Rychter, K. Sakashita, F. Sánchez, S. Sasaki, E. Scantamburlo, K. Scholberg, J. Schwehr, M. Scott, Y. Seiya, T. Sekiguchi, H. Sekiya, D. Sgalaberna, R. Shah, A. Shaikhiev, F. Shaker, D. Shaw, M. Shiozawa, T. Shirahige, M. Smy, J. T. Sobczyk, H. Sobel, J. Steinmann, T. Stewart, P. Stowell, Y. Suda, S. Suvorov, A. Suzuki, S. Y. Suzuki, Y. Suzuki, R. Tacik, M. Tada, A. Takeda, Y. Takeuchi, R. Tamura, H. K. Tanaka, H. A. Tanaka, T. Thakore, L. F. Thompson, S. Tobayama, W. Toki, T. Tomura, T. Tsukamoto, M. Tzanov, W. Uno, M. Vagins, Z. Vallari, G. Vasseur, C. Vilela, T. Vladisavljevic, T. Wachala, J. Walker, C. W. Walter, Y. Wang, D. Wark, M. O. Wascko, A. Weber, R. Wendell, M. J. Wilking, C. Wilkinson, J. R. Wilson, R. J. Wilson, C. Wret, Y. Yamada, K. Yamamoto, S. Yamasu, C. Yanagisawa, T. Yano, S. Yen, N. Yershov, M. Yokoyama, T. Yuan,

M. Yu, A. Zalewska, J. Zalipska, L. Zambelli, K. Zaremba, M. Ziembicki, E. D. Zimmerman, and M. Zito. First measurement of the $\nu_\mu$ charged-current cross section on a water target without pions in the final state. Phys. Rev. D, 97:012001, Jan 2018.

[117] CERN. Geant4 physics reference manual. `http://geant4.web.cern.ch/geant4/UserDocumentation/UsersGuides/PhysicsReferenceManual/fo/PhysicsReferenceManual.pdf`, 2017. [Online Accessed 12/10/2017].

[118] L. Pandola, C. Andenna, and B. Caccia. Validation of the geant4 simulation of bremsstrahlung from thick targets below 3 mev. Nuclear Instruments and Methods in Physics Research Section B: Beam Interactions with Materials and Atoms, 350:41–48, 2015.

[119] G.A.P. Cirrone, G. Cuttone, F. Di Rosa, L. Pandola, F. Romano, and Q. Zhang. Validation of the geant4 electromagnetic photon cross-sections for elements and compounds. Nuclear Instruments and Methods in Physics Research Section A: Accelerators, Spectrometers, Detectors and Associated Equipment, 618:315–322, 2010.

[120] G.O. Depaola and M.L. Iparraguirre. Angular distribution for the electron recoil in pair production by linearly polarized - rays on electrons. Nuclear Instruments and Methods in Physics Research Section A: Accelerators, Spectrometers, Detectors and Associated Equipment, 611:84–92, 2009.

[121] G. O. Depaola and G. N. Leguizamon. Measuring polarization in the x-ray

range: simulation for the impact gas mixture and pressure in gaseous detectors. X-Ray Spectrometry, 38(6):519–525, 2009.

[122] G.O. Depaola. New monte carlo method for compton and rayleigh scattering by polarized gamma rays. Nuclear Instruments and Methods in Physics Research Section A: Accelerators, Spectrometers, Detectors and Associated Equipment, 512:619–630, 2003.

[123] Dan Xu Zhong He and Feng Zhang. Detection of gamma ray polarization using a 3-d position-sensitive cdznte detector. IEEE TRANSACTIONS ON NUCLEAR SCIENCE, 52:1160–1164, 2005.

[124] CERN. Livermore low-energy electromagnetic models. `https://twiki.cern.ch/twiki/bin/view/Geant4/LoweMigratedLivermore`, 2017. [Online Accessed 13/10/2017].

[125] Physics reference manual: Low energy livermore model. `http://geant4.web.cern.ch/geant4/UserDocumentation/UsersGuides/PhysicsReferenceManual/html/electromagnetic/introduction/livermore.html`, 2018. [Online Accessed 08/03/2018].

[126] `http://hyperphysics.phy-astr.gsu.edu/hbase/Forces/funfor.html`, 2018. [Online Accessed 25/02/2018].

[127] `https://www.physi.uni-heidelberg.de/~reygers/seminars/2015/nobel_prizes_in_particle_physics/talks/schweiger_structure_of_nuclei.pdf`, 2018. [Online Accessed 25/02/2018].

[128] http://hyperphysics.phy-astr.gsu.edu/hbase/Nuclear/elescat.html, 2018. [Online Accessed 25/02/2018].

[129] http://www.microscopy.ethz.ch/downloads/Interactions.pdf, 2018. [Online Accessed 25/02/2018].

[130] https://www.jeol.co.jp/en/applications/detail/465.html, 2018. [Online Accessed 25/02/2018].

[131] http://hyperphysics.phy-astr.gsu.edu/hbase/Atomic/auger.html, 2018. [Online Accessed 26/02/2018].

[132] https://www.nucleonica.com/wiki/images/7/74/MTufan_Interaction_of_Electrons_with_Matter.pdf, 2018. [Online Accessed 26/02/2018].

[133] http://holbert.faculty.asu.edu/eee460/IonizationRange.pdf, 2018. [Online Accessed 26/02/2018].

[134] Günter H. Zschornack. Handbook of X-Ray Data. Springer-Verlag Berlin Heidelberg, 1 edition, 2007.

[135] https://ocw.mit.edu/courses/nuclear-engineering/22-105-electromagnetic-interactions-fall-2005/readings/chap7.pdf, 2018. [Online Accessed 26/02/2018].

[136] Passage of particles through matter. http://pdg.lbl.gov/2011/reviews/rpp2011-rev-passage-particles-matter.pdf, 2018. [Online Accessed 26/02/2018].

[137] Eva Tihlaříková, Vilém Neděla, and Makoto Shiojiri. In situ study of live specimens in an environmental scanning electron microscope. Microscopy and Microanalysis, 19:914–918, 2013.

[138] Electron-beam lithography training: Proximity effect. https://nano.yale.edu/proximity-effect-page-2, 2018. [Online Accessed 10/03/2018].

[139] Stefaan Tavernier. Experimental Techniques in Nuclear and Particle Physics. Springer-Verlag Berlin Heidelberg, 1 edition, 2010.

[140] Interaction of electrons with matter. http://moreira.tamu.edu/BAEN625/TOC_files/chapt4b08.pdf, 2018. [Online Accessed 16/01/2018].

[141] http://geant4-userdoc.web.cern.ch/geant4-userdoc/UsersGuides/ForApplicationDeveloper/html/Appendix/materialNames.html, 2018. [Online Accessed 13/02/2018].

[142] Photomultiplier tubes: Basics and applications. https://www.hamamatsu.com/resources/pdf/etd/PMT_handbook_v3aE.pdf, 2018. [Online Accessed 28/02/2018].

[143] Sensl. Introduction to silicon photomultiplier. http://www.sensl.com/downloads/ds/TN%20-%20Intro%20to%20SPM%20Tech.pdf, 2015. [Online Accessed 19/02/2015].

[144] Avalanche photodiodes. https://www.rp-photonics.com/avalanche_photodiodes.html, 2018. [Online Accessed 28/02/2018].

[145] Capturing the image ccd and cmos sensors. http://cpn.canon-europe.com/content/education/infobank/capturing_the_image/ccd_and_cmos_sensors.do, 2018. [Online Accessed 28/02/2018].

[146] What is a ccd? http://www.specinst.com/What_Is_A_CCD.html, 2018. [Online Accessed 28/02/2018].

[147] Sensl. C-series datasheet. http://sensl.com/downloads/ds/DS-MicroCseries.pdf, 2015. [Online Accessed 11/03/2015].

[148] Microfc-60035-smt. https://sensl.com/estore/microfc-60035-smt/, 2018. [Online Accessed 04/06/2018].

[149] Table of nuclides. http://www.kayelaby.npl.co.uk/atomic_and_nuclear_physics/4_6/4_6_1_part02_020_029.html#Co, 2018. [Online Accessed 02/03/2018].

[150] Co60 table de radionucléides. http://www.nucleide.org/DDEP_WG/Nuclides/Co-60_tables.pdf, 2010. [Online Accessed 04/06/2018].

[151] Tilly Alton, Stephen Monk, and David Cheneler. Beta particle energy spectra shift due to self-attenuation effects in environmental sources. Journal of Nuclear Engineering and Technology, 49:1483–1488, 2017.

[152] Table of nuclides. http://www.kayelaby.npl.co.uk/atomic_and_nuclear_physics/4_6/4_6_1_part01_010_019.html#Cl, 2018. [Online Accessed 28/02/2018].

[153] Cl36 table de radionucléides. http://www.nucleide.org/DDEP_WG/Nuclides/Cl-36_tables.pdf, 2012. [Online Accessed 12/06/2018].

[154] Ni usb-6212. http://sine.ni.com/psp/app/doc/p/id/psp-94/lang/en, 2018. [Online Accessed 05/06/2018].

[155] Lm317t: 3-terminal 1.5 a positive adjustable voltage regulator. http://www.onsemi.com/PowerSolutions/product.do?id=LM317T, 2018. [Online Accessed 16/04/2018].

[156] Lm317 3-terminal adjustable regulator. http://www.ti.com/lit/ds/symlink/lm317.pdf, 2018. [Online Accessed 16/04/2018].

[157] Op27 datasheet. http://www.analog.com/media/en/technical-documentation/data-sheets/OP27.pdf, 2018. [Online Accessed 12/06/2018].

[158] Matlab. https://uk.mathworks.com/products/matlab.html, 2018. [Online Accessed 11/11/2018].

[159] what are three number in :pmanager->addprocess(new g4multiplescattering,-1, 1,1);. http://hypernews.slac.stanford.edu/HyperNews/geant4/get/phys-list/516/1.html, 2009. [Online Accessed 06/06/2018].

[160] Saint-Gobain. Caf2(eu) europium doped calcium fluoride. http://www.crystals.saint-gobain.com/products/caf2-calcium-fluoride, 2017. [Online Accessed 17/10/2017].

[161] F. Corsi, A. Dragone, C. Marzocca, A. Del Guerra, P. Delizia, N. Dinu, C. Piemonte, M. Boscardin, and G.F. Dalla Betta. Modelling a silicon photomultiplier (sipm) as a signal source for optimum front-end design. Nuclear Instruments and Methods in Physics Research Section A: Accelerators, Spectrometers, Detectors and Associated Equipment, 572(1):416 – 418, 2007. Frontier Detectors for Frontier PhysicsProceedings of the 10th Pisa Meeting on Advanced Detectors.

[162] Francesco Corsi, Maurizio Foresta, Cristoforo Marzocca, Gianvito Matarrese, and Alberto Del Guerra. Asic development for sipm readout. Journal of Instrumentation, 4(03):P03004, 2009.

[163] A. Bensalah, M. Mortier, G. Patriarche, P. Gredin, and D. Vivien. Synthesis and optical characterizations of undoped and rare-earth-doped caf2 nanoparticles. Journal of Solid State Chemistry, 179:2636–2644, 2006.

[164] H. Wang, R. Liu, K. Chen, X. Shi, and Z. Xu. Electrodeposition and characterization of caf2 and rare earth doped caf2 films. Thin Solid Films, 519:6438–6442, 2011.

[165] L.G. Jacobsohn, C.J. Kucera, T.L. James, K.B. Sprinkle, J.R. DiMaio, B. Kokuoz, B. Yazgan-Kokuoz, T.A. DeVol, and J. Ballato. Preparation and characterization of rare earth doped fluoride particles. Materials, 3, 2010.

[166] L.G. Jacobsohn, K.B. Sprinkle, S.A. Roberts, C.J. Kucera, T.L. James, E.G.

Yukihara, T.A. DeVol, and J. Ballato. Fluoride nanoscintillators. Journal of Nanomaterials, 2011:6, 2011. DOI:10.1155/2011/523638.

[167] Xiaoming Sun and Yadong Li. Size-controllable luminescent single crystal caf2 nanocubes. Chemical Communications, pages 1768–1769, 2003.

[168] C. Pandurangappa, B.N. Lakshminarasappab, and B.M. Nagabhushanac. Synthesis and characterization of caf2 nanocrystals. Journal of Alloys and Compounds, 489:592–595, 2010.

[169] F. Wang, X. Fan, D. Pi, and M. Wang. Synthesis and luminescence behaviour of eu3+- doped caf2 nanoparticles. Solid State Communications, 133:775–779, 2008.

[170] B.C. Hong and K. Kawano. Luminescence studies of the rare earth ions-doped caf2 and mgf2 films for wavelength conversion. Journal of Alloys and Compounds, 408:838–841, 2006.

[171] B. Ritter, T. Krahl, K. Rurack, and E. Kemnitz. Nanoscale caf2 doped with eu3+ and tb3+ through fluorolytic sol–gel synthesis. Journal Of Materials Chemistry C, 2:8607–8613, 2014.

[172] B.C. Hong and K. Kawano. Synthesis of eu-activated alkaline earth fluoride mf2 (m=ca, sr) nanoparticles). Japanese Journal of Applied Physics, 46:6319–6323, 2007.

[173] M Secu, C.E. Secu, and C. Ghica. Eu3+-doped caf2 nanocrystals in sol-gel derived glass ceramics. Optical Materials, 33:613–617, 2011.

[174] B.C. Hong and K. Kawano. Reduction of eu2+-activated nanoparticles by unique tcra treatment. Journal of Alloys and Compounds, 451:276–279, 2008.

[175] C. Pandey, S.M. Dhopte, P.L. Muthal, V.K. Kondawar, and S.V. Moharil. Eu3+ eu2+ redox reactions in bulk and nano caf2:eu. Radiation Effects & Defects in Solids, 162:651–658, 2007.

[176] Hiroyuki Ishibashi, Seikichi Akiyama, and Mitsuru Ishii. Effect of surface roughness and crystal shape on performance of bismuth germanate scintillators. Japanese Journal of Applied Physics, 25:1435–1438, 1986.

[177] Xingtao Chen, Tiecheng Lu, Nian Wei, Zhongwen Lu, Wei Zhang, Benyuan Ma, Yongbin Guan, Wei Liu, and Fenfen Jiang. Effect of ball-milling granulation with pvb adhesive on the sinterability of co-precipitated yb:yag nanopowders. Journal of Alloys and Compounds, 589:448 – 454, 2014.

[178] Young Kwan Kim, Ho Kyung Kim, Do Kyung Kim, and Gyuseong Cho. Synthesis of eu-doped (gd,y)2o3 transparent optical ceramic scintillator. Journal of Materials Research, 19(2):413–416, 2004.

[179] Y. Eagleman, E. Bourret-Courchesne, and S. E. Derenzo. Investigation of eu $^{2+}$ doped barium silicates as scintillators. IEEE Transactions on Nuclear Science, 59(2):479–486, April 2012.

[180] F. H. Ruddy, J. G. Seidel, Haoqian Chen, A. R. Dulloo, and Sei-Hyung Ryu. High-resolution alpha-particle spectrometry using 4h silicon carbide semicon-

ductor detectors. IEEE Transactions on Nuclear Science, 53(3):1713–1718, June 2006.

[181] G. Scholz, I. Dörfel, D. Heidemann, M. Feist, and R. Stösser. Nanocrystalline caf2 particles obtained by high-energy ball milling. Journal of Solid State Chemistry, 179(4):1119 – 1128, 2006.

[182] M. Broseghini, M. D'Incau, L. Gelisio, N.M. Pugno, and P. Scardi. Homogeneity of ball milled ceramic powders: Effect of jar shape and milling conditions. Data in Brief, 10:186 – 191, 2017.

[183] Calcium l-lactate pentahydrate. https://www.sigmaaldrich.com/catalog/product/sial/21175?lang=en&region=GB, 2018. [Online Accessed 13/05/2018].

[184] Ammonium fluoride. https://www.sigmaaldrich.com/catalog/product/aldrich/338869?lang=en&region=GB, 2018. [Online Accessed 13/05/2018].

[185] Europium(iii) acetate hydrate. https://www.sigmaaldrich.com/catalog/product/aldrich/325627?lang=en&region=GB, 2018. [Online Accessed 13/05/2018].

[186] Tri-sodium citrate. https://www.alfa.com/en/catalog/A12274/, 2018. [Online Accessed 11/02/2018].

[187] http://www.decon.co.uk/english/decon90.asp, 2018. [Online Accessed 06/02/2018].

[188] Sisini Sasidharan, Aswathy Jayasree, Sajid Fazal, Manzoor Koyakutty, Shantikumar V. Nair, and Deepthy Menon. Ambient temperature synthesis of citrate stabilized and biofunctionalized, fluorescent calcium fluoride nanocrystals for targeted labeling of cancer cells. Biomaterials Science, 1:294–305, 2013.

[189] What is raman spectroscopy? https://www.nanophoton.net/raman/raman-spectroscopy.html, 2018. [Online Accessed 09/05/2018].

[190] A basic overview of raman spectroscopy. http://www.renishaw.com/en/a-basic-overview-of-raman-spectroscopy--25805, 2018. [Online Accessed 09/05/2018].

[191] J P Russell. The raman spectrum of calcium fluoride. Proceedings of the Physical Society, 85(1):194, 1965.

[192] R.S. Krishnan and N. Krishnamurthy. The second order raman spectrum of calcium fluoride. Journal de Physique, 26:633–636, 1965.

[193] Fluroite sample data. http://rruff.info/Fluorite/, 2018. [Online Accessed 13/12/2018].

[194] Eric Faulques, Jany Wery, Bertrand Dulieu, Chris Seybert, and Dale L. Perry. Synthesis, fabrication, and photoluminescence of caf2 doped with rare earth ions. Journal of Fluorescence, 8(4):283–287, Dec 1998.

[195] Raman substrate materials. https://www.crystran.co.uk/raman-substrate-materials, 2012. [Online Accessed 06/05/2018].

[196] P. Samuel, H. Ishizawa, Y. Ezura, Ken Ichi Ueda, and S. Moorthy Babu. Spectroscopic analysis of eu doped transparent caf2 ceramics at different concentration. Optical Materials, 33(5):735 – 737, 2011. 5th Laser Ceramics Symposium: International Symposium on TRANSPARENT CERAMICS FOR PHOTONIC APPLICATIONS (LCS'09) Bilbao, Spain, December 9-11, 2009.

[197] P. Samuel. Investigation on rare earth ion doped solid state loser hosts Single crystals and transparent ceramics. PhD thesis, Anna University, Faculty of Science and Humanities, 9 2013. http://hdl.handle.net/10603/11301.

[198] Mastersizer 3000. https://www.malvernpanalytical.com/en/products/product-range/mastersizer-range/mastersizer-3000, 2018. [Online Accessed 11/11/2018].

[199] C14 table de radionucléides. http://www.nucleide.org/DDEP_WG/Nuclides/C-14_tables.pdf, 2012. [Online Accessed 26/04/2018].

[200] Pb210 table de radionucléides. http://www.nucleide.org/DDEP_WG/Nuclides/Pb-210_tables.pdf, 2012. [Online Accessed 26/04/2018].

[201] D. Eisma, G. W. Berger, Chen Wei-Yue, and Shen Jian. Pb-210 as a tracer for sediment transport and deposition in the Dutch-German Waddensea. Springer, Dordrecht, 1989.

[202] Handong Yang and Peter G. Appleby. Use of lead-210 as a novel tracer for lead (pb) sources in plants. Scientific Reports, 6:21707, 2016.

[203] Larry K. Benninger, Dale M. Lewis, and Karl K. Turekian. The Use of Natural Pb-210 as a Heavy Metal Tracer in the River—Estuarine System, chapter 12, pages 202–210. AMERICAN CHEMICAL SOCIETY, 1975.

[204] Nuclear and isotopic techniques for marine pollution monitoring. https://www.iaea.org/About/Policy/GC/GC54/GC54InfDocuments/English/gc54inf-3-att3_en.pdf, 2012. [Online Accessed 26/04/2018].

[205] Using isotopes to understand the oceans and climate change. https://www.iaea.org/About/Policy/GC/GC51/GC51InfDocuments/English/gc51inf-3-att3_en.pdf, 2012. [Online Accessed 26/04/2018].

[206] B. P. Welford. Note on a method for calculating corrected sums of squares and products. Technometrics, 4:419–420, 1962.

[207] Tony F. Chan, Gene H. Golub, and Randall J. LeVeque. Algorithms for computing the sample variance: Analysis and recommendations. The American Statistician, 37:242–247, 1983.

[208] Water density. https://water.usgs.gov/edu/density.html, 2018. [Online Accessed 11/06/2018].

[209] Material property database: Pdms. http://www.mit.edu/~6.777/matprops/pdms.htm, 2018. [Online Accessed 11/06/2018].

[210] Sylgard™ 184 silicone elastomer kit. https://consumer.dow.com/en-us/pdp.sylgard%E2%84%A2%20184%20silicone%20elastomer%20kit.01064291z.html?tab=overview&id=01064291z, 2018. [Online Accessed 11/06/2018].

[211] Tilly Alton, Stephen Monk, and David Cheneler. Heterogeneous scintillator geometries to maximise energy deposition for waterborne beta particle detection. Radiation Measurements, 111:6–12, 2018.

[212] Ltspice. http://www.analog.com/en/design-center/design-tools-and-calculators/ltspice-simulator.html, 2018. [Online Accessed 05/04/2018].

[213] Peak detection using labview and measurement studio. http://www.ni.com/white-paper/3770/en/, 2012. [Online Accessed 11/06/2018].

[214] Tle2426 datasheet. http://www.ti.com/lit/ds/symlink/tle2426.pdf, 2018. [Online Accessed 26/03/2018].

[215] Ha5002 datasheet. https://www.intersil.com/content/dam/Intersil/documents/ha-5/ha-5002.pdf, 2018. [Online Accessed 26/03/2018].

[216] Lt6200-10 datasheet. http://www.analog.com/media/en/technical-documentation/data-sheets/62001ff.pdf, 2018. [Online Accessed 26/03/2018].

[217] P. C. Carman. Fluid flow through granular beds*. Institute of Chemical Engineers, 75:S32–S48, 1937.

[218] Warren L. McCabe, Julian C. Smith, and Peter Harriot. Unit Operations of Chemical Engineering. McGraw-Hill, 7th edition, 2005.

[219] P. N. Dwivedi and S. N. Upadhyay. Particle-fluid mass transfer in fixed and fluidized beds. Ind. Eng. Chem. Process Des. Dev., 16(2):157–165, 1977.

[220] Benchtop pumps with 114dv flip top single channel pumphead. http://www.watson-marlow.com/gb-en/range/watson-marlow/100-laboratory-pumps/120dv/, 2018. [Online Accessed 18/06/2018].

[221] John R. Taylor. An Introduction to Error Analysis: The Study of Uncertainties in Physical Measurements. Oxford University Press: University Science Books, 1982.

[222] http://polymerdatabase.com/polymers/polymethylmethacrylate.html, 2018. [Online Accessed 12/02/2018].

[223] https://refractiveindex.info/?shelf=organic&book=poly(methyl_methacrylate)&page=Sultanova, 2018. [Online Accessed 12/02/2018].

[224] http://www.bpf.co.uk/plastipedia/polymers/polycarbonate.aspx, 2018. [Online Accessed 12/02/2018].

[225] https://pubchem.ncbi.nlm.nih.gov/compound/159987, 2018. [Online Accessed 12/02/2018].

[226] https://refractiveindex.info/?shelf=organic&book=polycarbonate&page=Sultanova, 2018. [Online Accessed 12/02/2018].

[227] C-series user manual. http://www.sensl.com/downloads/ds/UM-MicroC.pdf, 2016. [Online Accessed 12/07/2016].

[228] R. Burek and D. Chocyk. Basic aspects of the mass absorption coefficient of beta particles. Journal Of Radioanalytical And Nuclear Chemistry, 209:181–191, 1996.

[229] G. Peter Lepage. A new algorithm for adaptive multidimensional integration. Journal Of Computational Physics, 27:192–203, 1978.

[230] Python. Vegas 3.0 : Python package index. `https://pypi.python.org/pypi/vegas`, 2016. [Online Accessed 19/05/2016].

[231] Nico JD. Nagelkerke. A note on a general definition of the coefficient of determination. Biometrika, 78:691–692, 1991.